PEOPLE'S DEMOCRATIC REPUBLIC OF ALGERIA

MINISTRY OF HIGHER EDUCATION AND SCIENTIFIC RESEARCH

UNIVERSITY OF ECHAHID CHEIKH LARBI TEBESSI - TEBESSA

FACULTY OF SCIENCE AND TECHNOLOGY

LAboratory of Mathematics, Informatics and Systems (LAMIS)

THESIS

Submitted in partial fulfillment of the requirements for the degree of

3^{rd} **Cycle LMD Doctorate**

In : **TELECOMMUNICATIONS**

Speciality: **Telecommunications**

by : **Saoussen DJEDDI**

Title

Enhancing phase unwrapping for encoded InSAR interferograms

Defended publicly on: 09/07/2026, before jury composed of :

Abdallah Meraoumia	*Professor*	*Echahid Cheikh Larbi Tebessi University*	*Chairman*
Tarek Bentahar	*MCA*	*Higher National School RE2SD, Batna*	*Thesis Director*
Riad Saidi	*MCA*	*University Mustapha ben boulaid, Batna2*	*Thesis Co-director*
Hakim Bendjenna	*Professor*	*Echahid Cheikh Larbi Tebessi University*	*Examiner*
Noureddine Doghmane	*Professor*	*School of Technology and Engineering*	*Examiner*
Hassene Nezzari	*MCA*	*Echahid Cheikh Larbi Tebessi University*	*Examiner*

بسم الله الرحمن الرحيم

يرفع الله الذين آمنوا منكم والذين أوتوا العلم درجات

To My Beloved Father.

Boubakeur DJEDDI

– May Allah Grant Him Jannah –

whose dream became my journey, this dissertation is his, more than it is mine.

Saoussen DJEDDI

Acknowledgements

Al-Hamdoulillah ;

With Allah's mercy and guidance, I have reached the end of this journey.
I sincerely acknowledge my supervisor, Dr. Tarek Bentahar, and co-supervisor, Dr. Saidi Riad, for their official guidance and continuous support throughout this work.

I would like to express my sincere and profound appreciation, to Prof. Abdallah Meraoumia, Chairman of the Scientific Council, for his invaluable advice, guidance, and expertise. I am deeply grateful to Prof. Hakim Benjennah, Head of the Laboratory of Mathematics, Informatics and Systems -LAMIS- , for his constant encouragement and generous support throughout this work. I also wish to extend my sincere thanks to DR. Hassene Nezzari, and Prof. Noureddine Doghmane for their valuable contributions. I respectfully acknowledge all of them for accepting to serve as members of the jury, which constitutes a great honor for me.

I am grateful to Prof. Hanane Djellab, Head of the L3S Laboratory, for her constant support, invaluable advice, guidance, and expertise, at all costs.
I extend thanks as well to the Departments of Electronics and Telecommunications and Electrical Engineering, the Electronics Laboratory, and all faculty members, whose support created an environment conducive to learning and research.

To my fellow PhD students from Larbi Tebessi University and those I know from Abbas Laghrour University Khenchela, thank you for your friendship, shared discussions, and moments of laughter, and even trips – you made this journey lighter and far more memorable. To my close circle of friends, your support, encouragement, and celebration of every small achievement have meant more than words can express even from a far.

Above all, I owe my deepest gratitude to my family.
To my mother, whose prayers, patience, and sacrifices have been my constant support,
To my father -may Allah bless his soul- who never doubted me even when I doubted myself,

To all my family members, my two brothers and sister, who stood by side through every challenge. Special thanks to little -Enzo Ayan-, the youngest. And to my faithful cat -QQ-, whose quiet companionship kept me going through the years.

This work is a reflection of the love, faith, and support of everyone who has accompanied me on this journey. To all of you, I am endlessly grateful.

BLESSED.

Saoussen DJEDDI

Abstract

Interferometric Synthetic Aperture Radar (InSAR) is a remote sensing technique for measurement of surface topography and ground deformation under all-weather, day-and-night acquisition conditions. Despite its effectiveness, the interferometric phase is wrapped within the interval $(-\pi, \pi]$*, and recovering the absolute phase required for geophysical interpretation remains a challenging ill-posed inverse problem. Phase unwrapping is sensitive to noise, decorrelation, atmospheric disturbances, and geometric distortions, which can lead to error propagation in large-scale and high-resolution interferometric datasets. This thesis aims to enhance the robustness, accuracy, and scalability of InSAR phase unwrapping by developing two complementary approaches capable of improving performance in noisy, low-coherence, and complex deformation scenarios. The first proposed approach introduces an optimization-based phase unwrapping framework using the Multi-Verse Optimizer (MVO). In this method, phase unwrapping is formulated as a global optimization problem, and an optimization-guided quality map is developed to adaptively guide the unwrapping path and reduce error propagation in unreliable regions. The second proposed approach presents VOH-Net, a Vision-Optimized Hybrid Network designed for InSAR phase unwrapping. The architecture combines convolutional neural networks for local spatial feature extraction with enhanced multi-directional Long Short-Term Memory (LSTM) modules to capture long-range spatial dependencies and preserve global phase consistency across large interferograms. Experimental evaluations conducted on both synthetic and real InSAR datasets demonstrate that the proposed methods outperform classical, optimization-based, and learning-based phase unwrapping techniques. In particular, the enhanced VOH-Net achieved 78.4%, 94.7%, and 79.0% reductions in the Mean Absolute Error (MAE), Mean Squared Error (MSE), and Root Mean Squared Error (RMSE), respectively, while improving the Structural Similarity Index Measure (SSIM) by 3.8% compared with the original loss formulation. In addition, the proposed approaches exhibit robustness to noise and decorrelation, and improved reconstruction accuracy over large and highly deformed interferograms. The findings of this thesis demonstrate that integrating global optimization with deep learning provides an effective and reliable strategy for InSAR phase unwrapping. The MVO-based framework enhances robustness through adaptive optimization-guided path selection, whereas VOH-Net improves scalability and global phase consistency through hybrid spatial learning. Together, these complementary contributions advance the state of the art in InSAR phase unwrapping and provide a robust foundation for generating more accurate InSAR-derived geophysical products.*

Keywords: *InSAR, Phase Unwrapping, Multi-Verse Optimizer, Deep Learning, CNN, LSTM, Hybrid Networks.*

Contents

List of Figures

List of Tables

Abbreviations

A Anti-diagonal

BiLSTM Bidirectional Long Short-Term Memory

CNN Convolutional Neural Network

D Diagonal

DEM Digital Elevation Model

E-LSTM Enhanced Long Short-Term Memory

FLOPs Floating-Point Operations

GFF Guided Flood Fill

GFLOPs Giga Floating-Point Operations

H Horizontal

InSAR Interferometric Synthetic Aperture Radar

LD Length of Discontinuities

LSTM Long Short-Term Memory

MAE Mean Absolute Error

MAP Maximum A Posteriori

MCF Minimum-Cost Flow

MSE Mean Squared Error

MVO Multi-Verse Optimizer

ND Number of Discontinuities

PDV Phase Derivative Variance

PSI Persistent Scatterer Interferometry

PSNR Peak Signal-to-Noise Ratio

PU Phase Unwrapping

QG Quality-Guided

RMSE Root Mean Square Error

SAR Synthetic Aperture Radar

SLC Single-Look Complex

SNR Signal-to-Noise Ratio

SSIM Structural Similarity Index Measure

TV Total Variation

V Vertical

VOH-Net Vision-Optimized Hybrid Network

Chapter 1

General Introduction

1.1 Introduction

In recent decades, Interferometric Synthetic Aperture Radar (InSAR) has emerged as one of the most transformative and versatile technologies in Earth observation, reshaping the way scientists, engineers, and policymakers monitor and analyze the planet. Unlike optical sensors, which rely on sunlight and are easily obstructed by cloud cover, Synthetic Aperture Radar (SAR) systems operate in the microwave domain, allowing consistent imaging of the Earth's surface regardless of illumination conditions or atmospheric interference [1] [2]. This capability has proven particularly valuable in polar regions, tropical zones with persistent cloud cover, and disaster-affected areas where rapid and reliable monitoring is essential [3].

InSAR extends the capabilities of SAR by exploiting the phase difference between two or more radar acquisitions obtained over the same scene [1] [2]. Through this principle, it enables high-precision mapping of surface displacement and topography, often achieving centimeter- to millimeter-level accuracy [4]. Such precision has transformed geoscience research, enabling detailed studies of tectonic deformation, volcanic activity, glacial dynamics, and anthropogenic impacts such as land subsidence and infrastructure stability. For example, InSAR-derived displacement maps have been used to evaluate post-earthquake fault motion [5] [6], monitor volcano inflation [7], and track glacier flow in response to climate change [8].

The versatility of InSAR extends beyond natural processes. Urban infrastructure monitoring increasingly relies on SAR interferometry to detect subtle structural deformations caused by groundwater extraction, construction activities, or traffic-induced vibrations [3] [9]. Bridges and dams are now routinely assessed using InSAR-derived data [10], while high-rise buildings and transportation networks are also monitored using interferometric measurements in engineering practice [11] [12].

Despite these advances, the full potential of InSAR remains constrained by a fundamental challenge: phase unwrapping (PU). Interferometric measurements provide only wrapped phase values in the interval $(-\pi, \pi]$. Converting these wrapped phases into physically meaningful, continuous values requires reconstructing the underlying true phase field, a process that is mathematically ill-posed [4] [13] and prone to error in operational settings [9]. Unwrapping errors propagate across the interferogram, producing artifacts and potentially misleading displacement signals, which can compromise scientific interpretations and decision-making in hazard assessment and infrastructure monitoring.

In this context, reliable phase unwrapping is essential because any error introduced at this stage propagates to the final geophysical product. Inaccurate phase reconstruction may lead to false deformation patterns, incorrect topographic estimation, and misleading scientific interpretation. For this reason, improving the robustness and accuracy of phase unwrapping remains an active and important research direction in modern InSAR processing.

1.2 Problem Statement

In InSAR processing, the observed interferometric phase is not directly available as a continuous quantity, but rather as a wrapped phase restricted to the principal interval $(-\pi, \pi]$. Consequently, several possible continuous phase values may correspond to the same wrapped measurement, making the recovery of the true phase inherently ambiguous. The phase unwrapping problem can therefore be viewed as the task of determining the correct integer multiples of 2π that must be added to the wrapped phase in order to reconstruct a physically meaningful continuous phase field [9] [13]. From a mathematical point of view, this is an ill-posed inverse problem [14] [15] [16] [17].

In ideal situations, where the phase varies smoothly and noise levels are low, local phase continuity assumptions are often sufficient to recover the unwrapped phase correctly. However, real interferometric data rarely satisfy these ideal conditions. In practice, the wrapped phase is strongly affected by noise, temporal and spatial decorrelation, atmospheric disturbances, orbital inaccuracies, and geometric distortions. In addition, abrupt geophysical events such as fault ruptures, landslides, or sharp topographic transitions may produce genuine phase discontinuities that further complicate the reconstruction process.

The difficulty of phase unwrapping does not stem only from ambiguity, but also from error propagation. A local mistake in one part of the interferogram can affect neighboring regions and spread across the image, resulting in large-scale distortions in the reconstructed phase surface. Such errors are particularly problematic in low-coherence areas, where the reliability of the measured phase is already reduced.

This challenge becomes even more significant with the continuous growth in the spatial resolution and size of modern SAR datasets. High-resolution interferograms often contain millions of pixels and exhibit complex spatial patterns that demand both strong robustness and computational scalability. Therefore, there is a clear need for advanced phase unwrapping approaches capable of handling noisy, discontinuous, and large-scale interferometric data more effectively than traditional methods [18] [19].

1.3 Limits of Existing Approaches

Over the past decades, numerous phase unwrapping methods have been developed for InSAR applications. Early classical approaches, such as branch-cut algorithms introduced by Goldstein et al. [14], addressed phase discontinuities by identifying and connecting residues to prevent incorrect phase integration. Least-squares methods formulated phase unwrapping as an optimization problem that minimizes the difference between the wrapped and reconstructed phase gradients [4]. Minimum-cost flow and network-based approaches further improved robustness by modeling the unwrapping problem as a global optimization over a graph structure [41, 52]. Quality-guided methods, such as the reliability sorting algorithm proposed by Herraez et al. [13] and region-growing approaches [78], introduced adaptive traversal strategies by prioritizing reliable pixels during reconstruction.

These classical approaches remain important due to their mathematical foundation, interpretability, and effectiveness under moderate noise conditions. However, their performance can degrade in the presence of severe noise, decorrelation, dense residue distributions, and abrupt phase variations [19, 43]. To address these limitations, optimization-based and metaheuristic approaches have been investigated by formulating phase unwrapping as a global optimization problem, aiming to improve robustness against local errors. Nevertheless, many of these approaches still depend on handcrafted reliability criteria, require parameter tuning, and may introduce significant computational costs, particularly for large-scale interferograms [20, 43].

1.4 Original Contributions

The thesis makes two principal methodological contributions and one comparative scientific contribution to the field of InSAR phase unwrapping.

The first contribution is the development of an optimization-guided phase unwrapping framework based on the Multi-Verse Optimizer. In this framework, the reliability map guiding the phase integration process is formulated as an adaptive and tunable component rather than a fixed handcrafted descriptor. By optimizing the parameters of this guidance mechanism, the proposed method improves the stability of quality-guided unwrapping, especially in noisy and low-coherence regions. The main contributions related to this approach are summarized as follows:

1. Global Optimization Formulation of InSAR Phase Unwrapping Phase unwrapping is reformulated as a constrained optimization problem, where phase consistency, reliability measures, and noise robustness are jointly considered within a global search framework.

2. Optimization-Guided Quality Map Construction A novel quality mapping strategy is introduced, in which the MVO adaptively optimizes pixel reliability to guide unwrapping paths, particularly in low-coherence and highly noisy regions.

3. Improved Robustness to Noise and Discontinuities By exploiting the exploration–exploitation balance inherent to MVO, the proposed approach reduces error prop-

agation and phase jumps near residues and discontinuities compared to classical quality-guided methods.

4. Scalability for Large-Scale Interferograms The MVO-based framework is designed to operate on large interferograms, demonstrating improved stability and convergence behavior in high-resolution InSAR datasets.

5. Quantitative Validation Against Classical and Metaheuristic Methods Extensive experiments on synthetic and real interferograms demonstrate that the MVO-based approach achieves superior accuracy and consistency compared to conventional optimization and path-integration techniques.

The second contribution is the development of VOH-Net, a hybrid deep neural architecture specifically designed for phase unwrapping. The proposed model combines a convolutional encoder-decoder structure with an enhanced multidirectional LSTM module to model both short-range phase features and long-range spatial continuity. This design enables more robust reconstruction in interferograms exhibiting complex phase patterns and degradation. The principal contributions of this approach are as follows:

1. Design of a Dedicated Deep Neural Architecture for Phase Unwrapping VOH-Net is specifically tailored to the phase unwrapping problem, combining convolutional layers for local feature extraction with recurrent mechanisms to model long-range spatial dependencies.

2. Multidirectional Context Modeling for Phase Continuity Preservation The architecture incorporates multidirectional sequence modeling to capture global phase trends and ensure spatial consistency across complex interferometric patterns.

3. Learning-Based Handling of Noise and Low-Coherence Regions VOH-Net learns robust representations of wrapped phase data, enabling effective unwrapping in challenging regions where classical methods typically fail.

4. Generalization Across Diverse Terrains and Deformation Scenarios The network is trained and evaluated on both synthetic and real-world interferograms, demon-

strating strong generalization performance across varying noise levels, terrain types, and deformation patterns.

5. Comparative Performance Gains Over Existing Deep Learning Models Experimental results show that VOH-Net outperforms existing CNN- and U-Net–based architectures in terms of unwrapping accuracy, structural consistency, and error suppression.

1.5 Structure Overview

To systematically address the research objectives and present a coherent scientific narrative, this thesis is organized into seven chapters, each building upon the previous to guide the reader from foundational concepts to advanced contributions and conclusions.

The first part, comprising Chapters 1, 2, and 3, establishes the conceptual and scientific background of the study. It begins by introducing the motivation, research problem, objectives, and contributions, then develops the theoretical foundations of SAR and InSAR interferometry, including radar imaging principles, phase ambiguity, noise sources, and atmospheric or orbital effects. This foundation is complemented by a comprehensive review of existing phase unwrapping techniques, covering classical, optimization-based, metaheuristic, and deep learning approaches. Together, these chapters define the research gaps that motivate the work presented in the thesis.

The second part of the thesis, represented by Chapters 4 and 5, presents the main methodological contributions. It first introduces an optimization-guided quality mapping strategy based on the Multi-Verse Optimizer, detailing its formulation, algorithmic framework, and implementation for improving phase unwrapping reliability. The thesis then extends this contribution through the development of VOH-Net, a deep learning architecture designed for InSAR phase unwrapping. This part describes the network design, training pipeline, and data preparation strategy, showing how optimization-based and learning-based perspectives are combined to address the limitations identified in the literature.

The third part, covering Chapters 6 and 7, focuses on validation, analysis, and future perspectives. The proposed methods are evaluated through extensive experiments using defined datasets, evaluation metrics, comparative studies, cross-validation procedures, and performance assessments. These analyses demonstrate the effectiveness, robustness, and scalability of the developed approaches. Finally, the thesis concludes by summarizing the main findings and contributions, discussing existing limitations, and outlining future research directions, including transformer-based models, multi-temporal InSAR processing, and deeper integration of optimization and learning frameworks for operational deployment.

Chapter 2

Theoretical foundations of synthetic aperture radar and interferometric synthetic aperture radar, and phase unwrapping

2.1 Introduction

Synthetic Aperture Radar (SAR) and Interferometric Synthetic Aperture Radar (InSAR) provide the physical and methodological basis of phase-based Earth observation. SAR is an active microwave imaging system that records complex backscatter from the Earth surface [17] [18], whereas InSAR uses phase differences between two coherent SAR acquisitions to infer terrain elevation and surface displacement [1] [2]. In this thesis, these concepts are not treated as generic background only; they define the observation model from which the phase-unwrapping problem emerges.

The interferometric phase delivered by the sensor is wrapped modulo 2π and therefore does not directly reveal the continuous phase required for geophysical interpretation. Recovering that continuous phase is difficult because the signal is affected by noise, decorrelation, atmospheric delay, orbital residuals, and geometric distortions. As a result, phase unwrapping is not a secondary numerical detail but a structural bottleneck in the InSAR processing chain.

Chapter 2 is organized as a problem-oriented theoretical framework. It first introduces the principles of SAR imaging, including acquisition geometry, complex signal formation, spatial resolution, and the main geometric distortions affecting radar observations. It then presents the fundamentals of InSAR, including acquisition configurations, interferogram formation, the physical components of interferometric phase, baseline geometry, and the role of coherence, noise, and decorrelation in phase quality. On that basis, the chapter defines wrapped and absolute phase, explains integer ambiguity, the Itoh condition, and phase residues, and situates these concepts within the interferometric SAR processing chain before clarifying why phase unwrapping becomes difficult under realistic operational conditions. The purpose is to prepare the analytical ground for the algorithmic review developed in the next chapter.

2.2 Synthetic Aperture Radar Imaging Principles

This section presents the theoretical basis of Synthetic Aperture Radar imaging, with particular emphasis on the geometric configuration and observation mechanism that govern SAR data acquisition.

2.2.1 Imaging geometry and observation concept

SAR is a side-looking radar system carried by a moving platform such as a satellite or aircraft. Rather than pointing vertically toward nadir, the antenna illuminates a lateral strip of the Earth surface. As the platform advances along its flight path, successive echoes are coherently combined to synthesize a long antenna aperture and produce high-resolution images.

The principal geometric elements of SAR imaging are the flight path, antenna look direction, nadir, slant range, range direction, azimuth direction, and swath. Slant range represents the direct line-of-sight distance between antenna and ground target, while azimuth refers to the along-track direction parallel to platform motion. This side-looking geometry is central to both SAR image formation and later interferometric sensitivity because it controls path length, incidence angle, and terrain distortion. Figure 2.1 illustrates the fundamental side-looking geometry of a Synthetic Aperture

Radar (SAR) system, which governs how the radar illuminates the Earth's surface and how the returned signal is interpreted. Unlike optical sensors that observe the ground nearly vertically, SAR acquires data obliquely along the flight track. This acquisition geometry is central to SAR image formation because it defines the slant-range measurement, the azimuth direction, the illuminated swath, and the geometric distortions that later affect interferometric analysis.

This geometry establishes the reference frame used throughout the chapter. In particular, the slant-range and azimuth directions determine how SAR samples the scene and explain why radar measurements are inherently sensitive to topography and viewing angle. The radar platform moves along the flight path, while the antenna points sideways toward the observed terrain. The direction parallel to platform motion is called the azimuth direction, whereas the direction perpendicular to the flight path, toward the observed ground targets, is the range direction. The slant range is the direct line-of-sight distance between the radar antenna and a target on the ground, and it is one of the principal quantities measured by the SAR system. The nadir corresponds to the point directly beneath the sensor, while the look angle defines the orientation of the radar beam relative to the vertical direction. The portion of the ground illuminated by the radar beam is referred to as the swath.

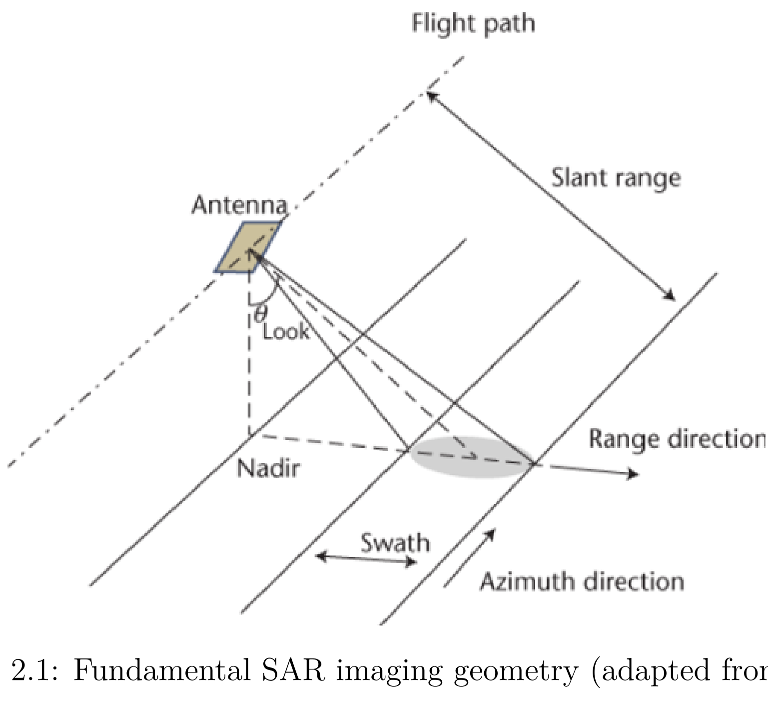

Figure 2.1: Fundamental SAR imaging geometry (adapted from NASA).

This geometry is of primary importance because it controls both SAR image formation and the interpretation of interferometric phase. In particular, the side-looking configuration enables high-resolution imaging through synthetic aperture processing, but it also introduces characteristic distortions such as foreshortening, layover, and shadow in areas of steep topography. Therefore, understanding the geometric relationships illustrated in Figure 2.1 is essential before discussing interferogram formation, baseline effects, and phase unwrapping in the following sections.

2.2.2 Complex SAR signal formation

SAR systems illuminate the Earth with coherent microwave pulses and record the backscattered echoes returned by distributed and point-like scatterers. Unlike passive optical sensors, SAR does not depend on solar illumination and is far less affected by cloud cover, smoke, or moderate precipitation [26] [27]. These properties explain its importance for all-weather observation of seismic zones, ice sheets, coastal environments, and urban infrastructure [23].

Each SAR pixel is complex-valued and contains both amplitude and phase. Amplitude is mainly related to the radar cross-section of the illuminated target ensemble, whereas phase is proportional to the two-way electromagnetic path length between the sensor and the target. The complex SAR signal may be expressed as:

$$s(x, y) = A(x, y)e^{j\phi(x,y)} \tag{2.1}$$

Here, $A(x, y)$ denotes the backscattered amplitude and $\phi(x, y)$ the measured phase. The fundamental geometric observable is the slant range R, which is derived from the pulse round-trip time τ according to:

$$R = \frac{c\tau}{2} \tag{2.2}$$

where R is the slant range (m), $c \approx 3 \times 10^8$ m/s is the speed of light, and τ is the measured pulse round-trip time (s). The factor of 2 accounts for the two-way propagation of the radar signal, from the sensor to the target and back.

The phase term is extremely sensitive to small path-length changes: variations much smaller than the radar wavelength can produce measurable phase shifts [1] [2]. This sensitivity is the reason interferometry can resolve millimetric deformation when coherence is maintained and nuisance terms are sufficiently controlled [23].

2.2.3 Resolution, frequency bands, and geometric distortions

SAR spatial resolution is governed by different mechanisms in range and azimuth. Range resolution depends mainly on transmitted bandwidth B. After pulse compression, the theoretical slant-range resolution is given by [26] [27]:

$$\delta_r = \frac{c}{2B} \tag{2.3}$$

Azimuth resolution is achieved synthetically by coherently combining echoes acquired along the platform trajectory. For stripmap SAR, the nominal azimuth resolution may be approximated by [27] [29]:

$$\delta_{az} \approx \frac{L}{2} \tag{2.4}$$

where L is the physical antenna length in the azimuth direction. This synthetic-aperture principle makes azimuth resolution largely independent of platform altitude, which constitutes one of the main advantages of SAR over real-aperture radar [23].

At the same time, side-looking geometry introduces characteristic distortions such as foreshortening, layover, and radar shadow. These effects influence image interpretation and phase reliability because steep slopes, shadowed areas, and layover zones frequently violate continuity assumptions or reduce interferometric coherence [27] [29]. Frequency band selection also matters because wavelength affects penetration, scattering regime, and coherence behaviour. The operating wavelength of a SAR system is a fundamental parameter because it controls how the radar signal interacts with the Earth's surface and near-surface features. Different wavelength bands exhibit different penetration capabilities, sensitivities to vegetation and surface roughness, and levels of suitability for specific remote-sensing applications. For this reason, the selection of the radar band directly influences the quality of SAR and InSAR observations, particularly in studies related to topography, deformation monitoring, biomass estimation, and urban mapping. Table 2.1 summarizes the principal SAR frequency bands commonly used in remote sensing and highlights their approximate wavelengths, interaction characteristics, and typical application strengths.

Table 2.1: Main SAR frequency bands and their typical characteristics.

Band	Approximate wavelength	Penetration / interaction	Typical strengths
X	3.1 cm	Low penetration; strong interaction with small-scale roughness and built structures	Fine urban detail and infrastructure mapping
C	5.6 cm	Moderate vegetation penetration and strong surface sensitivity	Operational Earth observation and deformation monitoring
L	23.5 cm	Greater penetration through vegetation and dry soil	Forests, biomass, and longer-term coherence in some terrains
P	68–70 cm	Very strong penetration but reduced spatial resolution and stricter regulation	Sub-canopy structure, tomography, and experimental campaigns

As shown, shorter wavelengths such as X-band and C-band are generally more sensitive to surface features and man-made structures, making them suitable for urban mapping and operational deformation studies. By contrast, longer wavelengths such as L-band and P-band penetrate vegetation and dry soil more effectively, which makes them advantageous for forest observation, biomass estimation, and sub-canopy investigations. This wavelength-dependent behaviour is especially important in InSAR applications because it affects coherence preservation, scattering mechanisms, and the reliability of phase measurements over different land-cover types.

2.3 SAR Limitations

Because SAR is a side-looking imaging system, terrain relief is projected onto the slant-range geometry rather than onto a true horizontal ground plane. This creates three canonical distortions foreshortening, layover, and shadow which affect both image interpretation and the spatial continuity assumptions used later in phase unwrapping. As shown in the figure 2.2 below

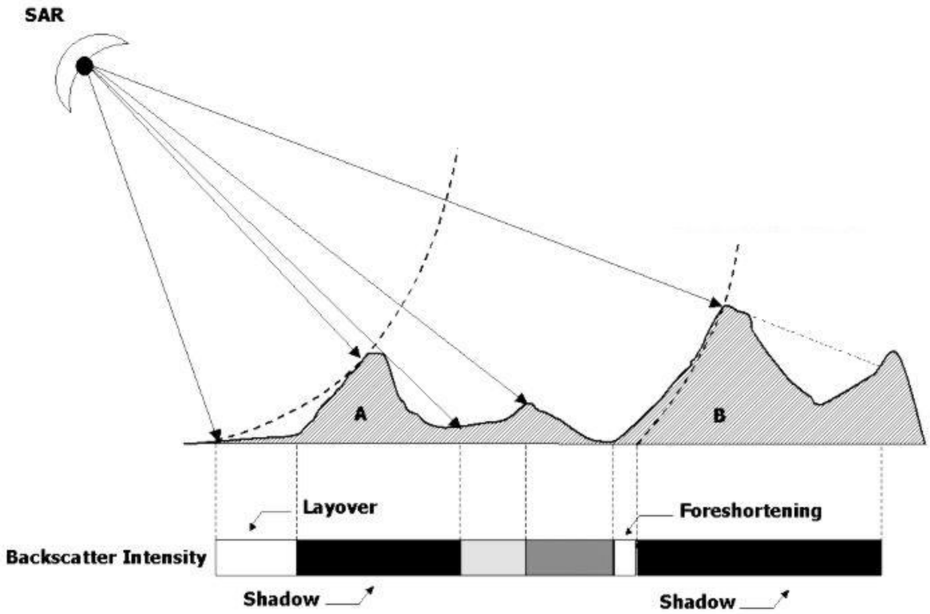

Figure 2.2: Principal geometric distortions in side-looking SAR imagery: layover, foreshortening, and radar shadow.

These distortions arise directly from the side-looking imaging geometry of SAR. They are not merely interpretive artefacts; in interferometric applications they also reduce phase reliability and can create gaps or inconsistencies that complicate phase unwrapping.

2.3.1 Foreshortening

Foreshortening geometry in radar-facing terrain slopes. Foreshortening occurs when a terrain slope faces the radar and its local slope angle is smaller than the radar incidence angle. In this configuration, the distance between scatterers along the slope is compressed in slant range, causing the slope to appear shortened in the SAR image and modifying the observed phase distribution.

These sketches in Figure 2.3 show that the ground-projected resolution cell changes with terrain orientation. Even when phase remains coherent, such geometric compression alters spatial sampling and can make steep terrain more difficult to interpret reliably.

2.3.2 Layover

Layover occurs when the local terrain slope exceeds the incidence angle, that is, $\alpha \geq \theta$.

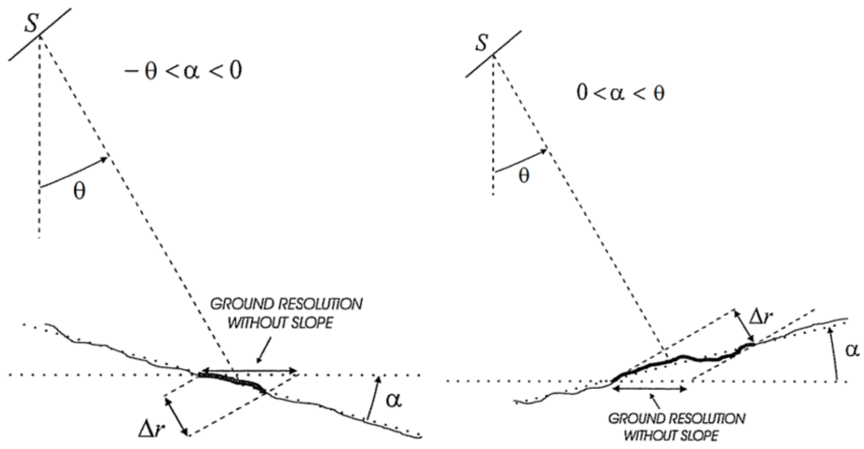

Figure 2.3: Foreshortening under negative and positive terrain slopes relative to the radar line of sight.

Causes an inversion of the image geometry. Peaks of hills or mountains with a steep slope commute with their bases in the slant range resulting in severe image distortion.figure 2.4 presents a layover geometry when the local terrain slope exceeds the radar incidence angle.

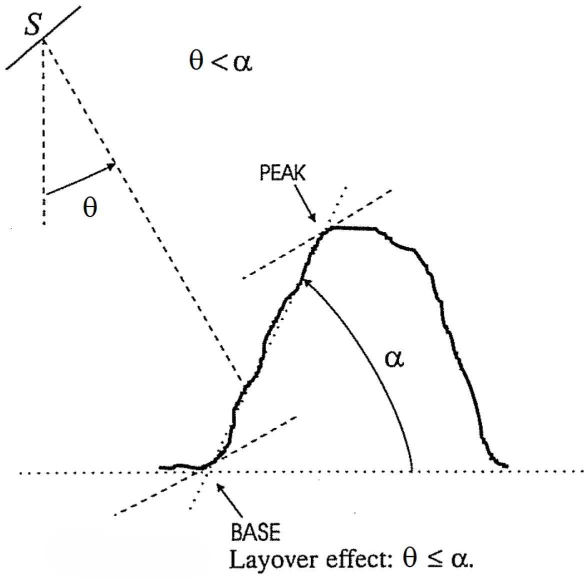

Figure 2.4: Layover geometry in sloped terrain.

Layover occurs when the local terrain slope is greater than the radar incidence angle, causing returns from higher elevations to arrive earlier than returns from lower slope positions. This produces geometric reversal in the SAR image, distorts the interferometric phase field, and can undermine local continuity-based phase unwrapping

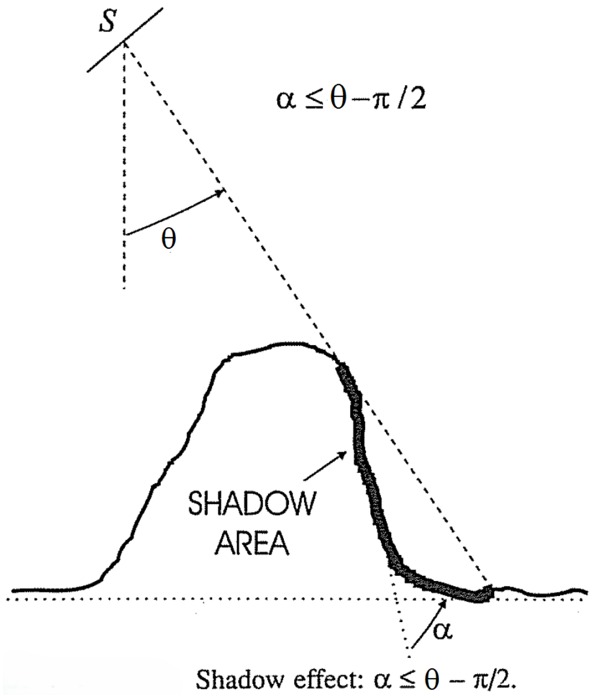

Figure 2.5: Radar shadow geometry in side-looking SAR imaging.

assumptions.

2.3.3 Shadow

Radar shadow occurs when the terrain slopes away from the sensor so strongly that the radar beam cannot illuminate the surface, approximately $\alpha \leq \theta - \frac{\pi}{2}$.

Radar shadow produces a region without any backscattered signal. This effect can extend over other areas regardless of the slope of those areas. As shown below (Figure 2.5)

Figure 2.5 shows how The radar sensor illuminates the terrain obliquely from the side rather than from directly overhead. When the terrain slope facing away from the radar is sufficiently steep, the microwave beam cannot reach the ground surface behind the obstacle. This non-illuminated region becomes a shadow area, where little or no backscattered energy returns to the sensor. In the image domain, such regions typically appear as dark zones because no meaningful echo is received from them.

2.4 Interferometric Synthetic Aperture Radar (InSAR) Fundamentals

The fundamental principle of Interferometric Synthetic Aperture Radar (InSAR) is based on observing the same ground target from two slightly different sensor positions. By introducing a small geometric separation between the two radar acquisitions, known as the baseline B, the system produces a slight difference in the travel path from the sensor to the target. This path difference generates a measurable phase difference between the two received radar signals. As a result, InSAR transforms phase information into a geometric observable that can be exploited to estimate terrain elevation and, in differential applications, surface deformation. InSAR observations can be acquired using two main geometric configurations, depending on whether the radar images are collected simultaneously or at different times. These acquisition modes determine how the interferometric baseline is formed and strongly influence the sensitivity of the interferometric phase to topography, deformation, and temporal decorrelation. Figure 2.6 illustrates the two principal InSAR acquisition strategies: single-pass (simultaneous baseline) and repeat-pass (repeat-track) interferometry.

single-pass interferometry uses two antennas or two receiving channels to observe

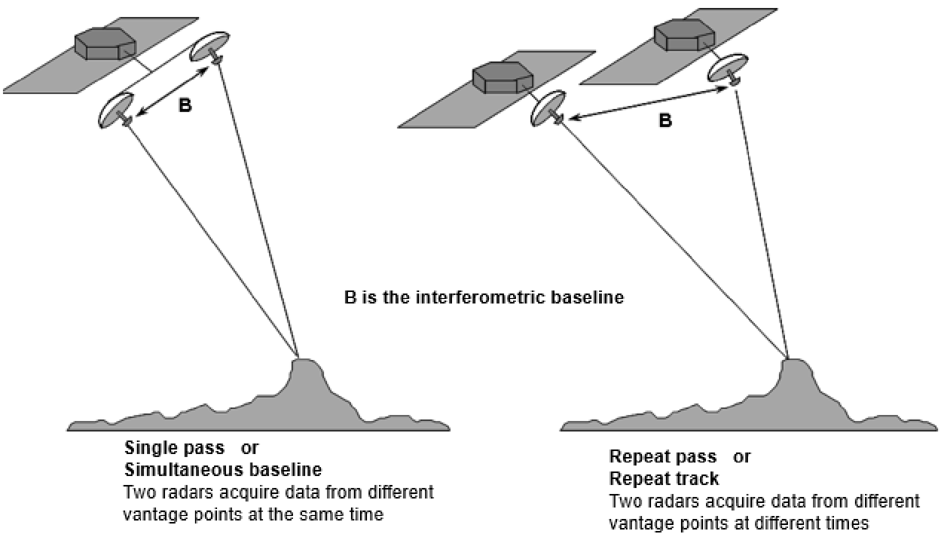

Figure 2.6: Comparison of the two main InSAR acquisition modes: single-pass (simultaneous baseline), and repeat-pass (repeat-track).

the same ground target simultaneously from slightly different positions. Because both measurements are acquired at the same time, this configuration largely avoids temporal decorrelation and is therefore well suited for accurate topographic mapping. The geometric separation between the two observation points defines the interferometric baseline B, which creates a path-length difference and, consequently, an interferometric phase difference related to terrain elevation.

By contrast, repeat-pass interferometry acquires the two SAR images at different times, usually from nearly identical orbital tracks. In this case, the baseline is formed by the small positional difference between the two sensor locations during successive passes. While this configuration is operationally more common in satellite radar missions, it is more sensitive to temporal changes in the scene, atmospheric disturbances, and surface motion between acquisitions. As a result, the measured phase contains not only topographic information but may also include deformation and decorrelation effects.

This distinction is important in InSAR analysis because the acquisition mode determines both the quality of coherence and the physical interpretation of the interferometric phase. In general, single-pass systems are preferred for pure topographic retrieval, whereas repeat-pass systems provide the basis for deformation monitoring and differential InSAR applications when temporal phase contributions are properly modeled or removed.

2.4.1 Interferogram formation

InSAR combines two co-registered complex SAR images acquired from slightly different viewing geometries or at different times. If $S_1(x, y)$ and $S_2(x, y)$ denote the registered complex images, the interferogram is formed by multiplying one image by the complex conjugate of the other [1, 25]:

$$I(x, y) = S_1(x, y)S_2^*(x, y) = A_1A_2e^{j(\phi_1-\phi_2)} \tag{2.5}$$

The interferometric phase is therefore the argument of the complex interferogram:

$$\phi_{int}(x, y) = \arg\{I(x, y)\} = \phi_1(x, y) - \phi_2(x, y) \tag{2.6}$$

This phase difference contains a superposition of topography, deformation, atmospheric propagation, orbital uncertainty, and random noise [1, 2]. Interferogram formation therefore condenses multiple physical effects into a single observable, which is precisely why accurate modelling and phase unwrapping are essential steps in the processing chain [25].

Operationally, interferogram generation begins with two single-look complex (SLC) images, often referred to as the reference and secondary acquisitions. These images must be co-registered so that corresponding pixels represent the same ground targets. Orbit refinement, cross-correlation, and geometric warping are used to ensure sub-pixel alignment before phase differencing is performed.

2.4.2 Components of the interferometric phase

Under a standard additive model, the absolute interferometric phase may be decomposed as [25, 31]:

$$\phi_{int} = \phi_{topo} + \phi_{def} + \phi_{atm} + \phi_{orb} + \phi_{noise} \tag{2.7}$$

Here, ϕ_{topo} is the topographic component controlled mainly by baseline geometry; ϕ_{def} represents line-of-sight surface displacement; ϕ_{atm} aggregates tropospheric and ionospheric delays; ϕ_{orb} corresponds to residual orbital inaccuracies; and ϕ_{noise} captures decorrelation, thermal noise, and residual modelling errors [32]. In practice, the scientific objective is rarely to estimate all components independently from first principles. Rather, one seeks to suppress or separate nuisance terms sufficiently so that the remaining phase can be interpreted as elevation or deformation [18, 25, 31, 33].

The topographic phase arises from the sensor-target geometry and the interferometric baseline, and it is the component primarily exploited for digital elevation model generation. The deformation phase is associated with ground displacement along the radar line of sight and constitutes the main observable in surface-motion studies such as subsidence, seismic deformation, and volcanic monitoring. By contrast, the atmospheric phase and orbital phase are generally unwanted contributions, since they introduce spatially correlated artefacts and large-scale ramps that may be misinterpreted as geophysical signals if not properly corrected.

Table 2.2: Main components of the interferometric phase and their physical interpretation.

Component	Origin	Effect on interferogram	Operational consequence
Topographic phase	Sensor–target geometry and baseline	Fringe pattern linked to elevation	Enables DEM generation but must be removed in D-InSAR
Deformation phase	Surface displacement along radar line of sight	Temporal phase change between acquisitions	Core observable for geodesy and hazard monitoring
Atmospheric phase	Tropospheric water vapour and ionospheric variability	Spatially correlated artefacts and long-wavelength ramps	Can mimic deformation or bias time-series analysis
Orbital phase	Residual ephemeris and baseline errors	Large-scale phase ramps	Requires orbit refinement or ramp estimation
Noise / decorrelation	Thermal noise, temporal change, geometric mismatch	Randomized phase and residue concentration	Reduces unwrap reliability and increases bias

Table 2.2 also highlights the importance of noise and decorrelation, which do not simply add a smooth phase term but instead degrade phase reliability by introducing randomness, residue concentration, and local ambiguity. This is particularly critical for phase unwrapping, because low-quality phase observations increase the probability of unwrapping errors and reduce the accuracy of the final elevation or deformation product. Accordingly, InSAR processing is fundamentally concerned with isolating the desired phase contribution while minimizing or compensating for the remaining error sources.

2.5 Coherence, Noise, and Decorrelation

Interferometric coherence γ is the canonical indicator of phase reliability. It measures the normalized similarity between two complex SAR observations and, in expectation form, is written as [25, 34]:

$$\gamma = \frac{|E\{S_1 S_2^*\}|}{\sqrt{E\{|S_1|^2\}E\{|S_2|^2\}}} \tag{2.8}$$

High coherence indicates that the scattering process remains stable between acquisitions, whereas low-coherence suggests that the measured phase is strongly contaminated by decorrelation and noise [35]. In practice, coherence is degraded by temporal change, spatial baseline mismatch, vegetation volume scattering, geometric distortions, and thermal noise. Because most phase-unwrapping methods rely explicitly or implicitly on local continuity, coherence maps are not merely descriptive products; they are diagnostic maps of algorithmic difficulty [36].

Table 2.3: Main decorrelation and noise sources affecting interferometric phase quality.

Source	Physical cause	Signature in phase/coherence	Implication for unwrapping
Temporal decorrelation	Vegetation growth, moisture change, surface disturbance	Reduced coherence between acquisitions	Higher residue density and local ambiguity
Spatial decorrelation	Large perpendicular baseline and differing viewing geometry	Phase mismatch despite static terrain	Loss of reliable gradients in rugged areas
Volume scattering	Multiple scatterers within the resolution cell, especially vegetation	Randomized phase contribution	Poor continuity and unstable unwrap paths
Thermal noise	Sensor noise and weak backscatter	Speckled phase with low SNR	Noisy gradients and false discontinuities
Atmospheric heterogeneity	Water vapour and ionospheric fluctuation	Correlated artefacts and ramps	Bias in deformation estimates after unwrapping

coherence is a practical proxy for unwrapping difficulty. Where decorrelation is strong, phase gradients become unreliable, residues accumulate, and the risk of error propagation increases markedly.

As coherence decreases, the reliability of the measured phase also decreases. The immediate effect is an increase in phase ambiguity and a higher probability of phase-unwrapping errors, often expressed as spurious 2π jumps and local inconsistencies in the final unwrapped field. Coherence loss is therefore a primary source of uncertainty in phase interpretation and one of the main determinants of downstream InSAR accuracy.

2.6 Wrapped Phase, Absolute Phase, and Integer Ambiguity

The interferometric phase observed by the sensor is not the unbounded absolute phase but its modulo-2π representation. If ϕ denotes the absolute phase, the wrapped phase ϕ_w is restricted to the principal interval $(-\pi, \pi]$ [4, 37]:

$$\phi_w = \mathrm{wrap}(\phi) = ((\phi + \pi) \mod 2\pi) - \pi \tag{2.9}$$

Equivalently, the absolute phase can be written as:

$$\phi = \phi_w + 2\pi k, \quad k \in \mathbb{Z} \tag{2.10}$$

The unknown integer k is the ambiguity, or fringe order, that must be estimated for each pixel. This discrete ambiguity is the core of the phase-unwrapping problem. Wrapped phase alone does not determine a unique continuous solution unless additional constraints are introduced through spatial regularity, redundancy, statistical priors, or physical modelling [38].

The wrapped phase preserves local phase information only within the principal interval. Phase unwrapping therefore consists of estimating the correct integer number of 2π cycles that must be restored to recover the continuous phase field.

The key point is that the discontinuities visible in the wrapped phase are often not true physical discontinuities in the underlying field. They are artefacts of periodic folding. Unwrapping seeks to reverse that folding while preserving genuine structural breaks where they actually exist.

2.7 Itoh Condition, Residues, and Path Dependence

A sufficient local condition for path-independent phase integration is the Itoh condition, which requires the absolute phase difference between adjacent pixels to remain below π in magnitude [37–39]:

$$|\Delta\phi| < \pi \tag{2.11}$$

When this condition holds, the wrapped phase difference equals the true phase gradient and local integration is well posed. In real interferograms, however, steep topography, strong deformation gradients, under-sampling, and decorrelation frequently violate this assumption. The result is cycle ambiguity and path dependence in local phase integration.

Such violations appear as phase residues. A residue is detected by summing wrapped phase differences around a closed elementary loop, typically a 2×2 pixel cell. A non-zero circulation indicates that local phase integration is inconsistent and that the unwrapping algorithm must explicitly manage this inconsistency [9, 13, 40].

$$\sum_{\square} \mathrm{wrap}(\Delta\phi_w) = \pm 2\pi \tag{2.12}$$

Table 2.4: Conditions under which local phase integration succeeds or fails.

Condition	Mathematical meaning	Expected behavior	Consequence
Itoh satisfied	$\lvert\Delta\phi\rvert < \pi$ between neighbours	Wrapped gradients equal true gradients	Path-independent local integration
Strong gradient / under-sampling	$\lvert\Delta\phi\rvert \geq \pi$ locally	Gradient aliasing and cycle ambiguity	Need global or guided strategies
Noise and decorrelation	Apparent gradient spikes unrelated to terrain or deformation	False residues and inconsistent loops	Higher risk of error propagation
True discontinuity	Physical jump in phase field or line-of-sight motion	Continuity assumption invalid	Discontinuity-preserving methods preferred

2.8 Baseline Geometry

InSAR geometry refers to the geometric relationship between the radar sensor and a ground target observed from two slightly different positions. In this configuration, the same target is seen with two slightly different slant-range distances, commonly denoted R and $R + \delta R$. Although this path difference is very small, it produces a measurable phase difference between the two radar signals. This interferometric phase difference forms the basis for estimating terrain elevation or surface deformation [1, 2, 25].

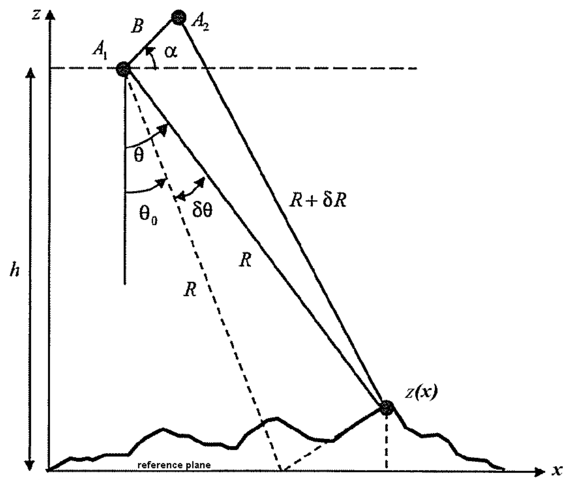

Figure 2.7: Basic InSAR geometry showing two slightly different radar path lengths.

As shown in Figure 2.7, the same ground target is illuminated from two nearby radar positions, resulting in two slightly different slant-range distances. The difference between these path lengths generates an interferometric phase difference, which is the key observable used in InSAR to retrieve topographic height or ground displacement.

2.9 Interferometric SAR Processing

The production of interferometric SAR products follows a structured processing chain through which coherent radar observations are transformed into topographic or deformation-related information. The process begins with the acquisition of two SAR datasets over the same scene, from which two complex SAR images are generated. These images must then be co-registered with sub-pixel precision so that corresponding pixels refer to the same ground targets.

Once registration is achieved, the interferogram is formed by combining the two complex images. The resulting phase contains contributions from terrain elevation, surface displacement, atmospheric delay, orbital errors, and noise. Subsequent processing steps include flat-earth removal, coherence analysis, phase unwrapping, phase-to-height conversion, geometric correction, and geocoding.The main stages of the interferometric SAR workflow are summarized in Figure 2.8

As shown in Figure 2.8, phase unwrapping is a key intermediate step in the InSAR workflow. Because the measured interferometric phase is wrapped modulo $2\pi 2\pi 2\pi$,

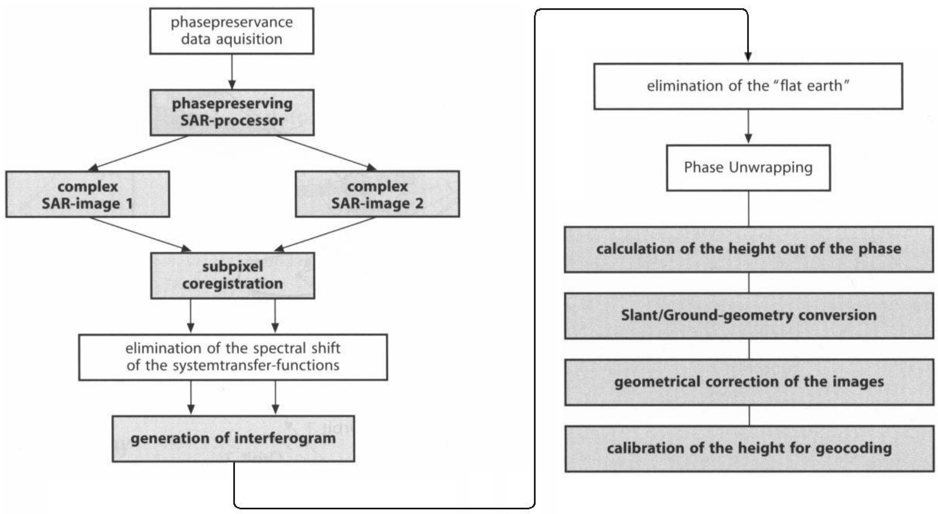

Figure 2.8: Simplified interferometric SAR processing chain
, showing the progression from phase-preserving SAR acquisition and complex image formation to sub-pixel coregistration, interferogram generation, flat-earth removal, phase unwrapping, height retrieval, geometric correction, and geocoding.

it must be transformed into a continuous phase field before meaningful elevation or deformation estimates can be obtained. Errors introduced at this stage propagate into all subsequent products. Therefore, robust phase unwrapping is essential for reliable InSAR analysis and constitutes a core concern of this thesis.

2.10 Why Phase Unwrapping Becomes Difficult in Practice

From an algorithmic perspective, the main difficulty of InSAR phase unwrapping does not lie in the modulo-2π relationship itself. It lies in the mismatch between the assumptions used by unwrapping algorithms and the conditions encountered in operational scenes. Low-coherence increases phase noise and residue density; steep topography and rapid deformation violate local continuity assumptions; layover and shadow create missing or unreliable observations; and atmospheric or orbital artefacts introduce long-wavelength structures that may be mistaken for geophysical signal.

The practical problem can be summarized as an inversion chain:

complex SAR pair $\rightarrow$ interferogram $\rightarrow$ wrapped phase $\rightarrow$ ambiguity field

$\rightarrow$ unwrapped phase $\rightarrow$ geophysical product

Errors introduced at the ambiguity-resolution stage propagate directly into elevation and deformation estimates [22] [23] [72] For that reason, a phase-unwrapping method that performs well only on smooth synthetic fringes has limited operational value. In contrast, a method that remains stable under low-coherence, dense residues, strong gradients, and partial discontinuities responds to a genuine scientific and engineering need. [73] [89].

2.11 Conclusion

Chapter 2 established the theoretical foundations required to understand SAR, InSAR, and the origin of the phase-unwrapping problem in interferometric radar analysis. It showed that SAR provides complex-valued observations whose amplitude and phase encode complementary information about the Earth's surface, while InSAR exploits phase differences between co-registered SAR acquisitions to retrieve topographic and deformation-related signals. It further clarified that the interferometric phase is not a direct geophysical measurement, but a composite observable influenced by acquisition geometry, atmospheric propagation, orbital inaccuracies, surface decorrelation, and measurement noise. Particular emphasis was placed on the central role of coherence, decorrelation, and baseline geometry in determining phase quality and interpretability. These factors directly affect whether the wrapped phase can be reliably transformed into a continuous absolute phase. The discussion of wrapped phase, ambiguity, the Itoh condition, and phase residues demonstrated that phase unwrapping is not merely a numerical post-processing operation, but a fundamental inverse problem arising from the physics and geometry of SAR interferometry itself.

By identifying the physical and mathematical sources of phase discontinuitiesThis theoretical foundation provides the basis for the methodological contributions developed in the remainder of the thesis. In particular, it motivates the need for phase-unwrapping approaches that are robust to noise, decorrelation, low-coherence regions, and phase inconsistencies. These challenges define the context in which the proposed work is positioned: improving the reliability, stability, and interpretability of phase-unwrapping results under realistic InSAR conditions.

Consequently, the chapter does more than introduce background concepts; it establishes the problem setting that justifies the subsequent contribution of this thesis. The practical difficulty of InSAR analysis lies not only in generating interferograms, but in recovering a stable and physically meaningful continuous phase from wrapped observations affected by noise, discontinuities, and decorrelation. On this foundation, the next chapter examines the principal families of phase-unwrapping methods, analyzes their limitations, and prepares the ground for the proposed methodological developments presented later in the thesis.

Chapter 3

Review of interferometric synthetic aperture radar phase unwrapping

3.1 Introduction

Phase unwrapping in InSAR is the task of reconstructing a continuous phase field from observations available only modulo 2π. Although the definition is compact, the practical problem is difficult because several constraints interact simultaneously: local continuity may be violated, the integer ambiguity field is unknown, noise and decorrelation distort the measured gradients, and large images amplify the consequences of local mistakes through error propagation [4, 7, 15].

The difficulty of phase unwrapping lies not only in the presence of ambiguity, but in the fact that ambiguity must be resolved under imperfect and often contradictory conditions. In real interferograms, low- coherence, steep phase gradients, shadow and layover, and atmospheric disturbances frequently lead to violations of local consistency assumptions. As a result, the reconstruction process becomes highly sensitive to local decisions, and small errors may propagate across large spatial regions, degrading the final solution. A useful review of the literature must therefore do more than list algorithms; it must explain which assumptions each family makes about the phase field, under which conditions those assumptions are reasonable, and how failure occurs when they are not [25, 28, 89].

Over the past decades, a wide range of approaches has been developed to address these challenges. These methods differ not only in their algorithmic design, but also in their interpretation of the phase unwrapping problem itself. Classical single-baseline methods rely on local continuity and heuristic strategies to guide the unwrapping process. Global and optimization-based approaches attempt to enforce consistency at the level of the entire interferogram. Multibaseline and network-based methods introduce redundancy to improve ambiguity resolution, while recent deep learning approaches aim to learn phase reconstruction directly from data. Each of these families represents a different compromise between robustness, computational complexity, and dependence on prior information.

Rather than treating these approaches as independent solutions, it is more meaningful to view them as different responses to a common underlying problem: the recovery of a globally consistent phase field from incomplete and noisy observations. This perspective highlights that no single method is universally optimal, and that the effectiveness of a given approach depends strongly on the characteristics of the interferogram, including coherence level, deformation pattern, and data scale.

To structure this diversity, Figure 3.1 presents a taxonomy of phase unwrapping methods in InSAR, highlighting the main methodological families and their evolution from classical spatial techniques toward network-based, optimization-driven, and learning-based frameworks. This taxonomy serves as a guide for the organization of the chapter.

The objective of this chapter is therefore not only to review existing methods, but to analyze them critically by examining their assumptions, strengths, and limitations. Particular attention is given to their robustness to noise and decorrelation, their ability to preserve true discontinuities, their computational scalability, and their dependence on handcrafted priors or training data. This analysis leads directly to the identification of key research gaps, which motivate the contributions developed in the following chapters.

3.2 Methodological Organization of Phase Unwrapping Approaches

Phase unwrapping methods in InSAR have evolved into a diverse set of approaches that differ in their underlying assumptions, problem formulations, and mechanisms for enforcing phase consistency. This diversity reflects the intrinsic complexity of the phase unwrapping problem, which requires the resolution of integer ambiguity under conditions of noise, decorrelation, and structural discontinuities. A structured organization of these methods is therefore necessary to clarify their relationships and to establish a coherent framework for analysis.

From a methodological perspective, phase unwrapping approaches can be classified according to the way ambiguity is constrained and how consistency is enforced across the phase field. Some methods rely primarily on local continuity assumptions and propagate phase information through spatial neighborhoods. Others formulate the problem at a global level, enforcing consistency through optimization or statistical inference. Additional approaches exploit redundancy across multiple interferograms or temporal acquisitions, while more recent methods adopt data-driven strategies to infer phase structure from training data.

Figure 3.1 presents a taxonomy of InSAR phase unwrapping methods based on these principles. The diagram organizes existing approaches into four main families: classical single-interferogram methods, optimization-based methods, multibaseline and network-based approaches, and learning-based methods. Each family represents a distinct interpretation of the phase unwrapping problem and corresponds to a specific strategy for addressing ambiguity, noise, and discontinuities.

Classical methods operate on a single interferogram and are based on the assumption that local phase continuity can be exploited to reconstruct the absolute phase. These approaches typically rely on path-following strategies, heuristic guidance, or local regularization mechanisms. In contrast, optimization-based methods recast phase unwrapping as a global estimation problem, where ambiguity is resolved by minimizing a cost function or by enforcing statistical consistency across the entire domain.

Multibaseline and network-based approaches extend the problem formulation by incorporating additional information from multiple interferograms or temporal stacks. In

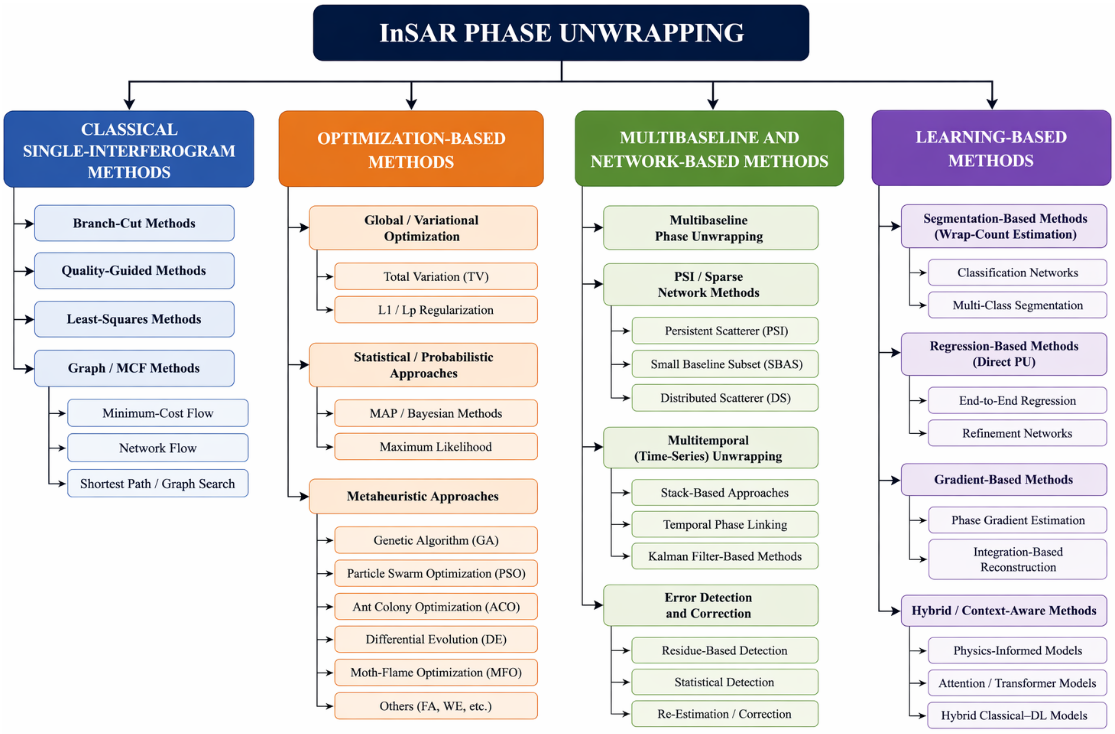

Figure 3.1: Taxonomy of InSAR phase unwrapping methods.

these methods, phase unwrapping is no longer treated as a purely spatial problem, but rather as a graph- or network-based inference problem, where ambiguity is constrained through redundancy and relational structure. Learning-based methods represent a further shift in perspective, introducing data-driven models that attempt to learn phase reconstruction directly from examples, often without relying explicitly on handcrafted continuity constraints.

This classification highlights the progression of phase unwrapping methodologies from local and heuristic strategies toward global, network-based, and data-driven formulations. It also provides the conceptual basis for the detailed examination of each method family in the following sections, where their respective assumptions, strengths, and limitations are analyzed in a systematic manner.

3.3 Classical Single-Interferogram Phase Unwrapping Methods

Classical single-interferogram phase unwrapping methods constitute the foundational approaches to resolving phase ambiguity in InSAR. These methods operate on a single interferogram and rely on the assumption that local phase continuity can be exploited to reconstruct the absolute phase field, provided that inconsistencies remain limited or can be effectively controlled [4, 6, 7].

The phase ambiguity addressed by these methods originates from the periodic nature of the measured interferometric phase. The relationship between the observed wrapped phase and the desired continuous phase can be expressed as:

$$\psi(x, y) = \phi(x, y) - 2\pi k(x, y) \tag{3.1}$$

where $\psi(x, y)$ represents the wrapped interferometric phase measured from the interferogram, $\phi(x, y)$ denotes the unknown absolute phase, and $k(x, y)$ is an integer ambiguity function representing the number of 2π phase cycles removed during the wrapping process. Therefore, phase unwrapping aims to estimate $k(x, y)$ in order to recover the continuous phase according to:

$$\phi(x, y) = \psi(x, y) + 2\pi k(x, y) \tag{3.2}$$

where the estimation of the integer field $k(x, y)$ constitutes the main challenge, especially in the presence of noise, phase discontinuities, and decorrelated regions.

Rather than representing minor algorithmic variations, classical methods reflect distinct strategies for managing ambiguity and controlling error propagation. The main methodological families include path-following approaches, global least-squares formulations, and graph-based optimization methods.

3.3.1 Path-Following Strategies

Path-following methods reconstruct the phase field by integrating wrapped phase gradients along selected paths. Their performance depends critically on how integration paths are defined and how inconsistent regions are avoided.

Branch-Cut Methods

Branch-cut methods explicitly identify phase residues and connect them through artificial discontinuity lines that prevent integration across inconsistent regions [7, 90–92].

This formulation provides a direct and physically interpretable mechanism for isolating ambiguity.

The principal contribution of this family lies in its explicit treatment of local inconsistency. By constraining integration paths, branch-cut methods prevent the accumulation of phase errors along unreliable trajectories. However, their effectiveness depends strongly on the spatial distribution of residues. In low-coherence interferograms, where residue density is high, the resulting network of cuts may become overly complex, isolating large regions or forcing integration along suboptimal paths.

Quality-Guided Methods

Quality-guided methods address the limitations of fixed path selection by introducing a reliability-based ordering of the unwrapping process. Pixels are unwrapped according to a predefined quality metric, such as coherence, phase-derivative variance, or gradient stability [6, 36, 38, 89].

The key contribution of these methods is the prioritization of reliable phase information, allowing stable regions to guide the reconstruction of more uncertain areas. This significantly improves robustness in heterogeneous interferograms. However, the quality map is typically fixed prior to unwrapping and does not adapt to evolving reconstruction conditions. As a result, performance is highly dependent on the chosen metric, and mismatches between the metric and actual phase reliability can lead to systematic errors.

3.3.2 Global Least-Squares and Minimum-Norm Methods

Global methods reformulate phase unwrapping as a reconstruction problem in which the objective is to estimate a phase field whose gradients best match the wrapped observations in a least-squares or minimum-norm sense [96, 98].

The principal contribution of these approaches is the enforcement of global consistency. By considering the entire interferogram simultaneously, they reduce sensitivity to local integration errors and improve numerical stability.

However, this global regularization introduces an inherent limitation. In order to produce stable solutions, these methods tend to impose smoothness constraints, which may attenuate or eliminate genuine phase discontinuities. This limitation becomes particularly critical in applications involving sharp deformation gradients, such as fault ruptures or landslides [99, 102, 103]. Consequently, least-squares methods are well suited for smooth phase fields but less effective when discontinuity preservation is required.

3.3.3 Graph-Based and Minimum-Cost Flow Methods

Graph-based methods represent phase unwrapping as a network optimization problem. In minimum-cost flow (MCF) formulations, phase residues are treated as sources and sinks, and the objective is to determine a flow configuration that minimizes a cost function while ensuring global consistency [26, 27].

A key contribution in this domain is the formulation of phase unwrapping as a network programming problem by Costantini [40], which enables efficient optimization under global consistency constraints. Similarly, Chen and Zebker [51] demonstrated the effectiveness of incorporating statistical cost functions into the unwrapping process, leading to improved robustness in noisy conditions.

Graph-based methods provide a balance between local flexibility and global consistency. They are generally more robust than purely local approaches, particularly in complex residue configurations. However, this robustness comes at the cost of increased computational complexity. The construction and solution of large-scale graphs may become resource-intensive for high-resolution interferograms or large datasets [100, 101].

3.3.4 Comparative Analysis of Classical Methods

The differences between classical phase unwrapping methods can be interpreted in terms of how they balance local decision-making and global consistency. Path-following methods rely on local continuity and are therefore sensitive to noise and residue distribution. Global least-squares methods reduce local error propagation but may over-smooth discontinuities. Graph-based approaches achieve improved robustness by enforcing global constraints, at the expense of increased computational cost.

Overall, classical methods remain essential due to their strong theoretical foundations and practical efficiency. However, their limitations become increasingly evident

Table 3.1: Comparison of classical single-interferogram phase unwrapping methods.

Method Family	Key Contribution	Strengths	Limitations
Branch-cut methods	Explicit isolation of phase residues and inconsistency control	Conceptual clarity, effective error containment in sparse residue fields	Performance degrades in high residue density, may isolate large regions
Quality-guided methods	Reliability-based integration ordering	Improved robustness in heterogeneous scenes, adaptive propagation from stable regions	Strong dependence on predefined quality map, limited adaptability
Least-squares methods	Global consistency through variational reconstruction	Numerical stability, reduced local error propagation	Oversmoothing of discontinuities, loss of sharp phase features
Graph-based (MCF) methods	Global combinatorial optimization with cost minimization	High robustness in complex residue configurations, flexible cost modeling	High computational cost, scalability limitations

in challenging scenarios characterized by low-coherence, strong phase gradients, or large-scale datasets. These limitations motivate the development of more advanced approaches, including optimization-based, multibaseline, and learning-based methods, which aim to overcome the constraints inherent in single-interferogram formulations.

3.4 Optimization-Based Phase Unwrapping Methods

Optimization-based phase unwrapping methods extend classical formulations by explicitly casting the reconstruction problem as a global optimization task. Instead of relying solely on local continuity or heuristic path selection, these approaches seek a phase solution that minimizes a predefined cost function or satisfies a set of global consistency constraints. This formulation provides a principled framework for controlling ambiguity under noisy and inconsistent conditions.

In general, optimization-based phase unwrapping can be formulated as the search for the optimal phase field $\hat{\phi}$ that minimizes an objective function:

$$\hat{\phi} = \arg\min_{\phi} J(\phi) \tag{3.3}$$

where $\hat{\phi}$ denotes the estimated continuous phase, ϕ represents a candidate phase solution, and $J(\phi)$ is an objective (or cost) function that measures the consistency between the reconstructed phase and the observed interferometric measurements. The design of $J(\phi)$ distinguishes different optimization methods and determines their robustness to noise and phase discontinuities.

3.4.1 Global Optimization Formulations

Early developments in this direction focused on expressing phase unwrapping as a minimum-discontinuity or minimum-error problem. Costantini demonstrated that phase unwrapping can be formulated as a network programming problem, enabling efficient solutions through minimum-cost flow (MCF) optimization [41]. This approach enforces global consistency by distributing phase discontinuities in a way that minimizes an overall cost function.

The corresponding optimization problem can be generally expressed as:

$$J(\phi) = \sum_{(i,j)\in E} c_{ij} f_{ij} \tag{3.4}$$

where E denotes the set of graph edges, f_{ij} represents the flow assigned between neighboring nodes, and c_{ij} is the corresponding transportation cost. Minimizing this objective ensures that phase inconsistencies are distributed with minimum global cost while satisfying residue conservation constraints.

Similarly, Chen and Zebker introduced statistical-cost formulations, showing that phase unwrapping can be treated within a probabilistic framework [52]. By incorporating noise statistics and prior information into the cost function, these methods improve robustness in low-coherence and noisy interferograms. Such formulations are particularly influential in operational systems, where statistical modeling plays a central role in balancing data fidelity and regularization.

From a statistical perspective, the reconstruction problem may be formulated as a

Maximum A Posteriori (MAP) estimation problem:

$$\hat{\phi} = \arg\max_{\phi} P(\phi \mid \psi) \tag{3.5}$$

where $P(\phi \mid \psi)$ denotes the posterior probability of the continuous phase ϕ given the observed wrapped phase ψ. Applying Bayes' theorem yields

$$P(\phi \mid \psi) \propto P(\psi \mid \phi)\, P(\phi) \tag{3.6}$$

where $P(\psi \mid \phi)$ represents the likelihood function describing the measurement model, and $P(\phi)$ is the prior distribution that regularizes the reconstructed phase field.

A notable implementation of this class of methods is SNAPHU, which combines statistical cost modeling with network-flow optimization and remains widely used in practical InSAR processing workflows [52]. The success of such approaches highlights the importance of integrating physical modeling with global optimization.

While global optimization methods significantly improve robustness compared to purely local strategies, they introduce new challenges. Their performance depends strongly on the choice of cost function, regularization terms, and prior assumptions. Inaccurate modeling may lead to suboptimal solutions or bias in the reconstructed phase field.

3.4.2 Metaheuristic Optimization Approaches

In addition to deterministic formulations, metaheuristic optimization methods have been explored as alternative strategies for solving the phase unwrapping problem. These approaches are particularly attractive in scenarios where the optimization landscape is complex, non-convex, or difficult to model analytically.

Unlike deterministic optimization, metaheuristic algorithms iteratively update a population of candidate solutions according to a general optimization framework:

$$X^{t+1} = F(X^t, \Theta) \tag{3.7}$$

where X^t denotes the population of candidate solutions at iteration t, $F(\cdot)$ represents the update mechanism of the optimization algorithm, and Θ denotes the set of algorithm-specific parameters. The objective is to progressively minimize the predefined cost function while avoiding convergence toward poor local minima.

Genetic Algorithm (GA)

Genetic algorithms provide a population-based search strategy capable of exploring a wide solution space through crossover and mutation operations. Their main contribution lies in their flexibility and ability to escape local minima. However, they typically require careful parameter tuning and may exhibit slow convergence.

The evolution of a population can be represented as

$$P^{t+1} = M\left(C\left(S(P^t)\right)\right) \tag{3.8}$$

where P^t is the population at generation t, S denotes the selection operator, C the crossover operator, and M the mutation operator.

Particle Swarm Optimization (PSO)

Particle swarm optimization (PSO) offers a simpler implementation based on collective behavior and velocity-driven search dynamics. It requires fewer control parameters and converges relatively quickly in many cases. Nevertheless, it may suffer from premature convergence and stagnation near local optima.

Each particle updates its velocity and position according to

$$v_i^{t+1} = wv_i^t + c_1 r_1(p_i - x_i^t) + c_2 r_2(g - x_i^t) \tag{3.9}$$

where x_i is the particle position, v_i is its velocity, p_i is the personal best solution, g is the global best solution, w is the inertia weight, and c_1, c_2 are acceleration coefficients with random variables $r_1, r_2 \in [0, 1]$.

Ant Colony Optimization (ACO)

Ant colony optimization (ACO) is particularly suited to path-construction problems, making it conceptually compatible with phase unwrapping. By simulating collective probabilistic exploration, it can identify efficient unwrapping paths. However, its computational cost increases significantly with problem size, limiting its scalability.

The probability of selecting the next path is computed as

$$P_{ij} = \frac{\tau_{ij}^{\alpha}\eta_{ij}^{\beta}}{\sum_{k\in N_i}\tau_{ik}^{\alpha}\eta_{ik}^{\beta}} \tag{3.10}$$

where τ_{ij} denotes the pheromone concentration, η_{ij} is the heuristic desirability, and α and β control their relative influence.

Multi-Verse Optimizer (MVO)

The Multi-Verse Optimizer (MVO) introduces a balance between exploration and exploitation through mechanisms inspired by cosmological models. Its design allows for efficient search in compact solution spaces while maintaining diversity in candidate solutions. However, as with other metaheuristics, repeated objective-function evaluations can be computationally expensive, and performance remains sensitive to problem formulation and parameter settings.

The population of universes can be represented as

$$U = \begin{bmatrix} x_{11} & x_{12} & \cdots & x_{1d} \\ x_{21} & x_{22} & \cdots & x_{2d} \\ \vdots & \vdots & \ddots & \vdots \\ x_{n1} & x_{n2} & \cdots & x_{nd} \end{bmatrix} \tag{3.11}$$

where n is the number of candidate universes and d is the number of optimization variables. Each universe corresponds to one candidate solution whose quality is evaluated through the objective function.

The exploration–exploitation balance is controlled by the Wormhole Existence Probability (WEP) and the Travelling Distance Rate (TDR), commonly expressed as

$$\mathrm{WEP} = \mathrm{WEP}_{\min} + \frac{l}{L}\left(\mathrm{WEP}_{\max} - \mathrm{WEP}_{\min}\right), \qquad \mathrm{TDR} = 1 - \left(\frac{l}{L}\right)^{1/p} \tag{3.12}$$

where l is the current iteration, L is the maximum number of iterations, and p is a user-defined exploitation parameter. These adaptive mechanisms gradually shift the search from exploration toward exploitation as the optimization progresses.

Overall, metaheuristic methods provide a flexible framework for phase unwrapping, particularly in situations where classical deterministic approaches are difficult to apply. However, their effectiveness depends strongly on the definition of the objective function and the tuning of algorithmic parameters.

3.4.3 Comparative Analysis of Optimization-Based Methods

Optimization-based phase unwrapping methods can be broadly categorized into deterministic global formulations and stochastic metaheuristic approaches. Deterministic methods, such as minimum-cost flow and statistical-cost formulations, provide strong theoretical guarantees and enforce global consistency. They are particularly effective in structured problems where the cost function accurately reflects the underlying phase behavior.

In contrast, metaheuristic methods offer greater flexibility in exploring complex solution spaces and can be applied to non-convex or poorly modeled problems. However, this flexibility comes at the cost of reduced interpretability, increased computational demand, and sensitivity to parameter selection.

From a broader perspective, optimization-based methods represent a transition from heuristic and local strategies toward principled global formulations. They address several limitations of classical approaches, particularly in terms of robustness to noise and consistency enforcement. However, they do not fully resolve the challenges associated with large-scale processing, parameter dependency, and adaptability to diverse interferometric conditions.

Conceptually, the optimization objective shared by these methods can be summarized as

$$\hat{\phi} = \arg\min_{\phi} \left[D(\phi, \psi) + \lambda R(\phi) \right] \tag{3.13}$$

where $D(\phi, \psi)$ is a data-fidelity term measuring agreement with the observed wrapped phase, $R(\phi)$ is a regularization term enforcing smoothness or consistency, and λ controls the trade-off between both objectives. Although different optimization algorithms employ different search mechanisms, they ultimately seek to minimize a formulation of this general form.

These limitations motivate the need for approaches that combine the strengths of global optimization with adaptive guidance mechanisms and improved handling of complex phase patterns, as explored in the contributions of this thesis.

Table 3.2: Comparison of optimization-based phase unwrapping methods.

Method Family	Key Contribution	Strengths	Limitations
Minimum-cost flow (MCF)	Global combinatorial optimization of phase ambiguity	Strong global consistency, robust in complex residue patterns	High computational cost, scalability limitations
Statistical/MAP methods	Incorporation of noise models and prior information	Improved robustness in noisy conditions, physically meaningful solutions	Dependence on model assumptions and parameter tuning
Genetic algorithms	Population-based global search	Strong exploration capability, flexible formulation	Slow convergence, many hyperparameters
Particle swarm optimization	Velocity-driven collective search	Simple implementation, fewer parameters	Risk of local stagnation, limited global guarantees
Ant colony optimization	Probabilistic path construction	Natural fit for path-based problems	High computational cost in large-scale problems
Multi-Verse Optimizer	Balanced exploration–exploitation strategy	Efficient search in compact spaces, adaptable framework	Computational cost of objective evaluations, parameter sensitivity

3.5 Multibaseline and Network-Based Phase Unwrapping Methods

Multibaseline and network-based phase unwrapping methods extend the classical single-interferogram formulation by incorporating additional information from multiple interferograms or temporal acquisitions. These approaches exploit redundancy to improve ambiguity resolution and reduce the dependence on local continuity assumptions. As a result, the phase unwrapping problem is no longer treated solely as a spatial reconstruction task, but rather as a structured inference problem defined over multiple observations.

3.5.1 Multibaseline Phase Unwrapping

Multibaseline phase unwrapping uses several interferograms acquired with different baselines or temporal separations to constrain phase ambiguity. The central contribution of this approach lies in the exploitation of redundancy, which effectively enlarges the unambiguous phase interval and improves robustness in regions characterized by dense fringes or strong deformation gradients [32, 41, 42].

For a set of N interferograms, the wrapped phase observations can be represented as

$$\psi_i(x, y) = \phi_i(x, y) - 2\pi k_i(x, y), \qquad i = 1, 2, \ldots, N \tag{3.14}$$

where $\psi_i(x, y)$ is the wrapped phase of the ith interferogram, $\phi_i(x, y)$ is the corresponding continuous phase, and $k_i(x, y)$ denotes the associated integer ambiguity. The availability of multiple observations provides additional constraints that facilitate the estimation of the ambiguity terms.

This strategy is particularly advantageous in scenarios where a single interferogram is insufficient for reliable unwrapping, such as areas with steep topography or rapid surface deformation [45–47]. By combining multiple observations, multibaseline methods reduce reliance on local phase continuity and enable more stable reconstruction.

The reconstruction is commonly formulated as a joint optimization problem,

$$\hat{\phi} = \arg\min_{\phi} \sum_{i=1}^{N} J_i(\phi) \tag{3.15}$$

where $J_i(\phi)$ represents the cost associated with the ith interferogram. The objective is to determine a phase solution that simultaneously satisfies all available interferometric observations.

However, the effectiveness of multibaseline approaches depends on several conditions. Accurate co-registration, appropriate baseline selection, and consistent noise characteristics are required to ensure reliable performance. In addition, the increased data volume and processing complexity introduce practical challenges, including higher computational cost and more demanding preprocessing requirements [45, 46, 48, 49].

Consequently, multibaseline methods are best understood as higher-information formulations whose benefits depend on acquisition design and data quality [50–53].

3.5.2 Network and Sparse Representation Approaches

The development of persistent scatterer interferometry (PSI) and related techniques has led to a shift from regular grid-based processing toward sparse network representations. In these approaches, phase unwrapping is performed on a graph, where nodes represent reliable scatterers and edges encode relationships such as spatial proximity, temporal coherence, or similarity [1].

The network can be represented mathematically as

$$G = (V, E) \tag{3.16}$$

where V denotes the set of persistent scatterers (graph nodes) and E denotes the set of edges connecting neighboring scatterers. Each edge represents a phase observation between two reliable measurement points.

For every connected pair of nodes, the measured phase difference can be expressed as

$$\Delta\phi_{ij} = \phi_j - \phi_i \tag{3.17}$$

where ϕ_i and ϕ_j are the continuous phases associated with nodes i and j, respectively.

A key contribution in this domain is the null-space formulation introduced by Fornaro et al. [31], which demonstrates that ambiguity resolution in multitemporal interferometric stacks can be expressed algebraically rather than through independent two-dimensional unwrapping operations. This formulation highlights the importance of global constraints and network structure in achieving consistent solutions.

The resulting system is commonly written as

$$A\phi = b \tag{3.18}$$

where A is the network incidence matrix describing the graph topology, ϕ is the vector of unknown continuous phases, and b contains the measured phase differences between connected scatterers.

Network-based approaches offer several advantages. By focusing on high-quality scatterers, they reduce sensitivity to noise and decorrelation. The graph structure also enables the integration of spatial and temporal information, improving robustness in complex environments.

However, these methods introduce new dependencies. Their performance is strongly influenced by the design of the network, including scatterer selection, edge definition, and weighting strategies. Errors in network construction may propagate through the entire graph, affecting the final solution. As a result, phase unwrapping becomes inseparable from the broader problem of network modeling and data selection.

3.5.3 Multitemporal and Time-Series Unwrapping

The extension of InSAR analysis to long temporal stacks has further transformed phase unwrapping into a spatio-temporal problem. Instead of processing interferograms independently, multitemporal methods exploit temporal redundancy to improve ambiguity resolution and consistency across acquisitions.

For a temporal stack composed of T acquisitions, the phase evolution can be represented as

$$\phi = \begin{bmatrix} \phi_1 \\ \phi_2 \\ \vdots \\ \phi_T \end{bmatrix} \tag{3.19}$$

where ϕ_t denotes the continuous phase corresponding to acquisition time t.

The reconstruction problem is generally formulated as

$$\hat{\phi} = \arg\min_{\phi} \left[J_s(\phi) + \lambda J_t(\phi) \right] \tag{3.20}$$

where $J_s(\phi)$ represents the spatial consistency term, $J_t(\phi)$ denotes the temporal consistency term, and λ balances their relative contributions.

This approach enables the identification of stable phase trends and reduces the impact of isolated errors. By enforcing consistency across time, multitemporal unwrapping improves robustness in the presence of noise and decorrelation.

However, the increased dimensionality of the problem introduces additional complexity. Temporal modeling, noise accumulation, and the management of large datasets become critical factors. Furthermore, inconsistencies in individual interferograms may propagate through the temporal network, affecting long-term deformation estimates.

3.5.4 Error Detection and Correction in Time-Series InSAR

An important development in multitemporal phase unwrapping is the recognition that initial unwrapping solutions are not always reliable and may require correction. This has led to the development of dedicated error detection and correction methods, particularly in the context of time-series analysis.

The consistency of multiple interferograms can be evaluated using the phase closure relation,

$$\phi_{12} + \phi_{23} - \phi_{13} = 0 \tag{3.21}$$

where ϕ_{12}, ϕ_{23}, and ϕ_{13} denote the interferometric phases corresponding to three acquisitions. Ideally, the closure error should be zero; any deviation indicates the presence of phase inconsistencies or unwrapping errors.

A representative contribution is the 3D-ADAC method [40], which combines closure phase analysis, phase gradients, and interferogram edge information to detect and correct unwrapping errors. The method operates iteratively, first addressing spatial inconsistencies and then refining the solution in the temporal domain.

The correction process can be formulated as

$$\phi^{(k+1)} = \phi^{(k)} + \Delta\phi \tag{3.22}$$

where $\phi^{(k)}$ denotes the reconstructed phase at iteration k, and $\Delta\phi$ is the correction term estimated from the detected inconsistencies. The iterative process continues until a predefined convergence criterion is satisfied.

This line of work reflects a broader shift in perspective, where phase unwrapping is no longer treated as a one-step preprocessing operation, but as part of an integrated quality-control framework. While these methods improve reliability, they also increase computational complexity and require additional modeling assumptions.

3.5.5 Comparative Analysis of Multibaseline and Network-Based Methods

Multibaseline and network-based approaches represent a significant advancement over classical methods by incorporating additional information and enforcing consistency across multiple dimensions. Their primary strength lies in the use of redundancy, which reduces reliance on local continuity and improves robustness in challenging conditions.

However, this improvement comes at the cost of increased complexity. These methods require more data, more sophisticated preprocessing, and careful design of acquisition geometry or network structure. Their performance is therefore highly dependent on data quality, availability, and modeling choices.

Overall, these methods mark a transition from purely spatial phase unwrapping toward more comprehensive frameworks that integrate spatial, temporal, and structural information. While they significantly enhance robustness and consistency, they also introduce new challenges related to scalability, data requirements, and model dependency. These limitations motivate the exploration of alternative approaches capable of balancing robustness, adaptability, and computational efficiency.

3.6 Learning-Based Phase Unwrapping Methods

Recent advances in machine learning have introduced a fundamentally different perspective on the phase unwrapping problem. Instead of relying exclusively on hand-

Table 3.3: Comparison of multibaseline and network-based phase unwrapping methods.

Method Family	Key Contribution	Strengths	Limitations
Multibaseline methods	Redundancy-based ambiguity resolution	Improved robustness in dense fringes and steep gradients	Requires multiple acquisitions, higher preprocessing complexity
Sparse network (PSI) methods	Graph-based representation of phase relationships	Reduced sensitivity to noise, integration of spatial and temporal information	Dependence on network design and scatterer selection
Multitemporal methods	Spatio-temporal consistency enforcement	Improved stability over time, reduced local error impact	Increased computational complexity, sensitivity to temporal inconsistencies
Error correction methods	Post-processing refinement of unwrapping errors	Improved reliability and accuracy	Additional computational cost, reliance on correction models

crafted rules, local continuity assumptions, or predefined optimization criteria, learning-based approaches attempt to infer the mapping between wrapped and unwrapped phase directly from data. This shift reflects the observation that ambiguity patterns in interferometric data are often structured and context-dependent, making them difficult to model analytically [8, 10, 54, 55].

Learning-based phase unwrapping can generally be expressed as a nonlinear mapping

$$\hat{\phi} = F_\theta(\psi) \tag{3.23}$$

where ψ denotes the wrapped phase image, $\hat{\phi}$ is the predicted continuous phase, $F_\theta(\cdot)$ represents the neural network, and θ denotes the set of trainable parameters. During training, the network learns the optimal parameters by minimizing a predefined loss function over a set of wrapped–unwrapped image pairs.

Learning-based methods differ not only in architecture but also in how the phase unwrapping problem is formulated. Broadly, these approaches can be categorized into segmentation-based models, regression-based models, gradient-estimation methods, and hybrid architectures.

3.6.1 Segmentation and Wrap-Count Estimation Approaches

Segmentation-based models treat phase unwrapping as a classification problem in which the objective is to estimate the integer ambiguity, often referred to as wrap count, for each pixel. Early developments in this direction demonstrated that convolutional neural networks (CNNs) can effectively learn local ambiguity patterns and provide accurate wrap-count predictions under controlled conditions [56, 57].

Instead of directly predicting the continuous phase, the network estimates the integer ambiguity map,

$$\hat{k}(x, y) = F_\theta(\psi(x, y)) \tag{3.24}$$

where $\hat{k}(x, y)$ is the predicted wrap count and F_θ denotes the trained classification network.

The continuous phase is then reconstructed as

$$\hat{\phi}(x, y) = \psi(x, y) + 2\pi\hat{k}(x, y) \tag{3.25}$$

where $\psi(x, y)$ is the wrapped phase and $\hat{\phi}(x, y)$ is the reconstructed phase.

Since wrap-count estimation is formulated as a classification problem, the network is commonly trained using the categorical cross-entropy loss

$$L_{\mathrm{CE}} = -\sum_{c=1}^{C} y_c \log(\hat{y}_c) \tag{3.26}$$

where C is the number of wrap-count classes, y_c is the ground-truth label, and $\hat{y}_c$ is the predicted class probability.

The key contribution of this approach lies in its interpretability. By explicitly estimating the ambiguity field, these models provide a clear intermediate representation that can be combined with classical reconstruction techniques. However, this formulation also introduces limitations. The final phase reconstruction typically requires additional post-processing steps to ensure spatial consistency, and errors in classification may propagate into the reconstructed phase field.

3.6.2 Direct Regression Approaches

Regression-based models aim to directly predict the unwrapped phase from the wrapped input. This formulation enables end-to-end reconstruction and reduces the need for intermediate processing stages. Approaches such as U-Net variants and related architectures have demonstrated strong performance in controlled environments, particularly when trained on synthetic datasets [119, 121, 122].

The learning objective is to approximate the nonlinear mapping

$$\hat{\phi} = F_\theta(\psi) \tag{3.27}$$

where the network directly predicts the continuous phase image.

Training is generally performed by minimizing a regression loss such as the Mean Squared Error (MSE),

$$L_{\text{MSE}} = \frac{1}{N} \sum_{i=1}^{N} \left(\phi_i - \hat{\phi}_i \right)^2 \tag{3.28}$$

where N is the number of pixels, ϕ_i is the ground-truth unwrapped phase, and $\hat{\phi}_i$ is the predicted phase.

The principal advantage of regression models is their simplicity and computational efficiency during inference. However, direct prediction of the phase field introduces challenges in maintaining global consistency. Since these models operate primarily on local receptive fields, they may fail to capture long-range dependencies, leading to inconsistencies in large-scale structures or in regions with complex deformation patterns.

For convolutional neural networks, the extracted feature maps are computed through convolution operations,

$$F^{(l)} = \sigma \left(W^{(l)} * F^{(l-1)} + b^{(l)} \right) \tag{3.29}$$

where $F^{(l)}$ is the feature map at layer l, $W^{(l)}$ denotes the convolution kernel, $*$ represents the convolution operator, $b^{(l)}$ is the bias term, and $\sigma(\cdot)$ is the activation function.

3.6.3 Gradient-Based and Hybrid Approaches

To address the limitations of direct regression, several works have proposed hybrid formulations in which the model predicts intermediate quantities, such as phase gradients or confidence maps, that are subsequently used within a classical reconstruction framework [56, 57, 121].

Instead of estimating the absolute phase directly, these methods predict the horizontal and vertical phase gradients,

$$g = \left(\frac{\partial \phi}{\partial x}, \frac{\partial \phi}{\partial y} \right) \tag{3.30}$$

where g represents the gradient field of the continuous phase.

The final phase reconstruction is then obtained by solving

$$\nabla \hat{\phi} = \hat{g} \tag{3.31}$$

where $\hat{g}$ denotes the predicted gradient field. This formulation allows the integration of learned gradient estimates with classical phase integration techniques.

The key contribution of gradient-based approaches is the decomposition of the problem into more stable learning targets. Predicting gradients or reliability measures is often easier than directly estimating the absolute phase, and these quantities can be integrated using established unwrapping techniques. This hybrid strategy improves stability and interpretability, while retaining some of the advantages of data-driven modeling.

More advanced architectures incorporate contextual reasoning mechanisms, including recurrent units, attention mechanisms, and multimodal inputs. Recent developments emphasize the importance of incorporating global context, cycle-consistency constraints, and realistic training data in order to improve robustness and generalization [123–125, 127]. These models represent a transition toward more sophisticated representations capable of capturing long-range dependencies and complex phase patterns.

For recurrent architectures, the hidden state is updated recursively according to

$$h_t = f(x_t, h_{t-1}) \tag{3.32}$$

where x_t is the input feature vector, h_{t-1} is the previous hidden state, and $f(\cdot)$ denotes the recurrent update function. Long Short-Term Memory (LSTM) networks extend this formulation by introducing memory cells and gating mechanisms that preserve long-range spatial dependencies, making them particularly suitable for phase unwrapping problems involving large-scale phase structures. This capability directly motivates the multidirectional LSTM architecture adopted in the proposed VOH-Net framework presented in Chapter 5.

3.6.4 Comparative Analysis of Learning-Based Methods

Learning-based approaches offer several advantages over classical and optimization-based methods. They are capable of modeling complex, nonlinear relationships in the data and can adapt to a wide range of phase patterns without requiring explicit mathematical modeling. Once trained, these models provide fast inference, making them attractive for large-scale applications.

However, these advantages are accompanied by significant limitations. Generalization remains a central challenge, as models trained on synthetic or domain-specific datasets may not perform reliably on real interferograms with different characteristics. In addition, many architectures lack mechanisms for enforcing global consistency, leading to errors in large-scale structures.

Recent developments, including benchmark datasets such as InSAR-DLPU and advanced architectures such as Unwrap-Net, highlight the importance of training realism and cross-domain evaluation in improving model performance [123, 127]. At the same time, studies of large-gradient deformation scenarios indicate that both classical and learning-based methods continue to exhibit failure modes under extreme conditions [108].

From a broader perspective, learning-based phase unwrapping represents a shift from explicit modeling toward data-driven inference. While these methods provide powerful tools for capturing complex phase behavior, they do not yet fully resolve the challenges of generalization, global consistency, and robustness under difficult condi-

Table 3.4: Comparison of learning-based phase unwrapping methods.

Model Family	Key Contribution	Strengths	Limitations
Segmentation (wrap-count) models	Explicit estimation of phase ambiguity	Interpretable representation, compatible with classical solvers	Requires post-processing, sensitive to classification errors
Regression models	Direct end-to-end phase reconstruction	Fast inference, simple pipeline	Limited global consistency, sensitivity to complex structures
Gradient-based models	Prediction of stable intermediate quantities	Improved learning stability, integration with classical methods	Performance depends on downstream reconstruction
Hybrid/context-aware models	Integration of long-range dependencies and contextual reasoning	Improved robustness and adaptability	Higher complexity, increased data and training requirements

tions. These limitations motivate the development of hybrid architectures that combine learned representations with structured reconstruction principles, as explored in the contributions of this thesis.

3.7 Literature Synthesis and Emerging Research Directions

The review of phase unwrapping methods in InSAR highlights that no single approach provides a universally robust solution. Each methodological family addresses specific aspects of the ambiguity problem, resulting in trade-offs between robustness, computational efficiency, and adaptability.

Classical methods remain efficient and conceptually simple, but are sensitive to noise, decorrelation, and error propagation. Optimization-based approaches improve global consistency through cost-function formulations, although their performance depends on parameter selection and computational resources. Multibaseline and network-based methods exploit redundancy to enhance stability, but introduce additional complexity related to data requirements and network design. Learning-based approaches offer powerful data-driven modeling capabilities, yet remain limited by generalization issues and difficulties in enforcing large-scale consistency.

Across these families, two key challenges persist: the reliance on fixed guidance mechanisms that may not adapt to varying data conditions, and the difficulty of maintaining global consistency while capturing complex local structures. These challenges indicate the need for approaches that combine adaptability with structurally consistent reconstruction.

The following chapters build on these observations by exploring complementary directions that address these limitations through both optimization and learning-based strategies.

3.8 Conclusion

This chapter has presented a critical review of phase unwrapping methods in InSAR, covering classical single-interferogram approaches, optimization-based formulations, multibaseline and network-based strategies, and recent learning-based models. The analysis has shown that the evolution of the field reflects a gradual shift from local and heuristic methods toward global, data-driven, and network-based frameworks.

Classical methods provide efficient and interpretable solutions but are limited by their sensitivity to local inconsistencies. Optimization-based approaches improve robustness through global formulations, while multibaseline and network-based methods further enhance performance by exploiting redundancy across spatial and temporal dimensions. More recently, learning-based methods have introduced new possibilities for modeling complex phase patterns, although important challenges remain in terms of generalization and consistency.

Despite these advances, phase unwrapping remains a challenging problem in realistic scenarios characterized by noise, decorrelation, large gradients, and large-scale data. The limitations identified in this chapter highlight the need for approaches that combine robustness, adaptability, and consistency across multiple scales.

The following chapters address these challenges by proposing methods designed to improve the reliability and flexibility of phase unwrapping under diverse and practical conditions.

Chapter 4

An Optimization-Guided Phase Unwrapping Framework using Multi Verse Optimizer

4.1 Introduction

The review presented in the previous chapter highlighted one of the central weaknesses of classical quality-guided phase unwrapping methods: their dependence on predefined reliability maps. In many traditional approaches, the success of the unwrapping process is strongly influenced by the order in which pixels are visited and integrated. This order is usually determined from a quality map derived from measures such as coherence, gradient stability, or phase derivative variance. When the selected quality indicator accurately reflects local phase reliability, the unwrapping path tends to remain stable and error propagation is reduced. However, in practical interferograms affected by noise, decorrelation, dense fringes, and structural complexity, fixed handcrafted quality maps often fail to represent the true difficulty of the phase field.

The problem addressed in this chapter is therefore the limitation of fixed reliability-based guidance in path-following phase unwrapping. In such methods, an inaccurate quality map can produce a poor traversal order, causing unreliable pixels to be unwrapped too early and allowing local errors to propagate across larger regions of the interferogram. As a result, the final unwrapped phase may contain discontinuities, inconsistencies, or distorted structures, even when the underlying unwrapping algorithm is correctly implemented.

To overcome this limitation, this chapter presents an optimization-guided phase unwrapping framework based on the Multi-Verse Optimizer (MVO). The proposed method parameterizes a phase quality map using a set of tunable coefficients and employs MVO to optimize these parameters according to an objective function that penalizes discontinuities in the final unwrapped phase. The optimized quality map is then integrated into a Guided Flood Fill unwrapping strategy, resulting in a path-following method guided by an adaptively refined reliability structure rather than a fixed handcrafted descriptor.

4.2 Motivation

The central motivation of this work is that the quality-guidance mechanism itself should not be regarded as a fixed component but as an adaptive element that can be optimized [13, 21]. This method is needed because the reliability structure of an interferogram is not always captured adequately by a single handcrafted descriptor. Different interferograms may exhibit different noise levels, fringe densities, residue distributions, and spatial discontinuities; therefore, a fixed quality measure may not be sufficiently flexible to guide the unwrapping process reliably in all cases. By optimizing the quality-guidance parameters, it becomes possible to search for a more suitable phase-priority structure, one that is better aligned with the continuity and stability requirements of the unwrapping process.

The contribution developed in this chapter therefore does not replace quality-guided unwrapping; rather, it enhances it by improving the mechanism through which unwrapping priorities are established. This makes the approach particularly relevant for interferograms where classical reliability maps are not sufficiently discriminative. By combining the interpretability of path-following phase unwrapping with the adaptability of metaheuristic optimization, the proposed framework aims to reduce error propagation and improve the coherence of the reconstructed phase surface.

4.3 Problem Formulation

Let the input interferogram be denoted by a complex-valued image composed of an amplitude component and a wrapped phase component. The goal of phase unwrapping is to reconstruct a continuous phase field from the wrapped phase while minimizing the occurrence and propagation of unwrapping errors. In path-following approaches, the order in which pixels are unwrapped is a crucial factor, since a poor traversal order may propagate local inconsistencies over large spatial regions.

In classical quality-guided strategies, a reliability map is computed first and then used to prioritize the traversal sequence. The implicit assumption is that pixels with high reliability should be unwrapped before those with lower reliability. Although this principle is intuitive, its effectiveness depends entirely on the validity of the reliability map. If the map is poorly adapted to the actual interferogram, the resulting traversal order becomes suboptimal.

The core idea of the proposed formulation is therefore to parameterize the quality map rather than fixing it in advance. Let the quality map be generated from a family of local phase descriptors controlled by a finite parameter vector. The task is then to determine the parameter vector that leads to the most stable unwrapping behavior according to a chosen continuity-based criterion.

This converts the construction of the quality map into an optimization problem. Instead of searching directly for the final phase field, the method searches for the set of guidance parameters that enables a downstream unwrapping algorithm to produce the most coherent reconstruction. This indirect strategy has an important advantage: it preserves the interpretability and spatial logic of path-following unwrapping while improving its adaptability through optimization.

4.4 Foundations of the Multi-Verse Optimizer

The Multi-Verse Optimizer is a population-based metaheuristic inspired by cosmological concepts related to multiple interacting universes [21]. In this framework, each candidate solution is represented as a universe, and the quality of that solution is quantified by an inflation rate. Better universes correspond to better candidate solutions with respect to the optimization objective.

The search dynamics of MVO rely on three main mechanisms. The first mechanism is the exchange of solution components through analogies to white holes and black holes. Universes with stronger inflation rates are more likely to share their characteristics, whereas universes with weaker inflation rates are more likely to absorb useful information from better candidates. The second mechanism is based on wormholes, which allow universes to move stochastically toward the best solution found so far. This facilitates local refinement in promising regions of the search space.

A key strength of MVO lies in the balance it creates between global exploration and local exploitation. In the early stages of optimization, population diversity is maintained so that broad regions of the search space can be explored. As the search proceeds, the algorithm gradually increases the intensity of local refinement around promising candidates. This behavior makes MVO particularly suitable for nonconvex optimization problems where the objective surface may contain multiple local minima.

In the context of this chapter, MVO is not applied to the final unwrapped phase directly. Instead, it is used to optimize the parameters of the phase quality map. This is a more structured and tractable use of metaheuristic optimization, because the search space is defined over a small and interpretable parameter vector, while the quality of each candidate is evaluated indirectly through the performance of the unwrapping process guided by the resulting map.

which is employed in this study to search for suitable parameter configurations in the phase unwrapping process. The flowchart in Figure 4.1 summarizes the main steps of the algorithm, from the initialization of candidate solutions to the iterative refinement of the search space until the termination criterion is satisfied.

The algorithm starts by generating an initial population of universes, each corresponding to a possible candidate solution. Their fitness values are then computed and used to rank the universes according to their performance. Through the mechanisms of white hole, black hole, and movement toward the best universe, the algorithm balances exploration and exploitation in the search space. This iterative procedure is repeated until the stopping criterion is reached, at which point the best-performing universe is selected as the optimal solution.

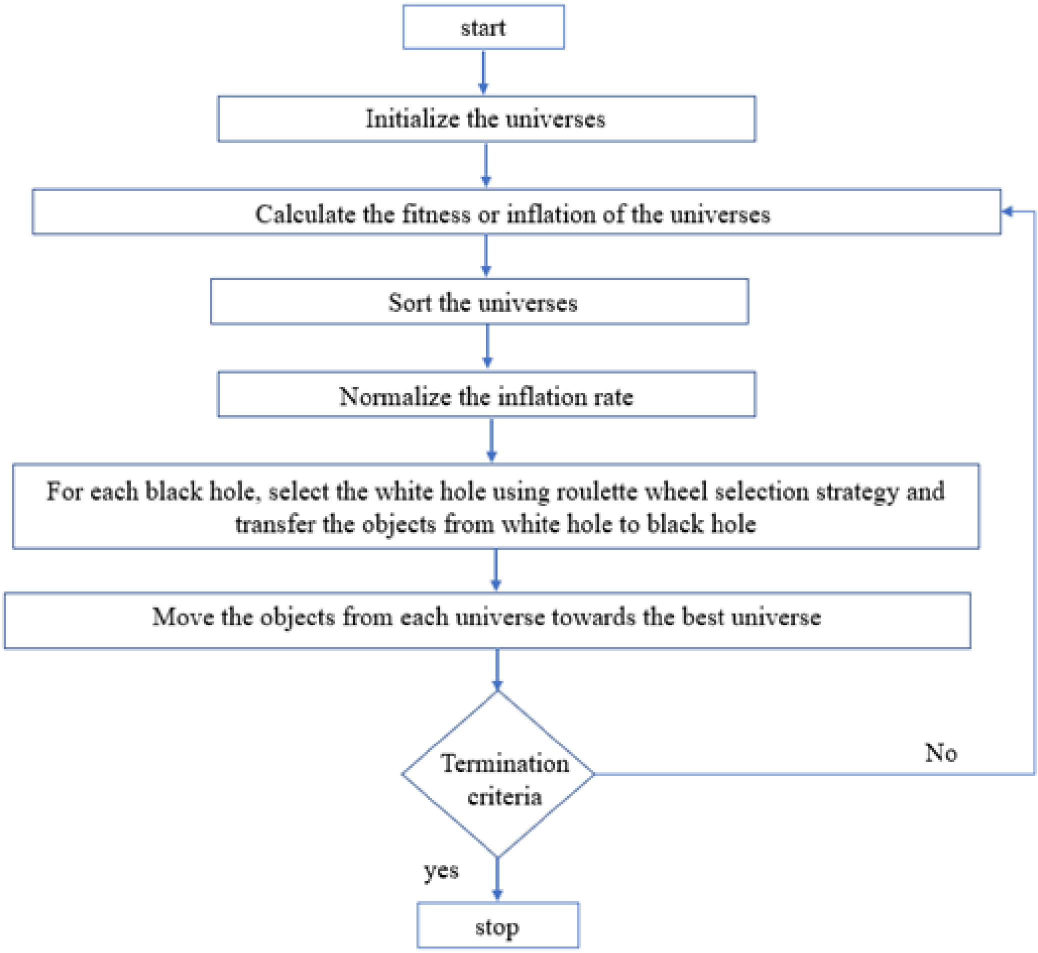

Figure 4.1: Workflow of the Multi-Verse Optimizer (MVO).

4.5 Proposed Optimization-Guided Framework

To address the persistent challenges of phase unwrapping in noisy or decorrelated interferometric data, this study introduces an optimization-guided framework that enhances unwrapping reliability through an adaptively tuned phase quality map [129]. At the core of this framework lies the integration of a parameterized Phase Derivative Variance (PDV) map within a Guided Flood Fill (GFF) unwrapping algorithm. The PDV map incorporates five tunable parameters, which are optimized using the Multi-Verse Optimizer (MVO) to minimize a cost function penalizing both the number and cumulative length of discontinuities in the final unwrapped phase. The overall system design is illustrated schematically in Figure 4.2 below

The proposed framework combines three major components: interferogram preprocessing, parameterized construction of the phase quality map, and phase unwrapping

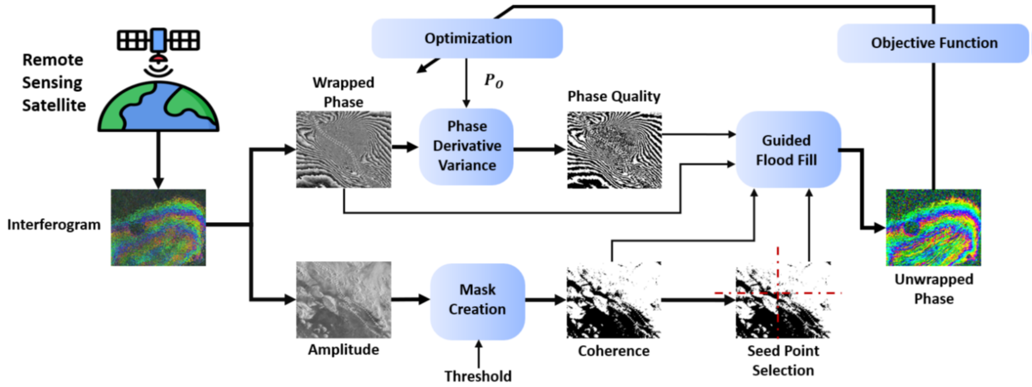

Figure 4.2: Overall architecture of the optimization-guided phase unwrapping framework.

through Guided Flood Fill. These components are integrated into an optimization loop controlled by MVO.

4.5.1 Interferogram Preprocessing

The framework begins with the interferogram as input modeled as

$$I(x, y) = A(x, y)e^{j\phi(x,y)} \tag{4.1}$$

where $A(x, y)$ represents the amplitude image and $\phi(x, y)$ denotes the wrapped phase component. This interferogram is separated into amplitude and wrapped phase components. The wrapped phase is the signal to be unwrapped, while the amplitude information is used to identify reliable image regions and to support initialization.

Because low-intensity regions often correspond to low signal quality or unstable scattering behavior, a masking stage is introduced before unwrapping. This stage excludes pixels considered too unreliable for phase reconstruction. By restricting the processing domain, the method reduces the influence of highly uncertain areas and improves the stability of the subsequent path-following stage.

4.5.2 Mask Construction

A binary mask $M(x, y)$ is generated from the amplitude image by thresholding relative to the maximum amplitude level. Pixels whose amplitude falls below the selected threshold are excluded from the valid processing domain, while the remaining pixels are retained for unwrapping.

$$M(x,y) = \begin{cases} 1, & A(x,y) \geq \tau \cdot \max(A), \\ 0, & \text{otherwise} \end{cases} \tag{4.2}$$

where τ is a threshold factor typically set to 0.3. This ensures that unwrapping operations are restricted to coherent, high-confidence regions of the interferogram.

The purpose of this mask is not simply to reduce image size, but to control the operational domain of the unwrapping process. In noisy interferograms, unwrapping across extremely weak or incoherent regions may introduce severe instability. The mask therefore acts as a confidence filter that constrains the propagation of the phase reconstruction to more trustworthy locations.

4.5.3 Parameterized Quality Map via Phase Derivative Variance

To guide phase integration, the proposed method constructs a quality map $Q(x,y)$ based on a parameterized formulation of Phase Derivative Variance.

$$Q(x,y) = C\left(\left|\frac{\partial\phi}{\partial x}\right|^{H} + \left|\frac{\partial\phi}{\partial y}\right|^{B}\right) + D\nabla^2\phi(x,y) + G\sigma^2_{\text{local}}(\phi) \tag{4.3}$$

The quality map $Q(x,y)$ assigns a reliability value to each valid pixel of the interferogram. In phase unwrapping, this value is used to determine the order in which pixels are processed: pixels with higher reliability are unwrapped earlier, while pixels with lower reliability are delayed. The parameters (C, H, B, D, G) control the relative influence of local phase-derivative information, including horizontal and vertical variations, higher-order phase changes, and local variability. Regions with smooth and stable derivatives usually indicate coherent phase behavior and are therefore assigned higher quality values. In contrast, regions with large derivative fluctuations are more likely to contain noise, residues, discontinuities, or decorrelation effects, and are assigned lower priority. Optimizing these parameters allows the quality map to adapt to the specific structure of each interferogram instead of relying on a fixed handcrafted reliability measure.

The rationale behind this choice is that local variations in the phase derivatives contain useful information about structural regularity and about the likelihood that a pixel belongs to a stable region of the interferogram [47].

Rather than computing a fixed PDV map from a rigid formula, the proposed framework defines a family of quality maps controlled by a small set of coefficients. These coefficients regulate the relative importance of directional derivatives, higher-order phase behavior, and local variability. In this way, the quality map becomes an adaptive object whose characteristics can be tuned to better match the interferogram under consideration.

This design is important because there is no guarantee that a single predefined quality measure is optimal across all interferograms. By allowing the phase-quality representation to vary, the method opens the possibility of discovering reliability patterns more compatible with the actual data structure and with the behavior of the unwrapping algorithm.

4.5.4 Seed Point Selection

The Guided Flood Fill algorithm requires an initial seed from which the unwrapping process begins. In the proposed framework, the seed point is selected as the valid pixel with the highest amplitude value. The rationale is that high-amplitude pixels are more likely to correspond to coherent and stable scattering areas, making them suitable starting points for phase propagation.

$$(x_0, y_0) = \arg\max_{(x,y)\in M} A(x, y) \tag{IV.14}$$

This initialization strategy reduces the probability that the unwrapping process begins in a noisy or structurally ambiguous location. Since errors introduced early in the path-following process can propagate outward, the stability of the seed point plays an important role in the overall quality of the reconstruction.

4.5.5 Guided Flood Fill Phase Unwrapping

Once the seed point and quality map have been defined, unwrapping proceeds through a Guided Flood Fill (GFF) strategy. The algorithm expands from the seed point to neighboring pixels according to spatial connectivity, while the priority of candidate neighbors is determined by the optimized quality map. The unwrapped phase at neighboring pixel (x', y') is computed as

$$\Phi(x', y') = \Phi(x, y) + \Delta\phi \tag{4.4}$$

where

$$\Delta\phi = W[\phi(x', y') - \phi(x, y)] \tag{4.5}$$

$W[\cdot]$ wraps the phase difference into $(-\pi, \pi]$

This equation describes how the unwrapped phase is propagated from an already unwrapped pixel (x, y) to a neighboring pixel (x', y'). The value $\Phi(x, y)$ represents the known unwrapped phase at the current pixel, while $\Phi(x', y')$ is the phase value to be estimated. The term $\Delta\phi$ is the locally corrected phase difference between the two neighboring wrapped phase values. Because wrapped phases are limited to $(-\pi, \pi]$, the raw difference $\phi(x', y') - \phi(x, y)$ may contain artificial 2π jumps. The wrapping operator $W[\cdot]$ removes these artificial jumps by selecting the equivalent phase difference that is closest to zero. In this way, the algorithm assumes that neighboring reliable pixels should vary smoothly and uses this local continuity assumption to reconstruct the continuous phase surface progressively.

The essential characteristic of the proposed framework is that the order of propagation is no longer based on a fixed handcrafted reliability map. Instead, it is governed by an optimized map whose parameters have been selected to favor continuity in the final output. This transforms Guided Flood Fill from a standard path-following routine into an optimization-guided reconstruction process.

4.6 Objective Function Design

The quality of a candidate parameter vector must be assessed indirectly through the phase map produced after unwrapping. For this reason, the objective function used by the MVO is not defined on the quality map itself, but on measurable properties of the resulting unwrapped phase.

The main criterion adopted in this chapter is the presence of discontinuities in the reconstructed phase field. A robust unwrapping solution is expected to preserve meaningful phase structure while minimizing spurious abrupt transitions caused by reconstruction errors. Accordingly, the proposed objective function is built from two complementary terms: the number of discontinuity pixels (ND) and the total spatial extent of discontinuity clusters (LD).

To detect discontinuities, the spatial gradient of the unwrapped phase is examined. Locations where the local gradient magnitude exceeds a threshold are interpreted as discontinuity points. This threshold is defined adaptively with respect to gradient statistics so that natural phase slopes are less likely to be confused with unwrapping artifacts.

The first term of the objective is the count of all pixels identified as discontinuity points. This quantity measures how frequently strong phase inconsistencies occur in the unwrapped map. The second term measures the total length or extent of connected discontinuity components, thereby reflecting not only the presence of isolated artifacts but also the spatial spread of irregular regions. These two terms are combined into a weighted objective function formulated as

$$J(\Theta) = \alpha ND + \beta LD \tag{4.6}$$

The objective function $J(\Theta)$ evaluates the quality of a candidate parameter vector $\Theta = (C, H, B, D, G)$. The term ND counts the number of detected discontinuity pixels in the unwrapped phase, while LD measures the total spatial extent of connected discontinuity regions. The coefficients α and β control the relative importance of these two penalties. Minimizing $J(\Theta)$ means searching for a quality-map parameter set that produces an unwrapped phase with fewer abrupt jumps and fewer extended error regions. In the context of phase unwrapping, this is meaningful because true unwrapped phase surfaces are expected to be spatially coherent, whereas unwrapping errors usually appear as sharp discontinuities or irregular phase breaks. Therefore, the objective function links the MVO search directly to the physical and structural quality of the reconstructed phase field.

Table 4.1 summarizes the main components of the objective function adopted in this study, together with their definitions and physical interpretations. The table is intended to clarify the role of each term involved in the evaluation of candidate parameter vectors and to show how the objective function reflects the structural properties of the unwrapped phase map.

Table 4.1: Components of the objective function and their physical interpretation.

Term	Definition	Interpretation
ND	Number of discontinuity pixels	Counts how often strong phase inconsistencies occur
LD	Total extent of connected discontinuity components	Measures spatial spread of irregular regions
α	Weight of ND	Controls penalty on discontinuity frequency
β	Weight of LD	Controls penalty on discontinuity extent
$J(\Theta)$	$\alpha ND + \beta LD$	Overall objective minimized by MVO

The optimization process then seeks the parameter vector that minimizes this objective, meaning that it prefers quality maps leading to smoother, more coherent, and less fragmented phase reconstructions. This objective is particularly appropriate for the present work because it evaluates what ultimately matters in path-following unwrapping: the structural stability of the reconstructed phase surface.

4.7 Optimization Workflow

The complete workflow of the proposed method can be summarized as an iterative interaction between the MVO and the Guided Flood Fill unwrapping procedure. First, an initial population of universes is created, where each universe corresponds to one candidate parameter vector for the quality map. For each universe, the corresponding PDV-based quality map is computed, the Guided Flood Fill algorithm is executed, and the resulting unwrapped phase is evaluated using the discontinuity-based objective function.

Based on these evaluations, the MVO updates the candidate universes through white-hole and black-hole exchanges and through wormhole-based refinement toward the best current solution. This process is repeated until a stopping criterion is reached, such as a maximum number of iterations or convergence in objective value.

The final output of the optimization stage is the best parameter vector identified by the MVO. This vector defines the optimized quality map used by the unwrapping algorithm. The resulting phase reconstruction constitutes the final output of the proposed framework.

The structure of this workflow has an important methodological implication. The optimization does not attempt to reconstruct the phase directly in one global step. Instead, it improves the conditions under which a classical path-following method operates. This preserves the intuitive spatial logic of Guided Flood Fill while introducing a higher degree of adaptability through parameter optimization.

The table below summarizes the complete workflow of the proposed MVO-guided phase unwrapping framework.

Table 4.2: Workflow of the proposed MVO-guided phase unwrapping framework.

Step	Operation
1	Initialize a population of universes representing candidate PDV parameter vectors Θ.
2	For each universe, compute the quality map $Q(x, y)$, unwrap the interferogram with guided flood fill, and evaluate $J(\Theta)$.
3	Rank universes according to inflation rate derived from the objective function.
4	Update universes using white-hole / black-hole exchange and wormhole refinement around the best solution.
5	Repeat until convergence or maximum iteration, then retain the best Θ and corresponding unwrapped phase.

the principal implementation settings and hyperparameter values adopted in the proposed method. These parameters govern the preprocessing stage, the search dynamics of the Multi-Verse Optimizer, and the propagation behavior of the guided flood-fill unwrapping procedure. In particular, the amplitude threshold is used to suppress unreliable low-backscatter regions, while the population size and iteration limit regulate the trade-off between exploration capability and computational burden. The neighborhood definition influences the local connectivity structure of the unwrapping process, and the stopping criterion ensures that the optimization terminates once convergence is reached or further evaluation becomes unnecessary.

4.8 Computational and Methodological Discussion

From a methodological perspective, the proposed framework occupies an intermediate position between classical path-following methods and fully global optimization of the phase field. On one hand, it retains the interpretable structure of quality-guided unwrapping: phase reconstruction still proceeds through spatial propagation from reliable regions. On the other hand, it introduces a layer of adaptive optimization that allows the guidance mechanism itself to be refined according to the continuity properties of the final output.

This design offers several advantages. First, the optimized parameter space remains relatively compact and interpretable. Second, the objective function is directly linked to phase continuity, which gives the optimization process a clear structural meaning. Third, the framework does not require labeled training data, which is particularly relevant in interferometric applications where ground-truth unwrapped phase is often unavailable.

However, the method also has limitations. Since each candidate universe must be evaluated through an actual unwrapping procedure, the overall optimization may become computationally expensive, especially for large interferograms or high iteration counts. Furthermore, the quality of the final solution depends on the chosen parameterization of the PDV map and on the design of the discontinuity-based objective function. If these elements are too restrictive, the search space may not include sufficiently expressive guidance patterns.

These limitations indicate that adaptive optimization can substantially enhance classical quality-guided unwrapping, but it does not eliminate the dependence on hand-crafted representations altogether. This observation motivates the next step of the thesis: the development of a learning-based approach in which phase continuity is modeled directly from data rather than indirectly through a designed quality map.

4.9 Conclusion

This chapter introduced the first methodological contribution of the thesis: an optimization-guided phase unwrapping framework based on the Multi-Verse Optimizer. The proposed method starts from the observation that classical quality-guided unwrapping is strongly limited by the reliability map used to determine the propagation order. To address this issue, the chapter reformulated the construction of the quality map as an optimization problem and employed MVO to search for parameters that minimize discontinuities in the final unwrapped phase.

By combining parameterized Phase Derivative Variance, amplitude-based masking, seed-point selection, and Guided Flood Fill unwrapping within an optimization loop, the proposed framework enhances the adaptability of classical path-following reconstruction while preserving its interpretability. The resulting method constitutes a robust alternative to fixed quality-guided strategies, particularly in interferograms characterized by noise and low-coherence.

At the same time, the chapter showed that even an optimized quality-guided approach remains based on handcrafted phase descriptors and iterative search. This remaining limitation motivates the second major contribution of the thesis, developed in the next chapter, which explores the possibility of learning phase continuity directly from data through a dedicated hybrid deep architecture.

Chapter 5

Vision-Optimized Hybrid Network for Deep Learning-Based Phase Unwrapping

5.1 Introduction and Motivation

The optimization-guided framework developed in the previous chapter improves phase unwrapping by adaptively refining the reliability structure that governs the traversal order of a classical path-following algorithm. This represents an important step beyond fixed handcrafted quality-guided methods. However, the approach still relies on manually designed phase descriptors and on an iterative optimization process that searches over a predefined parameter space. Although this strategy enhances adaptability, it remains indirect: the model does not learn phase continuity itself, but rather optimizes the conditions under which a classical algorithm operates.

The problem addressed in this chapter is the accurate reconstruction of a continuous phase surface from a wrapped phase image. In wrapped phase data, the measured phase is restricted to a principal interval, commonly $(-\pi, \pi]$, which introduces artificial 2π discontinuities known as phase wraps. The objective of phase unwrapping is therefore to remove these discontinuities and recover the underlying continuous phase distribution.

This problem becomes particularly challenging when the wrapped phase contains noise, dense fringes, residues, or spatially complex discontinuities. Under such conditions, classical phase unwrapping methods that depend on handcrafted quality maps, predefined reliability measures, or path-following rules may fail to fully capture the true continuity structure of the phase surface. As a result, local unwrapping errors can propagate and produce globally inconsistent reconstructions.

This observation motivates a second methodological direction [20, 22]. Instead of designing and tuning a quality map manually, it becomes natural to ask whether a model can learn the spatial structure of phase continuity directly from data. If such a model can identify how wrapped phase patterns correspond to continuous phase surfaces, then phase unwrapping may be formulated as a data-driven image reconstruction problem rather than as a handcrafted traversal problem [70, 71].

Deep learning provides a suitable framework for this objective because it allows complex nonlinear mappings to be learned from examples [22, 71]. In the context of phase unwrapping, however, a standard image-to-image architecture is not sufficient on its own. The task requires not only local feature extraction, but also the preservation of long-range spatial consistency across the interferogram. A locally accurate prediction may still produce a globally inconsistent phase surface if the model fails to capture extended dependencies [66].

For this reason, this chapter introduces VOH-Net, a Vision-Optimized Hybrid Network designed specifically for phase unwrapping. The model combines convolutional encoding and decoding with an enhanced multidirectional Long Short-Term Memory mechanism in order to integrate local spatial features with broader contextual continuity. The aim of the chapter is to present the rationale, construction, and training of this architecture as the second principal contribution of the thesis.

5.2 Learning Formulation of Phase Unwrapping

In a learning-based perspective, phase unwrapping can be viewed as a supervised mapping from a wrapped phase image to its corresponding continuous phase representation. Under this formulation, the input to the model is the wrapped phase map and the desired output is the unwrapped phase field. The role of the neural network is therefore to approximate the transformation that resolves cyclic ambiguity while preserving the underlying spatial structure of the phase.

This formulation differs conceptually from classical methods. In path-following or optimization-guided approaches, the problem is usually solved through explicit local correction, residue management, or minimization of a predefined objective. In contrast, a neural model attempts to learn the relationship implicitly from examples. This makes it possible to capture nonlinear behaviors and structural patterns that may be difficult to express analytically.

However, learning-based phase unwrapping also introduces specific challenges. The first is that the network must distinguish between wrapped discontinuities caused by modulo effects and true structural variations corresponding to the underlying phase surface. The second is that phase continuity is not purely local. A reliable reconstruction may depend on contextual information distributed over large image regions, especially in the presence of noise or repeated patterns.

These challenges motivate a hybrid architecture. Convolutional layers are well suited for extracting local features and suppressing high-frequency disturbances, while recurrent mechanisms can propagate information over longer spatial extents [74, 75]. The learning formulation adopted in this chapter is therefore based on the idea that successful unwrapping requires both multiscale local representation and multidirectional long-range dependency modeling [76].

5.3 Dataset Design and Generation

The performance of a learning-based phase unwrapping model depends strongly on the quality and diversity of the data used for training and evaluation. Since large collections of real interferograms paired with reliable ground-truth unwrapped phases are difficult to obtain, the proposed framework relies on synthetic data generation for supervised learning, while still incorporating real interferometric data during the evaluation stage.

5.3.1 Synthetic Unwrapped Phase Generation

To construct training samples, synthetic continuous phase maps are generated using combinations of Gaussian components with varying amplitudes, polarities, and spatial positions. This design produces diverse phase surfaces containing peaks, depressions, and irregular transitions rather than only simple idealized structures. In addition to these Gaussian patterns, random linear ramps are introduced along horizontal and vertical directions in order to simulate broader phase trends.

The purpose of this generation strategy is to expose the network to a wide range of spatial configurations [22, 71]. By varying local structures and large-scale gradients simultaneously, the synthetic dataset approximates the diversity of phase surfaces that may appear in realistic interferometric scenarios. This improves the ability of the model to learn phase continuity beyond a narrow class of patterns.

5.3.2 Wrapped Phase Formation

Once the synthetic continuous phase map is created, the corresponding wrapped phase is obtained through the standard phase wrapping operation, which maps the continuous phase to the principal interval. This produces the input representation seen by the network during training, while the original continuous phase serves as the target output.

This pairing defines a supervised learning problem in which the model must learn to recover the original phase structure from its cyclically wrapped representation. Because the generation process is controlled, the exact relationship between input and target remains known for every sample.

Let $\phi(x, y)$ denote the true unwrapped phase at the pixel coordinates (x, y). The corresponding wrapped phase $\psi(x, y)$ is obtained through the standard wrapping operation:

$$\psi(x, y) = \angle \left(e^{j\phi(x,y)}\right) \tag{5.1}$$

where j represents the imaginary unit, and $\angle(\cdot)$ extracts the phase angle (argument) of a complex number, mapping it to the principal interval $(-\pi, \pi)$. The core challenge of phase unwrapping lies in reconstructing $\phi(x, y)$ from the observed $\psi(x, y)$, particularly under conditions of noise, discontinuities, and aliasing.

5.3.3 Training Datasets

To simulate realistic yet controlled learning conditions, synthetic unwrapped phase images $\phi(x, y)$ were generated by combining multiple Gaussian functions of varying amplitudes, spatial positions, and polarities (positive or negative). Random linear phase ramps were then added along both horizontal and vertical directions to simulate large-scale phase trends. This composition yields non-uniform and topologically diverse phase fields, enabling the network to generalize across various deformation patterns. Two datasets were produced, each comprising 1,500 images of size 256×256, with phase values uniformly distributed in the range $[-44, 44]$. One dataset remained noise-free, while the other was corrupted with additive Gaussian noise at randomly selected signal-to-noise ratios (SNRs) $\{0, 5, 10, 20, 60\}$ dB prior to the wrapping operation, effectively emulating realistic interferometric noise conditions.

5.3.4 Independent Testing Datasets

For evaluation, an independent generation strategy was adopted to prevent overlap with the training data and to rigorously assess model generalization. Small random matrices (ranging from 2×2 to 25×25) were first constructed with values drawn from either a uniform or Gaussian distribution within the range [2, 77]. These matrices were subsequently upsampled to 256×256 using one of three interpolation methods: nearest-neighbor, bilinear, or bicubic. The wrapped phase was then computed using Equation (5.1), ensuring methodological consistency with the training process. To mimic real-world acquisition conditions, additional noise types, Gaussian, salt-and-pepper, and multiplicative, were introduced at random intensities into $\psi(x, y)$. This unified dataset formulation guarantees that both training and testing data adhere to the same underlying physical phase model while maintaining sufficient variability to challenge the network's ability to generalize to unseen patterns. Although Gaussian noise is the predominant error component in interferometric measurements, real-world InSAR data can also exhibit non-Gaussian perturbations such as decorrelation-induced outliers or phase cycle slips. Accordingly, Gaussian noise was primarily employed during training to model stochastic measurement errors, while additional non-Gaussian disturbances were selectively applied during testing to evaluate robustness under distributional shift. This deliberate mismatch between training and inference noise distributions reflects realistic operational conditions in InSAR applications, ensuring that VOH-Net is exposed to the full spectrum of practical phase unwrapping challenges.

5.3.5 Real Interferometric Data

Although synthetic data are essential for supervised training, practical relevance requires validation on real interferometric observations. For this reason, the final evaluation stage of the thesis includes real wrapped phase data so that the proposed model can be examined under authentic interferometric conditions.

The role of these real data is not necessarily to provide perfect ground truth for every pixel, which may be unavailable, but to assess whether the reconstructed phase maps exhibit improved structural consistency, reduced artifacts, and visually plausible continuity compared with baseline methods. In this way, the thesis combines the control of synthetic supervision with the realism of operational interferometric testing.

5.4 Vision-Optimized Hybrid Network (VOH-Net) Architecture

The Vision-Optimized Hybrid Network (VOH-Net) is designed as a hybrid encoder-decoder neural network specialized for phase unwrapping [77]. The architecture combines hierarchical convolutional feature extraction with a central recurrent module that captures long-range spatial dependencies along multiple directions. This section presents the main architectural components and the rationale behind each of them. Figure 5.7 illustrates the overall architecture of the Vision-Optimized Hybrid Network (VOH-Net) proposed for phase unwrapping. The model is designed as a hybrid encoder-decoder framework that combines convolutional feature extraction with a central recurrent module in order to capture both local spatial patterns and long-range contextual dependencies within the interferometric phase data.

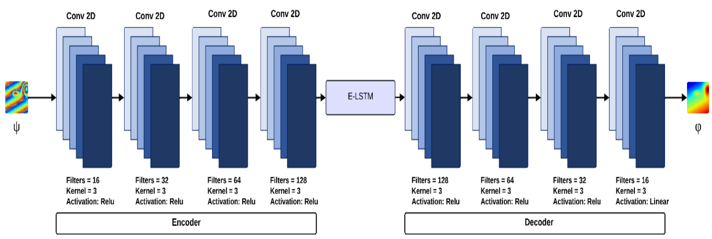

Figure 5.1: Overall architecture of VOH-Net.

5.4.1 Overall Architectural Principle

At a high level, VOH-Net follows a symmetric encoder-decoder structure. The encoder transforms the wrapped phase input into a compact multiscale feature representation, while the decoder reconstructs the continuous phase map from this latent representation. Between these two stages, an enhanced recurrent module processes the encoded features in multiple spatial directions, thereby allowing the model to incorporate broader contextual information before reconstruction.

The importance of this design lies in the complementarity of its components. The encoder and decoder provide local and multiscale image-processing capability, while the recurrent bottleneck is responsible for integrating spatial continuity beyond the short receptive fields of standard convolutional layers.

5.4.2 Encoder Network

The encoder is composed of successive convolutional blocks interleaved with downsampling operations. Each block extracts progressively more abstract features from the wrapped phase input, allowing the network to detect local structures, gradients, textures, and phase patterns at multiple spatial scales.

Through repeated convolution and pooling, the encoder reduces the spatial dimension of the representation while increasing its feature depth. This compression has two advantages. First, it enables the model to summarize local phase behavior efficiently. Second, it prepares a latent representation suitable for recurrent processing, since long-range spatial relations can be modeled more effectively at reduced spatial resolution than at the full image size.

The encoder therefore serves as the local feature-analysis component of VOH-Net. It does not resolve the unwrapping task by itself, but transforms the input into a representation from which longer-range continuity relationships can be learned more effectively.

For mathematical clarity, the encoder component of VOH-Net is designed to progressively extract hierarchical spatial features from the input wrapped phase map. The input, denoted as $\psi \in \mathbb{R}^{256\times256\times1}$, corresponds to the wrapped interferometric phase image. Each convolutional block in the encoder performs a sequence of operations: two-dimensional convolution, batch normalization, ReLU activation, and average pooling. These operations enable the network to capture increasingly abstract representations of the input data while reducing spatial dimensions. Mathematically, for the k-th convolutional block ($k = 1, 2, 3, 4$), the convolutional transformation is defined as

$$C_k = \sigma\left(BN\left(W_k * P_{k-1} + b_k\right)\right) \tag{5.2}$$

where P_{k-1} is the output of the previous block (with $P_0 = \psi$), and W_k and b_k represent the learnable weights and biases of the convolutional layer, respectively. Following convolution and normalization, average pooling is applied to reduce spatial resolution by a factor of two:

$$P_k = \mathrm{AvgPool}(C_k) \tag{5.3}$$

The final output of the encoder, $P_4 \in \mathbb{R}^{16\times16\times128}$, serves as the compact feature representation of the input interferogram, preserving essential phase-related structures for subsequent processing.

5.4.3 Enhanced Multidirectional LSTM Module

The central element of VOH-Net is the E-LSTM module [20, 71]. The motivation for this component is that phase continuity is not strictly determined by short-range neighborhoods. In many interferograms, the interpretation of local wrapped structures depends on larger contextual patterns extending horizontally, vertically, and diagonally across the image.

To capture this contextual structure, the encoded feature map is reshaped and processed along several spatial directions. Specifically, horizontal, vertical, diagonal, and anti-diagonal traversals are considered. Each traversal is handled by a recurrent processing branch that learns how information should propagate along that orientation.

This multidirectional design is important because phase patterns are not aligned uniformly in a single direction. A model limited to row-wise or column-wise context may fail when the dominant continuity structure follows oblique trajectories or when long-range interactions occur along multiple orientations simultaneously. By combining directional branches, the module constructs a richer representation of the spatial organization of the phase field.

After directional processing, the resulting features are reshaped back into spatial form and concatenated. This fusion step integrates the contextual information captured from all orientations and produces a latent representation that contains both local detail inherited from the encoder and long-range continuity information learned through recurrent modeling.

The Enhanced Long Short-Term Memory (E-LSTM) module is illustrated in Figure 5.2.

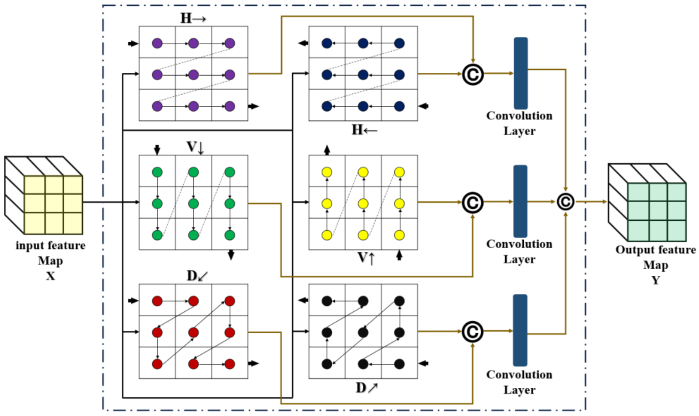

Figure 5.2: E-LSTM module illustrating multidirectional feature extraction for enhanced spatial dependency modeling.

Step 1: Reshaping for Sequence Processing. The encoded feature map P_4 is first reshaped into directional sequences suitable for recurrent processing. For horizontal and vertical directions, the transformations are expressed as

$$X_{\text{hor}} = \text{reshape}(P_4), \quad X_{\text{ver}} = \text{reshape}(P_4^T) \tag{5.4}$$

A similar reshaping procedure is performed for diagonal and anti-diagonal sequences, ensuring that features from all spatial orientations are appropriately aligned for LSTM-based sequence modeling.

Step 2: Directional Processing. Each sequence is then processed through an E-LSTM unit [75, 82] to capture long-range dependencies within that direction. The operation is mathematically expressed as

$$H_{\text{dir}} = \text{LSTM}_{\text{dir}}(X_{\text{dir}}; W_{\text{lstm}}, b_{\text{lstm}}) \tag{5.5}$$

where X_{dir} denotes the reshaped input for a specific direction, and W_{lstm} and b_{lstm} are the trainable parameters of the LSTM layer.

Step 3: Reconstruction and Concatenation. Following the directional LSTM processing, each output is reshaped back to its spatial dimensions. The resulting feature maps from the horizontal, vertical, diagonal, and anti-diagonal directions, denoted as $H'_{\text{hor}}, H'_{\text{ver}}, H'_{\text{diag}}, H'_{\text{anti-diag}}$, are concatenated to form a unified representation:

$$F = \text{concat}(H'_{\text{hor}}, H'_{\text{ver}}, H'_{\text{diag}}, H'_{\text{anti}}) \tag{5.6}$$

This multidirectional fusion enriches the feature space with both local and global spatial information, enabling the network to better preserve phase continuity and mitigate the impact of noise and decorrelation.

5.4.4 Decoder Network

The decoder reconstructs the continuous phase map from the context-enriched latent representation. It performs progressive upsampling through transposed convolution or equivalent operations, gradually recovering the original spatial dimensions of the input.

At each stage, skip connections are used to merge decoder features with corresponding encoder features. These skip connections are essential because they restore high-resolution spatial information that may have been lost during downsampling. As a result, the decoder can reconstruct fine phase detail without sacrificing the broader context introduced by the recurrent bottleneck.

The decoder therefore serves as the synthesis stage of VOH-Net: it transforms the abstract representation learned by the encoder and recurrent module into a coherent phase surface that approximates the target unwrapped phase. For mathematical clarity, The decoder reconstructs the unwrapped phase map by progressively upsampling the multidirectional feature maps produced by the E-LSTM. The upsampling operation is implemented using transposed convolution layers defined as

$$U_k = \text{TransConv}(H_{k-1}; W_k^T, b_k^T) \tag{5.7}$$

where H_{k-1} denotes the output from the previous decoding stage, and W_k^T and b_k^T represent the learnable weights and biases of the transposed convolution layer. Each upsampled feature map U_k is concatenated with the corresponding encoder feature map C_{9-k} through skip connections, allowing high-resolution spatial information to be reintroduced:

$$U_k' = \text{Concatenate}(U_k, C_{9-k}) \tag{5.8}$$

A subsequent convolutional operation refines the concatenated features to produce the output of the k-th decoding block:

$$H_k = \sigma\left(W_k * V_k + b_k\right) \tag{5.9}$$

This iterative decoding process ensures that both global context and fine-grained phase details are preserved throughout the reconstruction pathway.

5.4.5 Output Layer

The final layer of the network converts the refined decoder representation into a single-channel continuous phase estimate. This output is interpreted as the predicted unwrapped phase map corresponding to the wrapped phase input.This operation is expressed as

$$\hat{\phi} = W_o * H_{\text{final}} + b_o \tag{5.10}$$

The resulting output ϕ represents the reconstructed phase field, where noise and discontinuities have been effectively suppressed through the hierarchical feature extraction, directional dependency modeling, and structured decoding mechanisms of the proposed VOH-Net. Unlike a classification-based formulation that would discretize ambiguity classes, the output layer is designed for continuous regression. This choice is consistent with the objective of recovering a smooth and physically interpretable phase surface rather than merely assigning local wrap counts.

5.5 Loss Function Design

The choice of loss function is critical in learning-based phase unwrapping because the model must not only minimize pixel-wise error, but also preserve the structural consistency of the reconstructed phase surface [66, 71]. A purely local fidelity objective may produce numerically acceptable predictions while still allowing spatial irregularities or incoherent phase transitions. For this reason, the training objective adopted in this work combines complementary components.

The first component is the Mean Squared Error between the predicted phase and the reference continuous phase. This term encourages pixel-level fidelity and penalizes large deviations in absolute phase value. It ensures that the network remains anchored to the target reconstruction at the local scale.It is expressed as

$$L_{\mathrm{MSE}} = \frac{1}{N}\sum_{i=1}^{N}(\hat{y}_i - y_i)^2 \tag{5.11}$$

where N denotes the total number of pixels, $\hat{y}_i$ represents the predicted phase value produced by the network at pixel i, and y_i corresponds to the reference, or ground-truth, phase value at the same pixel. This loss penalizes the squared difference between the predicted and reference phase values, encouraging the model to generate phase estimates that closely approximate the ground truth across all pixel locations.

The second component is a gradient-based regularization term that penalizes discrepancies between spatial phase variations in the prediction and in the reference. The role of this term is to encourage structural smoothness and to preserve the continuity of the phase surface while avoiding unnecessary oscillations. In the context of this thesis, this term is treated as the structural smoothness component of the loss. It is formulated as

$$L_{\mathrm{grad}} = \frac{1}{N}\sum_{i=1}^{N}\|\nabla\hat{y}_i - \nabla y_i\|_2^2 \tag{5.12}$$

where $\nabla\hat{y}_i$ and ∇y_i denote the spatial gradients of the predicted and reference phase values at pixel i, respectively. This term encourages the network to preserve local phase variations, edges, and structural details by minimizing the difference between the predicted and ground-truth phase gradients.

For the variance loss, write:

$$L_{\text{var}} = \mathrm{Var}(\hat{y} - y) \tag{5.13}$$

or more explicitly:

$$L_{\text{var}} = \frac{1}{N}\sum_{i=1}^{N}(E_i - \bar{E})^2, \quad E_i = \hat{y}_i - y_i \tag{5.14}$$

where E_i denotes the prediction error at pixel i, and $\bar{E}$ represents the mean prediction error over all pixels. By penalizing deviations from the mean error, this term reduces the concentration of large errors in localized regions and encourages more uniform reconstruction accuracy across the interferogram.

The final loss is formed by combining these three components with an appropriate weighting strategy. This design reflects the three requirements of phase unwrapping regression: local accuracy, structural coherence, and stable spatial error behavior. By training the model with this composite objective, the network is encouraged to reconstruct a phase surface that is not only close to the reference numerically, but also coherent in its geometric and spatial organization. The overall training objective integrates these three components into a single weighted function:

$$\text{Loss} = L_{\text{mse}} + \lambda \cdot L_{\text{grad}} + L_{\text{var}} \tag{5.15}$$

The hyperparameter $\lambda = 0.1$ controls the influence of the gradient regularization term. This value was determined empirically through a grid search over $\lambda \in \{0.01, 0.05, 0.1, 0.2\}$, where $\lambda = 0.1$ provided the most balanced trade-off between preserving smooth phase continuity and maintaining high pixel-wise reconstruction accuracy. Higher values of λ tended to oversmooth the phase surface, while smaller values resulted in residual discontinuities.

To evaluate the impact of this composite design, Table 5.6 presents a comparison between the original and modified loss formulations, highlighting their respective components and contributions to overall model performance.

Table 5.1: Comparison between original and modified loss functions.

Aspect	Original Loss Function	Modified Loss Function
Gradient Regularization Loss	Yes	Yes
Variance of Error Loss	Yes	Yes
Mean Squared Error	No	Yes
Final Objective	Smoothness + Error Consistency	Smoothness + Error Consistency + Pixel-wise Accuracy

Table 5.2: Comparison of loss function formulations and their expected effects.

Formulation	Components	Expected effect
Original formulation	Gradient term + variance control	Promotes smoothness but may underweight pointwise error
Modified formulation	MSE + gradient term + variance control	Retains continuity while improving local accuracy

The modified formulation explicitly introduces the Mean Squared Error term, which enhances pixel-level precision without compromising the smoothness and consistency promoted by the original loss components. This combination ensures that VOH-Net not only reconstructs globally consistent phase surfaces but also preserves the fine structural details required for accurate interferometric analysis.

5.6 Training Protocol and Implementation Strategy

The training of VOH-Net follows the standard supervised learning setting established by the synthetic dataset construction described earlier. Wrapped phase images are provided to the network as inputs, while the corresponding continuous phase maps are used as targets. The optimization of the network parameters is performed with a gradient-based learning algorithm, using the composite loss defined in the previous section.

To improve generalization, training is conducted on both clean and noisy synthetic data. Validation data are used to monitor convergence and to reduce the risk of overfitting. This separation between training and validation is important because a network that memorizes the synthetic generation process without learning robust continuity principles would perform poorly on out-of-distribution or real interferometric data.

The implementation strategy also reflects practical considerations related to phase unwrapping. First, the image dimensions and architectural depth are selected to balance representational richness with computational feasibility. Second, recurrent processing is applied at the encoded feature level rather than directly on the full-resolution input, which reduces memory usage while preserving the ability to model long-range dependencies.

In this way, the design of VOH-Net is not only motivated by theoretical considerations about phase continuity, but also by the need for a trainable and computationally manageable architecture suitable for interferometric image reconstruction.

5.7 Conclusion

This chapter introduced the second methodological contribution of the thesis: VOH-Net, a hybrid deep neural architecture for phase unwrapping. The chapter began by motivating the move from optimization-guided path-following toward a learning-based formulation in which the mapping from wrapped to continuous phase is learned directly from data.

To support this formulation, the chapter described a synthetic data-generation strategy designed to expose the model to diverse phase structures and noise conditions, while still allowing evaluation on real interferometric observations. It then presented the architecture of VOH-Net, emphasizing the complementarity between multiscale convolutional processing and enhanced multidirectional LSTM modeling. Finally, it introduced a composite loss function intended to promote pixel-level fidelity, spatial smoothness, and stable error behavior.

Taken together, these elements define VOH-Net as a dedicated phase unwrapping architecture that addresses one of the central limitations of existing learning-based methods: insufficient modeling of long-range spatial continuity. The next chapter evaluates both the optimization-guided framework and VOH-Net under a common experimental setting and compares their behavior in terms of accuracy, robustness, and practical suitability for interferometric phase reconstruction.

Chapter 6

Experimental Evaluation and Comparative Discussion

6.1 Introduction

The previous two chapters presented the methodological contributions of this thesis from two complementary perspectives. Chapter 4 introduced an optimization-guided framework that enhances classical path-following unwrapping through adaptive quality-map optimization, while Chapter 5 presented VOH-Net as a deep learning architecture for direct phase reconstruction. Although each contribution has its own rationale and internal design, the scientific value of the thesis depends on evaluating them under a coherent comparative framework.

The purpose of this chapter is therefore twofold. First, it aims to assess the performance of the proposed methods in terms of phase reconstruction quality, continuity preservation, robustness to degradation, and practical behavior on both synthetic and real interferometric data [19, 32]. Second, it aims to compare the two paradigms directly in order to clarify their respective strengths, limitations, and suitable operating contexts [67, 70].

Both methods are tested on synthetic and real InSAR datasets to assess their accuracy, phase continuity, and robustness in the presence of noise and decorrelation.

Quantitative metrics and qualitative visual analyses are employed to ensure a balanced evaluation, while comparisons with established benchmark algorithms demonstrate the advances achieved by the proposed models in terms of reliability and generalization capability.

6.2 Experimental Design and Evaluation Protocol

A rigorous evaluation of phase unwrapping methods requires a protocol capable of balancing control and realism. On the one hand, synthetic datasets are necessary because they provide exact continuous phase references, making it possible to compute quantitative reconstruction errors directly. On the other hand, real interferometric data are essential to assess whether the methods remain meaningful when confronted with practical measurement conditions that are more difficult to simulate perfectly.

For this reason, the evaluation adopted in this chapter combines synthetic and real data. The synthetic data provide the basis for direct measurement of reconstruction accuracy and for controlled investigation of noise robustness, discontinuity handling, and architectural sensitivity. The real interferometric data provide a practical benchmark for structural plausibility, continuity preservation, and qualitative reconstruction behavior in operational settings.

The proposed methods are compared with representative baselines drawn from the methodological families reviewed in Chapter 3. These include classical path-following or quality-guided methods, conventional optimization-based strategies where applicable, and learning-based architectures serving as references for VOH-Net. The goal is not merely to show isolated numerical improvement, but to determine how the proposed methods relate to the major existing paradigms in phase unwrapping.

The evaluation criteria reflect the multidimensional nature of the problem [13, 20]. Reconstruction error measures are used to quantify fidelity to the reference phase where ground truth is available. Structural continuity indicators are used to assess the presence of discontinuities or artifacts in the unwrapped output [21]. Additional analysis is devoted to robustness under different degradation conditions and to the qualitative coherence of the reconstructed phase surfaces.

6.3 Optimization-Guided Quality Mapping

The performance of the Optimization-Guided Quality Mapping framework is evaluated to demonstrate its effectiveness in improving phase unwrapping accuracy and reliability. The analysis focuses on how the Multi-Verse Optimizer (MVO) enhances the tuning of the Phase Derivative Variance (PDV) parameters, leading to improved quality map generation and reduced unwrapping errors. Experimental results on synthetic and real interferometric datasets are presented to assess the convergence behavior, optimization stability, and quantitative performance gains compared to conventional path-following and quality-guided unwrapping methods.

6.3.1 Optimization Setup

The Multi-Verse Optimizer (MVO) was employed to minimize the number and cumulative length of phase discontinuities within the interferometric phase data. The optimization process was executed for 100 iterations with a population of 20 universes, representing candidate solutions. Experiments were conducted on an InSAR dataset characterized by significant phase inconsistencies. These settings were selected to ensure an effective balance between exploration and exploitation while maintaining computational feasibility.

6.3.2 Performance Metrics

Table 6.1 summarizes the key configuration parameters and computational performance of the proposed MVO-based phase unwrapping framework. The average processing time per optimization run was approximately 476.34 seconds, which is reasonable given the complexity of the underlying objective function that integrates phase derivative variance and discontinuity-based constraints. The chosen population size of 20 universes provides a suitable trade-off between convergence stability and efficiency for large-scale InSAR applications.

Table 6.2 presents the quantitative results of the MVO optimization in reducing phase discontinuities, expressed in terms of both count and cumulative length. These metrics directly reflect the spatial consistency and smoothness achieved in the reconstructed

Table 6.1: Optimization Configuration and Performance.

Metric	**MVO Iterations**	**Number of Universes**	**Average Processing Time (s)**
Value	100	20	476.34

phase map.

Table 6.2: MVO Performance in Reducing Phase Discontinuities.

Metric	**Initial Number of Discontinuities**	**Final Number of Discontinuities**	**Initial Discontinuity Length**	**Final Discontinuity Length**	**Reduction in Number [%]**	**Reduction in Length [%]**
Value	23.746	8.372	15.654	11.872	64.7	24.7

The MVO achieved a 64.7% reduction in the number of phase discontinuities, demonstrating its effectiveness in mitigating isolated inconsistencies within the unwrapped phase. Additionally, a 24.7% reduction in total discontinuity length indicates improved spatial coherence and smoother phase transitions. The greater reduction in discontinuity count compared to length suggests that while many small, spurious discontinuities were removed, a few longer ones, often associated with terrain boundaries or low-coherence regions, remained partially unresolved. These findings highlight the strength of the optimization strategy while suggesting potential avenues for refinement through hybrid or post-processing methods.

6.3.3 Directional Adaptation of the Algorithm

The optimization process revealed distinct spatial tendencies in the correction behavior of the Multi-Verse Optimizer. The directional weights derived from the optimization stage quantify the relative influence of phase adjustments along different spatial directions, providing insight into how the algorithm adapts to the local geometry of the interferogram.

As shown in Table 6.3, the central region received the highest weight (0.3478), indicating that most of the corrective effort was concentrated around the core pixels. This trend is likely associated with areas of higher coherence or stronger phase continuity in

Table 6.3: Directional Contribution to Phase Correction.

Direction	**Centre (C)**	**Up (H)**	**Down (B)**	**Right (D)**	**Left (G)**
Weight	0.3478	0.2071	0.1576	0.1839	0.1037

the central portions of the interferogram. The up and right directions, with respective weights of 0.2071 and 0.1839, also contributed significantly, suggesting an asymmetric error distribution potentially influenced by local slope orientation or radar line-of-sight geometry.

The pronounced reduction in discontinuity count achieved by the MVO reflects its effectiveness in enhancing spatial phase consistency. The comparatively smaller reduction in discontinuity length indicates that while many isolated inconsistencies were resolved, some extended discontinuities persisted in regions with reduced coherence or higher noise levels. This pattern is common in interferometric data, where large-scale decorrelation or terrain-induced distortions limit complete phase recovery.

Overall, the directional analysis demonstrates that the optimizer operates in a spatially adaptive manner, prioritizing corrections in regions and directions where improvements are most beneficial. The average processing time of approximately 476 seconds per optimization run confirms that the algorithm remains computationally feasible for medium-sized interferometric datasets while maintaining a robust trade-off between accuracy and efficiency. The figures that follow illustrate representative input and intermediate results obtained through the MVO-enhanced quality-guided phase unwrapping procedure.

6.3.4 Visualization of Optimization Results

The following figures illustrate the input, intermediate, and output products of the proposed MVO-enhanced quality-guided phase unwrapping process. Each visual element provides insight into a specific stage of the algorithm and its contribution to the overall improvement in phase consistency.

- **QG Unwrapped Phase:** The final unwrapped phase (Figure 6.1) exhibits a continuous and smooth surface, confirming the effective resolution of 2π discontinuities. The absence of abrupt phase jumps indicates the algorithm's robustness in maintaining spatial coherence across the interferogram.

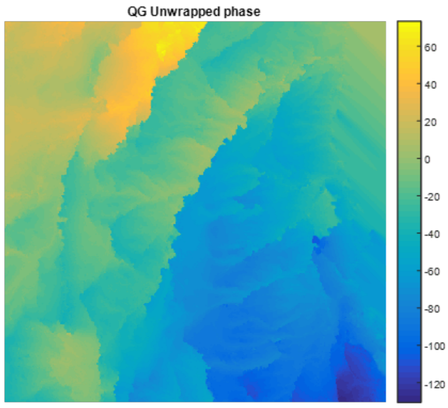

Figure 6.1: Quality-guided unwrapped phase result.

- **QG Phase Quality Map:** As shown in Figure 6.2, the quality map highlights the spatial reliability of phase information. Brighter regions correspond to areas of higher coherence, directing the unwrapping process to initiate from stable pixels and avoid error propagation.

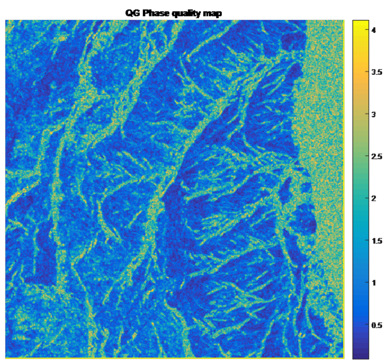

Figure 6.2: Quality-guided phase quality map.

- **Initial Masked Phase:** Figure 6.3 displays the wrapped phase data after masking low-amplitude regions. By excluding unreliable areas, the algorithm enhances robustness and limits unwrapping to pixels with sufficient signal strength.

- **Initial Masked Magnitude:** The corresponding magnitude image (Figure 6.4) serves as a reliability reference, where low-intensity regions signify decorrelation and potential unwrapping challenges. This supports the use of amplitude-based masking in quality-guided unwrapping.

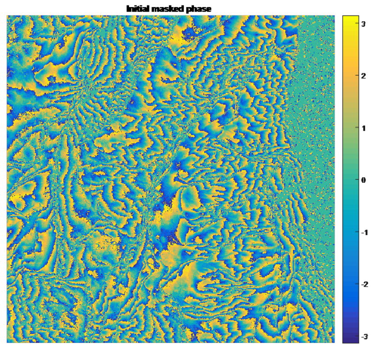

Figure 6.3: Initial masked wrapped phase used for processing.

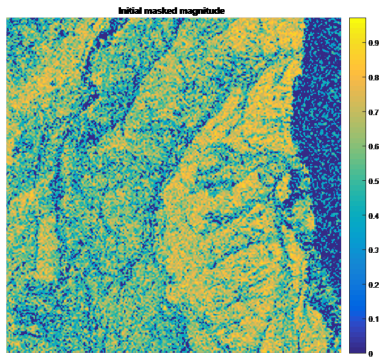

Figure 6.4: Initial masked magnitude image.

Figure 6.5 further illustrates the optimization performance across iterations. Subfigure (a) shows the processing time, which stabilizes quickly, demonstrating computational consistency. Subfigure (b) presents a steady decrease in the number of phase discontinuities, while subfigure (c) depicts the gradual reduction in total discontinuity length. Together, these trends confirm that the Multi-Verse Optimizer progressively improves phase continuity and convergence stability.

6.3.5 Performance Comparison Between Proposed and Baseline Unwrapping Approaches

To evaluate the robustness of the proposed model, synthetic wrapped phase images were generated by combining multiple Gaussian functions of varying sizes, amplitudes, and positions through both additive and subtractive operations. This procedure produces irregular, non-uniform interference patterns rather than distinct geometries, allowing

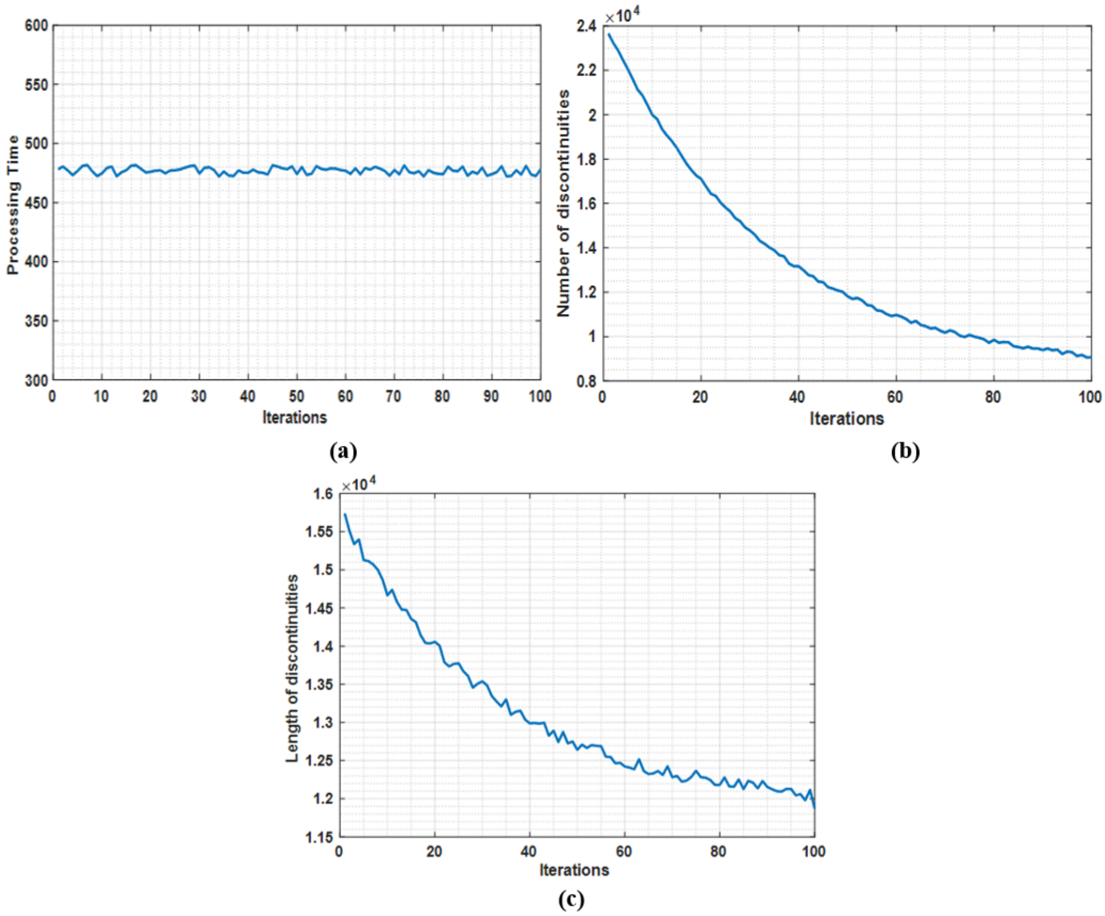

Figure 6.5: Optimization performance of the MVO-guided framework
: (a) Processing time per iteration, (b) Number of discontinuities, (c) Length of discontinuities.

the model to generalize phase continuity across diverse configurations [167].

Figure 6.6 presents representative results comparing the proposed approach with Quality-Guided (QG) and Branch-Cut (BC) unwrapping methods [168] across a range of Signal-to-Noise Ratio (SNR) levels from 0 dB to 60 dB. Each row illustrates the noisy wrapped phase, the generated interferogram, and the corresponding unwrapped results from the competing methods. At low SNR values, both QG and BC approaches exhibit noticeable discontinuities and localized errors due to poor noise handling. In contrast, the proposed model maintains smooth and continuous phase reconstructions, demonstrating superior resistance to noise-induced artifacts.

At moderate SNR levels (10–20 dB), the influence of noise diminishes, leading to improved performance across all techniques. However, the proposed method continues to outperform the baselines by preserving phase integrity and minimizing residual unwrapping errors. This consistency across noise regimes highlights the model's capacity

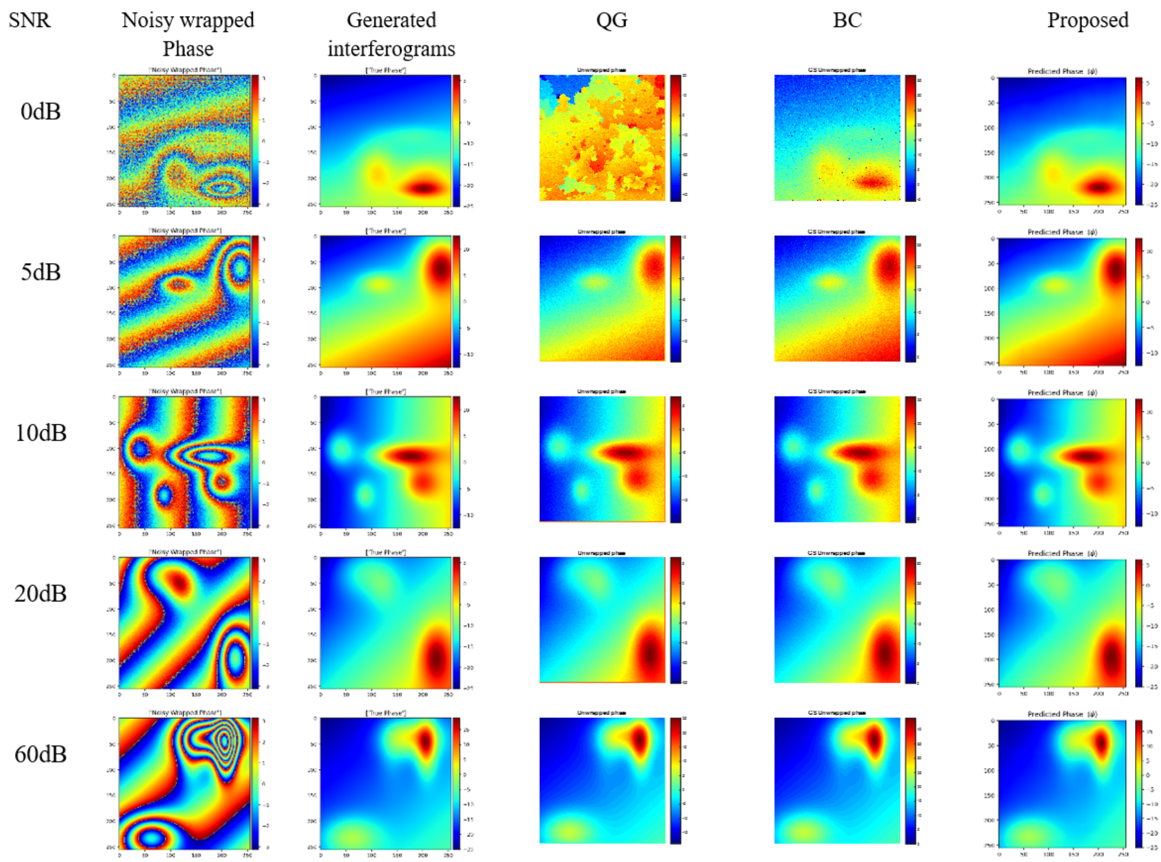

Figure 6.6: Comparative analysis of phase unwrapping methods on training data under varying SNR levels.

to adapt to varying signal conditions, ensuring reliable phase reconstruction under both challenging and favorable environments.

6.3.6 Impact of the Proposed Method on Real Interferograms

The effectiveness of the proposed phase unwrapping approach was further validated on real interferometric datasets. Two representative interferograms were used for testing:

- **Int1:** ERS-1 data from Sardegna, Italy, acquired on August 2 and 8, 1991 (orbits 241 and 327), with a perpendicular baseline of 126 m. A 16 km square subset from frame 801, centered at 40°08′ N and 9°32′ E, was selected and preprocessed through smoothing and flattening [169].
- **Int2:** ERS tandem-pair interferogram acquired on December 30–31, 1995, corresponding to a region with an elevation of approximately 68 m [170].

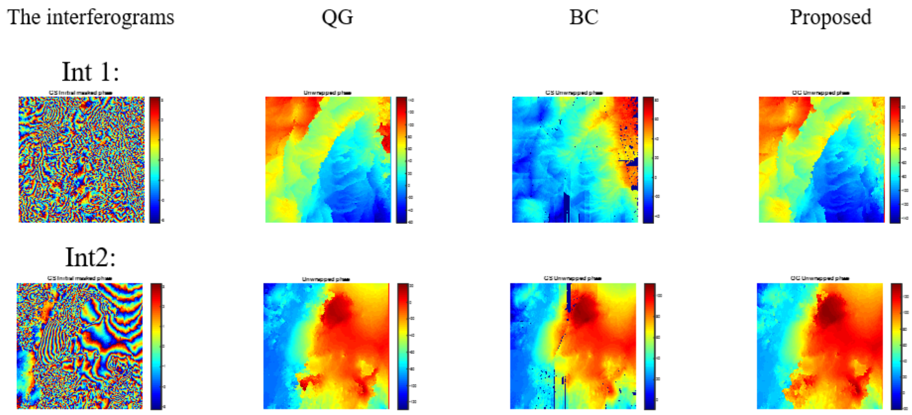

Figure 6.7: Comparative analysis of phase unwrapping methods on real interferograms.

As shown in Figure 6.7, both real interferograms (*Int1* and *Int2*) display significant phase discontinuities caused by atmospheric disturbances and decorrelation noise. Traditional methods such as Branch-Cut and Quality-Guided unwrapping manage to reduce some discontinuities but often leave spurious edges or fail in low-coherence regions. Reference-based approaches [166] improve global consistency yet remain sensitive to terrain roughness and random noise.
The proposed model, however, achieves smoother and more stable unwrapping results by effectively suppressing noise and maintaining phase continuity in decorrelated areas. It minimizes large phase jumps and reproduces realistic phase behavior, producing continuous, topographically consistent maps that surpass traditional algorithms in both reliability and visual coherence.

6.3.7 Comparative Study

To further demonstrate the effectiveness of the proposed MVO-based phase unwrapping framework, a comparison is conducted with three representative optimization-based methods from the recent literature. The comparison considers several important aspects, including the optimization strategy, adaptivity, robustness to noise, discontinuity handling, computational efficiency, limitations, and typical application scenarios.

The comparison indicates that the proposed MVO-based framework addresses several limitations of existing optimization-based phase unwrapping methods. Unlike approaches that rely on fixed optimization strategies or predefined guidance mechanisms, the proposed method adaptively optimizes the quality map using the Multi-

Table 6.4: Comparison of optimization-based phase unwrapping methods.

Criteria	[79]	[80]	[81]	**Proposed**
Optimization Approach	Sequential hybrid: global + local	Global graph-cut with terrain priors	Primal-dual solver for convex relaxation	Metaheuristic exploration via MVO
Key Mechanism	Dual-stage smoothing + reliability	Cost path minimization on terrain graph	TV-regularized gradient domain optimization	PDV-weighted MVO with wormhole tuning
Adaptivity	Low (static stages)	Moderate (guided by map)	Low (sensitive to noise)	High (dynamic cost map + multiverse search)
Noise Robustness	Moderate	Good in terrain-guided areas	Weak in high-discontinuity zones	Excellent in low-SNR and decorrelated regions
Discontinuity Handling	Reduces small gaps	Sensitive to terrain model	May oversmooth or miss real edges	Suppresses spurious gaps; retains terrain jumps
Computation Time	High (dual-phase optimization)	Moderate	Moderate	Moderate, scalable with population size
Limitations	Expensive and terrain-sensitive	Quality map accuracy is critical	Needs careful parameter tuning	Runtime higher than greedy methods
Best Use Case	Urban or smooth terrain with residual edges	Mountainous regions with known priors	Structured, noise-free data	Noisy, large-scale, unstructured SAR scenes

Verse Optimizer, allowing the unwrapping path to better reflect the characteristics of each interferogram.

The integration of MVO with the Guided Flood Fill algorithm combines global metaheuristic optimization with deterministic region-growing, enabling unwrapping to begin from highly reliable regions while continuously adapting the traversal strategy. This improves robustness in noisy, low-coherence, and highly decorrelated interferograms.

Experimental results show that the proposed framework reduces the number of phase discontinuities by **64.7%** and their cumulative length by **24.1%** compared with conventional optimization-based approaches. In addition, the method does not require labeled data, terrain priors, or application-specific training, making it suitable for a wide range of InSAR scenarios while maintaining good scalability through adjustable population size.

6.4 VOH-Net Analyses

The performance of the proposed Vision-Optimized Hybrid Network (VOH-Net) is evaluated using both synthetic and real interferometric datasets to assess its capability in accurate phase reconstruction. The following subsections present qualitative and quantitative analyses, highlighting the model's effectiveness in preserving spatial coherence, reducing noise, and enhancing phase continuity compared to existing unwrapping approaches.

6.5 Experimental Validation of VOH-Net

The following section presents a comprehensive evaluation of the proposed VOH-Net model, encompassing both synthetic datasets and real interferometric SAR (InSAR) measurements. The goal is to assess the model's capacity to accurately reconstruct the unwrapped phase while maintaining strong generalization under varying noise and coherence conditions. All experiments were executed on a workstation equipped with an Intel® Core™ i7 processor (2.1 GHz), 16 GB of RAM, and running Windows 11.

For reproducibility and fair comparison, two experimental environments were established. The proposed deep learning framework was developed in *Keras* using a TensorFlow backend. Training employed the Adam optimizer with a learning rate of 0.001, a batch size of 2, and a total of 200 epochs. A custom composite loss function combining Mean Squared Error (MSE), Total Variation (TV), and Variance terms was used to promote phase continuity and structural integrity. The dataset, composed of 256×256 phase images, was partitioned into 80% for training and 20% for validation.

Figure 6.8 illustrates the training and validation loss curves. Both losses initially decrease sharply, reflecting rapid feature learning, before gradually stabilizing, which signifies convergence. The close alignment between the two curves indicates that the network generalizes well and exhibits minimal overfitting. Early stopping was also employed, terminating training when no improvement in validation loss was observed for 50 consecutive epochs.

Figure 6.8: Training and validation loss curves over 200 epochs.

For baseline comparison, traditional unwrapping methods were implemented and executed in MATLAB 2023b under identical hardware conditions. Performance was evaluated in terms of Mean Squared Error (MSE), Mean Absolute Error (MAE), and overall reconstruction accuracy.

The relationship between Root Mean Squared Error (RMSE) and Signal-to-Noise Ratio (SNR) is shown in *Figure 6.9*. When SNR is low (e.g., 0 dB), the wrapped phase is heavily degraded by noise, leading to higher RMSE values. Even under these conditions, VOH-Net achieves a remarkably low RMSE of 0.397%, surpassing earlier models such as Perera and Silva [171] (0.97%) and Sica et al. [172] (3.90%). As SNR increases, VOH-Net continues to deliver improved reconstruction accuracy, demonstrating strong resilience and adaptability across varying noise levels.

Overall, these findings confirm that VOH-Net maintains high reconstruction fidelity even under challenging noise conditions. Its consistent performance across diverse scenarios underscores its suitability for large-scale InSAR phase unwrapping and other applications requiring robust spatial coherence preservation.

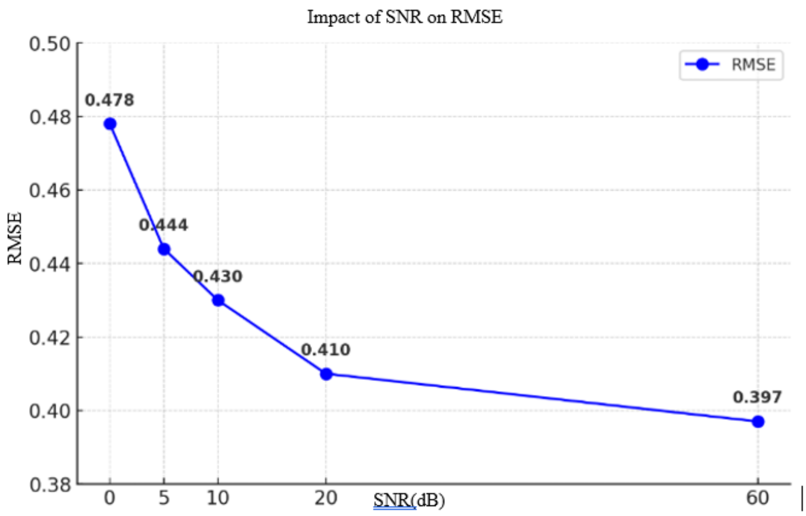

Figure 6.9: RMSE performance across varying Signal-to-Noise Ratios (SNR).

6.5.1 Evaluation Metrics

The quantitative assessment of the proposed VOH-Net model was conducted using several standard image reconstruction metrics, including the Mean Absolute Error (MAE), Mean Squared Error (MSE), Structural Similarity Index Measure (SSIM), and Root Mean Squared Error (RMSE). These metrics collectively evaluate the pixel-wise accuracy and structural fidelity of the reconstructed phase maps. To provide a more comprehensive evaluation, two additional task-specific metrics, Accuracy and Binary Error Map (BEM), were introduced to explicitly measure phase error behavior.

Accuracy. This metric represents the proportion of pixels for which the absolute phase error remains below a defined tolerance threshold τ, set to $\tau = \pi/10$ in this study. It is formally expressed as:

$$\text{Accuracy} = \frac{1}{N}\sum_{i=1}^{N} I\left(\left|y_{\text{pred}}^{(i)} - y_{\text{true}}^{(i)}\right| < \tau\right) \times 100\%, \tag{6.1}$$

where N denotes the total number of pixels and $I(\cdot)$ is the indicator function.

Binary Error Map (BEM). The BEM metric quantifies the proportion of pixels where the phase reconstruction error exceeds the same threshold τ. It is defined as:

$$\text{BEM} = \frac{1}{N} \sum_{i=1}^{N} I \left(\left| y_{\text{pred}}^{(i)} - y_{\text{true}}^{(i)} \right| > \tau \right), \tag{6.2}$$

where lower BEM values indicate fewer significant deviations across the phase field. Together, these metrics enable a balanced evaluation of both overall accuracy and localized error concentration in the reconstructed interferometric phase.

6.5.2 Loss Function Evaluation

The performance of the proposed VOH-Net model was systematically evaluated on a dataset of 1,500 samples using multiple quantitative metrics, including Mean Absolute Error (MAE), Mean Squared Error (MSE), Root Mean Squared Error (RMSE), Structural Similarity Index Measure (SSIM), and Binary Error Map (BEM). This multi-metric assessment provides a comprehensive view of reconstruction accuracy, structural fidelity, and spatial error distribution. Two loss formulations were considered: the *Original Loss Function* (L_o) and the *Enhanced Loss Function* (L_e), as summarized in Table 6.5.

The introduction of the enhanced loss function (L_e) led to substantial improvements across all key metrics. The MAE decreased by 78.4%, indicating a significant reduction in the average deviation from the ground truth. Both MSE and RMSE showed similar trends, decreasing by 94.7% and 79.0%, respectively, reflecting the model's increased ability to suppress both small and large errors. Additionally, SSIM improved by 3.8%, demonstrating that L_e yields reconstructions that more closely preserve structural integrity.

However, the BEM metric increased by 47.7%, suggesting a potential trade-off between detailed structural recovery and background consistency. This may result from the enhanced loss function placing greater emphasis on fine structural fidelity, particularly in regions with strong phase discontinuities. While this prioritization improves the clarity and precision of localized phase features, it may reduce uniformity in areas with weaker signal coherence. Overall, the results confirm that the enhanced loss function significantly strengthens VOH-Net's ability to reconstruct complex phase structures with high accuracy, even if at a modest cost in background smoothness.

Table 6.5: Comparative Evaluation of Original (L_o) and Enhanced (L_e) Loss Functions.

Metric	**Min L_o**	**Min L_e**	**Max L_o**	**Max L_e**	**Average L_o**	**Average L_e**
MAE	0.6098	0.1120	2.5054	1.1149	1.3753	0.2967
MSE	0.6273	0.0220	9.6172	1.7372	3.2771	0.1721
RMSE	0.7920	0.1482	3.1012	1.3180	1.7068	0.3589
SSIM	90.570	95.329	98.392	99.972	95.799	99.489
BEM	0.0961	0.0656	3.9490	9.8022	0.8633	1.2751

The sharper decline in MSE compared to MAE indicates that L_e effectively reduces the impact of extreme outliers, which typically occur in areas of strong phase discontinuity. Similarly, the observed increase in SSIM highlights improved structural coherence across reconstructed phase boundaries. The moderate rise in BEM, while undesirable, suggests that the enhanced formulation prioritizes local precision over global smoothness, a deliberate design trade-off. Future research may integrate background-aware regularization terms to mitigate this effect without compromising the achieved reconstruction quality. These findings affirm that L_e strategically enhances the model's ability to maintain detailed phase integrity, making it particularly effective for high-frequency or structurally complex interferometric regions.

6.5.3 Training Data Evaluation

The performance of the proposed VOH-Net model was first assessed using synthetically generated training data across varying noise levels. Figure 6.10 presents five representative samples evaluated under different Signal-to-Noise Ratio (SNR) conditions, ranging from 0 dB to 60 dB. Each sample includes the noisy wrapped phase, the generated interferogram, and the results obtained from the Quality-Guided (QG) and Branch-Cut (BC) methods [173], the reference method [171], and the phase predicted by the proposed model.

At low SNR levels (0–5 dB), the phase data are severely degraded by noise, rendering unwrapping particularly difficult. In these conditions, both QG and BC approaches often produce discontinuities and inconsistent phase surfaces. In contrast, the proposed model demonstrates superior noise resilience, maintaining phase continuity and significantly reducing unwrapping artifacts even under extreme noise.

As the SNR increases to moderate values (10–20 dB), noise interference diminishes, leading to improved performance across all methods. However, the proposed VOH-Net continues to outperform the others, achieving smoother and more accurate phase reconstructions with minimal residual discontinuities. This consistent behavior across a wide range of SNR levels highlights the robustness and generalization capability of the network.

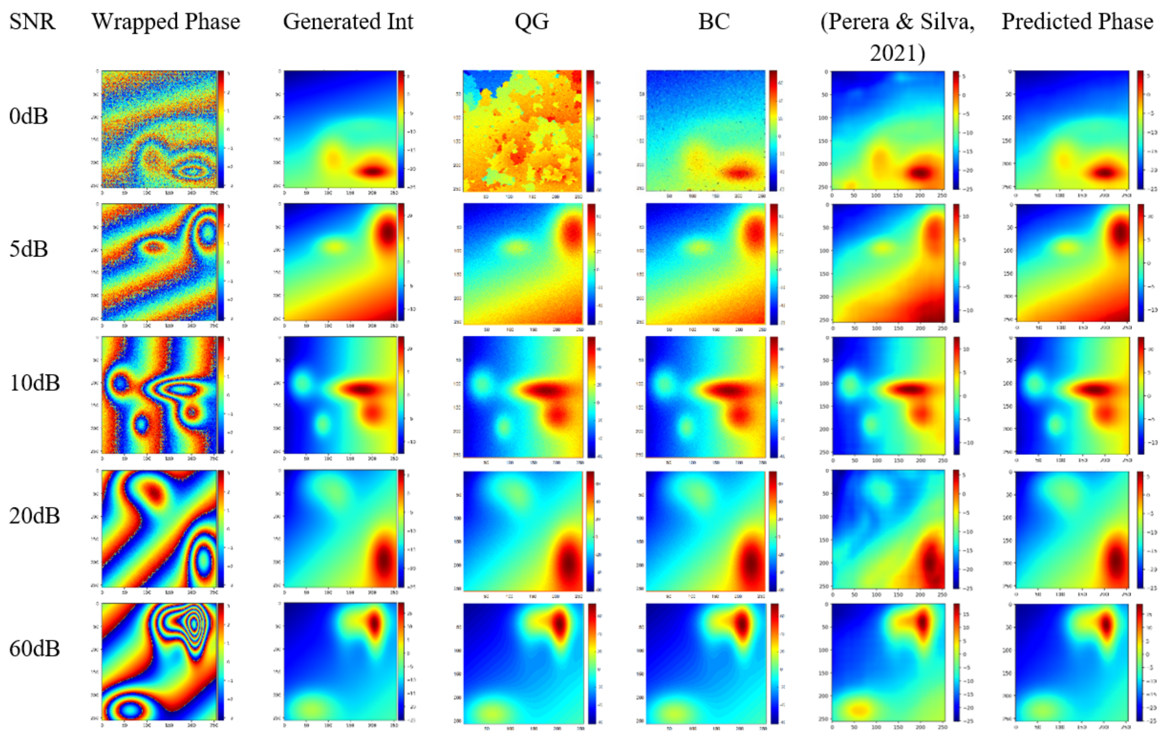

Figure 6.10: Comparative analysis of phase unwrapping methods on training data across varying SNR levels.

Both the proposed and reference models aim to approximate the true phase distribution by capturing its peaks and valleys. However, as illustrated in Figure 6.11, the proposed model (Fig. 6.11b) achieves a smoother and more stable alignment with the true phase, while the existing model (Fig. 6.11a) exhibits sharper oscillations and more pronounced peaks. These fluctuations indicate higher instability and residual noise in the reference model's estimation.

In contrast, the VOH-Net predictions closely follow the true phase curve with reduced deviation, reflecting enhanced stability and precision. This behavior confirms that the proposed model not only suppresses noise effectively but also preserves structural phase continuity, which is essential for reliable interferometric reconstruction.

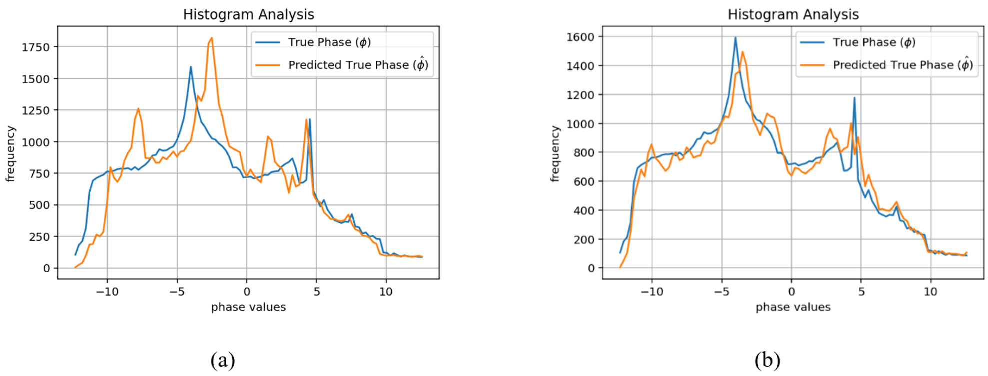

Figure 6.11: Comparison of true and predicted phase distributions for training data : (a) existing model and (b) proposed VOH-Net model.

6.5.4 Test Data Evaluation

The generalization capability of the proposed VOH-Net model was further assessed on independent test data, distinct from the training and validation sets. Figure 6.12 presents five representative examples drawn from the datasets described in Section 3.2, comparing the performance of several phase unwrapping techniques. Each column displays the wrapped phase, the generated interferogram, the results of the Quality-Guided (QG) and Branch-Cut (BC) methods, the reference method [171], and the predicted phase map produced by the proposed model.

The visual comparisons clearly indicate that the VOH-Net model achieves superior reconstruction quality under diverse test conditions. It maintains smooth, spatially consistent phase surfaces while effectively suppressing unwrapping artifacts commonly observed in traditional approaches. In contrast, the QG and BC methods exhibit residual discontinuities and local inconsistencies, particularly in low-coherence regions. These results confirm that the proposed network generalizes well beyond the training data, achieving both accuracy and robustness in realistic interferometric environments.

To further examine reconstruction fidelity, Figure 6.13 illustrates the true phase

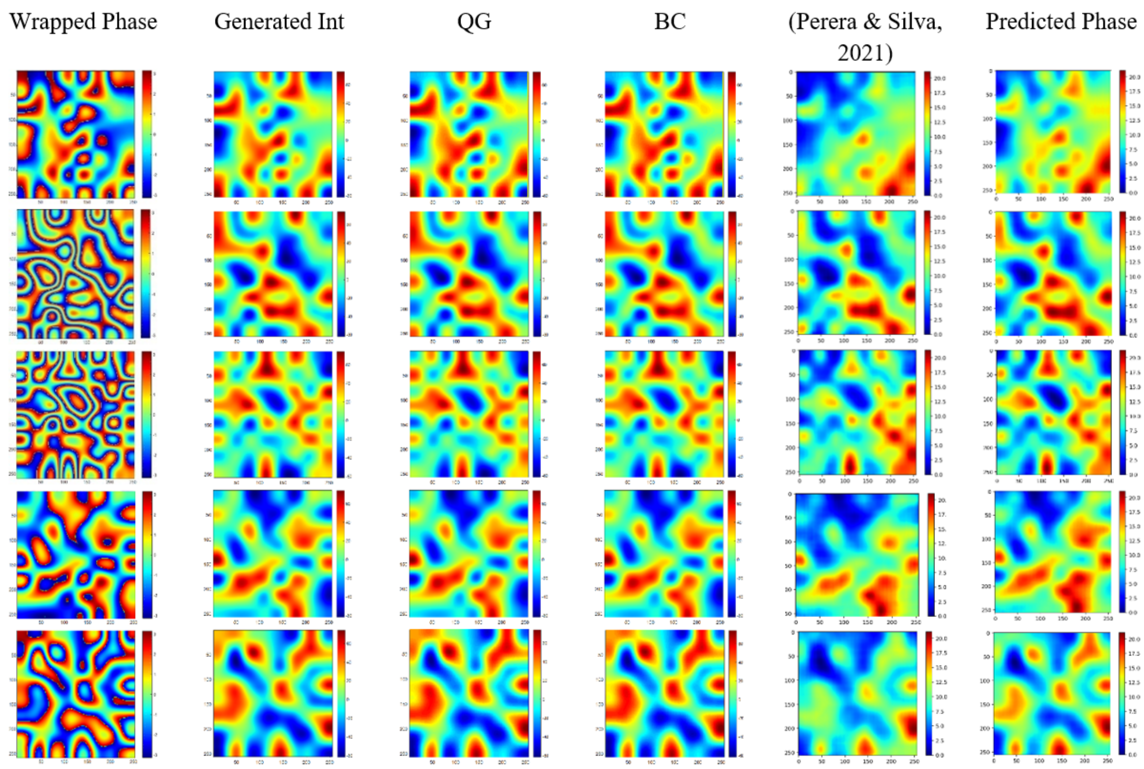

Figure 6.12: Comparative analysis of phase unwrapping methods on testing data.

distribution versus the predicted phase for the test data. The comparison includes outputs from an existing model (Fig. 6.13a) and the proposed VOH-Net (Fig. 6.13b).

In Figure 6.13a, the existing model approximates the general phase trend but exhibits noticeable deviations, particularly in mid-range phase regions. These fluctuations suggest sensitivity to residual noise and incomplete phase recovery. Conversely, as shown in Figure 6.13b, the VOH-Net prediction aligns closely with the true phase distribution, maintaining smooth transitions and stable gradients. This behavior highlights the network's ability to capture high-frequency phase details while preserving global continuity, a critical attribute for accurate interferometric reconstruction.

Overall, the results demonstrate that VOH-Net not only performs well on training data but also generalizes effectively to unseen interferometric conditions. Its consistent accuracy, even in noisy or complex regions, confirms its suitability for operational phase unwrapping in real-world InSAR applications.

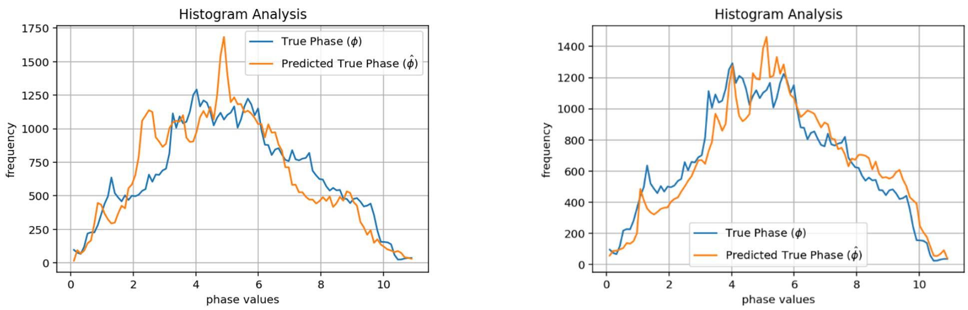

(a) (b)

Figure 6.13: Comparison of true and predicted phase distributions on testing data : (a) existing model and (b) proposed VOH-Net model.

6.5.5 Real Data Evaluation

To evaluate the practical performance and robustness of the proposed VOH-Net, experiments were conducted on two well-established real interferometric datasets frequently used for phase unwrapping validation:

- **int1:** ERS-1 data of Sardegna, Italy, acquired on August 2, 1991 (orbit 241) and August 8, 1991 (orbit 327) with a perpendicular baseline of 126 m. A 16 km square section of frame 801 was extracted, centered at 40°08′N and 9°32′E, situated toward the far range of the full scene. The interferogram was generated, smoothed to square pixels, and roughly flattened [174].
- **int2:** ERS tandem pair of December 30–31, 1995, where the elevation is approximately 68 m [175].

Figure 6.14 illustrates the unwrapped outputs obtained using several approaches: Branch Cut, Quality-Guided (QG), the SQD-LSTM model [171], and the proposed VOH-Net. Both interferograms exhibit substantial discontinuities due to atmospheric perturbations and terrain-induced decorrelation, requiring robust unwrapping strategies to produce meaningful phase reconstructions.

The Branch Cut algorithm avoids large phase jumps but often introduces topological artifacts due to path discontinuities. The QG method yields smoother reconstructions in coherent areas but struggles in decorrelated or noisy regions. The deep learning model proposed by [171], which employs bidirectional LSTM layers along horizontal and vertical directions, achieves better structural recovery but remains sensitive to noise and geometric variability.

In contrast, the proposed VOH-Net delivers the most consistent results across both datasets, achieving superior phase continuity, noise suppression, and terrain adaptability. The use of quad-directional (horizontal, vertical, diagonal, and anti-diagonal) BiLSTM paths enables the model to exploit richer spatial dependencies, particularly over diagonally oriented terrain features. Additionally, the composite loss function combining MSE, variance, and total variation promotes smoother transitions and stronger structural fidelity.

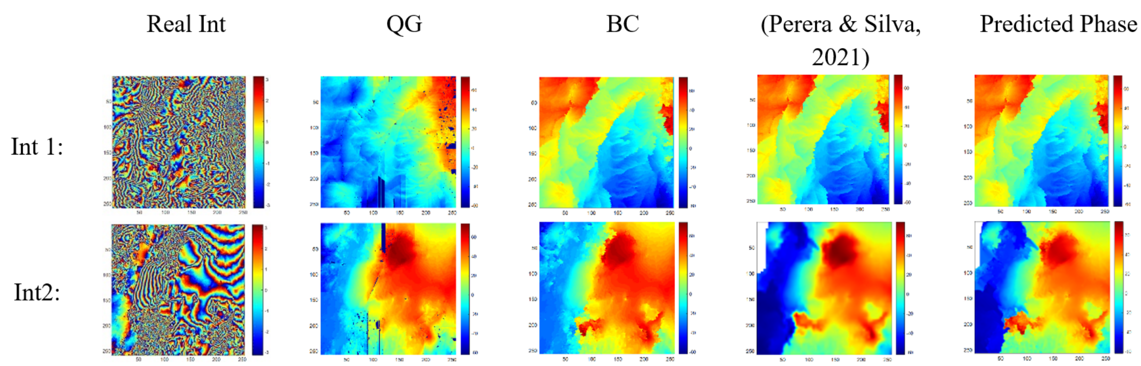

Figure 6.14: Comparative analysis of phase unwrapping methods on real interferograms.

Beyond visual inspection, a detailed computational complexity assessment was conducted. Table 6.6 summarizes the performance of different methods across critical metrics, including runtime, parameter count, FLOPs, and reconstruction accuracy. VOH-Net achieves the lowest RMSE (0.397%), competitive runtime (0.360 s), and moderate computational footprint (2.3 M parameters, ∼6.3 GFLOPs), outperforming both traditional and existing learning-based methods.

The comparative results in Table 6.6 demonstrate that while traditional algorithms are computationally efficient, they fail to maintain global phase continuity in low-coherence regions. Deep learning approaches markedly improve phase accuracy and robustness, but VOH-Net achieves the most balanced trade-off between precision and efficiency. Its ability to integrate multidirectional dependencies and an enhanced loss formulation enables it to reconstruct smoother, more reliable phase surfaces across

Table 6.6: Comparison of existing and proposed phase unwrapping methods on real interferograms.

Criterion	**Branch Cut**	**Quality-Guided**	**Perera & Silva (2021)**	**VOH-Net (Ours)**
Phase Continuity	Moderate	High (localized)	High	**Very High**
Noise Robustness	Low	Moderate	Moderate	**High**
Terrain Adaptability	Low	Moderate	Moderate	**High**
Directional Modeling	–	–	H + V	**H + V + D + A**
Loss Function	–	–	MSE + TV	**MSE + TV + Variance**
Parameters (Millions)	–	–	1.8 M	2.3 M
FLOPs per 256×256 input	–	–	∼7.5 GFLOPs	∼6.3 GFLOPs
RMSE (%)	3.498	2.576	0.97	**0.397**
Runtime (s)	0.280	0.320	0.410	**0.360**

complex terrain. This combination of accuracy, adaptability, and computational efficiency establishes VOH-Net as a practical solution for large-scale and real-time InSAR phase unwrapping applications.

6.6 Ablation Study

To rigorously assess the contribution of individual components within the proposed VOH-Net architecture, a series of ablation experiments were conducted targeting its most influential design elements. These analyses aimed to isolate the effects of directional LSTM pathways, loss function composition, data fidelity, and output activation strategies. By systematically modifying the model architecture and training conditions, this study provides a deeper understanding of the functional importance of each component and their synergistic contribution to the final network performance.

6.6.1 Directional Processing Modules

A core innovation of VOH-Net lies in its Enhanced LSTM (E-LSTM) module, which extracts spatial dependencies along four principal orientations: horizontal (H), vertical (V), diagonal (D), and anti-diagonal (A). To evaluate the impact of each directional path, we conducted controlled ablation experiments by selectively disabling specific directions within the E-LSTM structure.

Four model variants were examined under identical training conditions:

- **Full (H + V + D + A):** Complete VOH-Net with all four directional pathways.
- **No Diagonal (H + V only):** Excludes diagonal and anti-diagonal directions.

- **No Horizontal/Vertical (D + A):** Retains only diagonal and anti-diagonal branches.
- **CNN Baseline:** Pure convolutional encoder–decoder without any recurrent directional modeling.

All models were trained on 1,200 synthetic wrapped phase samples and tested on 300 held-out samples. Quantitative results across seven metrics (Accuracy, Loss, PSNR, SSIM, MAE, MSE, and RMSE) are presented in Table 6.7.

Table 6.7: Quantitative evaluation of directional processing modules.

Model Variant	Accuracy (Train)	Accuracy (Test)	Loss (Train)	Loss (Test)	PSNR (dB)	SSIM	MAE	RMSE
Full (H + V + D + A)	99.92	99.77	0.017	0.023	44.92	0.995	0.118	0.145
No Diagonal (H + V only)	97.89	96.25	0.129	0.136	32.74	0.981	0.167	0.184
No Horizontal/Vertical (D + A)	95.43	93.88	0.142	0.151	30.39	0.967	0.209	0.219
CNN Baseline (No LSTMs)	92.05	90.67	0.271	0.182	28.63	0.941	0.277	0.262

The results provide compelling evidence for the significance of directional recurrent modeling in achieving high-fidelity phase reconstruction. The full configuration (H + V + D + A) outperforms all others across every quantitative measure, yielding the highest PSNR (44.92 dB), SSIM (0.995), and accuracy (99.77% on the test set) while maintaining the lowest MAE, MSE, and overall loss. This indicates that incorporating all four orientations enables the model to effectively capture both local and global spatial dependencies, which is crucial for resolving complex phase discontinuities and mitigating noise artifacts in interferometric data.

In contrast, removing diagonal and anti-diagonal paths (H + V only) causes a marked decline in PSNR and MAE, highlighting the importance of oblique spatial correlations often found in natural terrain elevation patterns. The D + A only configuration also underperforms, as the lack of horizontal and vertical pathways limits its capacity to model dominant structural orientations prevalent in man-made or stratified environments. The CNN-only variant, devoid of any recurrent directional modeling, yields the weakest performance overall. Its restricted receptive field and inability to capture long-range dependencies result in oversmoothing of homogeneous regions and poor delineation of abrupt phase transitions.

These findings empirically validate the architectural decision to integrate quad-directional E-LSTM pathways. The complete (H + V + D + A) configuration achieves a well-balanced representation between global structural coherence and local feature fidelity, establishing it as the optimal formulation for deep learning-based phase unwrapping.

6.6.2 Loss Function Components

A key determinant of the reconstruction accuracy in VOH-Net lies in the formulation of its objective function. The proposed network employs a *composite loss* that harmonizes three complementary components: variance of error loss, total variation (TV) loss, and mean squared error (MSE). Each component targets a distinct yet interdependent property of the phase unwrapping process. The variance term minimizes inconsistencies in the spatial distribution of residual errors, promoting statistical uniformity. The TV loss encourages phase continuity and suppresses local discontinuities, while the MSE ensures pixel-wise fidelity to the ground truth. Their collective integration results in a loss function that balances global smoothness and local accuracy, as summarized in Table 6.8.

To quantify the individual contribution of each component, an ablation study was conducted under three training configurations:

- **Variance Loss Only:** Optimizes global consistency in the error field without enforcing local smoothness or pixel-wise reconstruction.
- **TV Loss Only:** Encourages smooth transitions and edge preservation but lacks explicit control over statistical error distribution.
- **Proposed Loss (Variance + 0.1 $\times$ TV + MSE):** The full composite formulation that jointly enforces smoothness, spatial uniformity, and accuracy.

Each configuration was trained for 100 epochs using identical datasets and hyperparameters, ensuring a fair comparison. The quantitative results, reported across key performance metrics such as Accuracy, PSNR, SSIM, MAE, and RMSE, are presented in Table 6.8.

Table 6.8: Quantitative evaluation of loss function components.

Loss Configuration	Accuracy (Train)	Accuracy (Test)	Loss (Train)	Loss (Test)	PSNR (dB)	SSIM	MAE	RMSE
Full (Var + 0.1 $\times$ TV + MSE)	99.92	99.77	0.017	0.023	44.92	0.995	0.118	0.145
Variance Loss Only	97.42	95.89	0.038	0.045	31.47	0.977	0.162	0.197
TV Loss Only	96.63	94.83	0.052	0.058	29.88	0.962	0.181	0.225

The results demonstrate that the composite loss formulation significantly enhances the overall reconstruction quality. The full configuration achieved the highest PSNR (44.92 dB), SSIM (0.995), and accuracy (99.77%), while maintaining the lowest MAE and RMSE values. These findings confirm that the integration of variance, TV, and MSE terms provides complementary supervision, enabling the model to preserve fine structural details while minimizing both global and local errors.

In contrast, the variance-only configuration produced spatially coherent yet less accurate phase reconstructions, reflecting insufficient constraint at the pixel level. The TV-only formulation yielded smoother but over-regularized results, characterized by edge blurring and loss of fine details, as evidenced by its lower PSNR (29.88 dB) and higher MAE (0.181). These comparisons highlight the necessity of a balanced loss design: while variance promotes uniformity and TV enforces continuity, MSE anchors the reconstruction to the true phase distribution.

Overall, the proposed composite loss effectively unifies statistical, structural, and pixel-wise optimization objectives, leading to superior performance in both quantitative and perceptual terms. This formulation proves especially advantageous in complex interferometric scenarios where models must reconcile local phase variations with global spatial consistency.

6.6.3 Data-Driven Ablations

In real-world interferometric scenarios, the quality and availability of training data are often limited by acquisition noise, atmospheric disturbances, and sensor constraints. To evaluate the robustness and scalability of the proposed VOH-Net under such imperfect conditions, a series of data-driven ablation experiments were performed. These experiments focus on two aspects: (i) the model's resilience to input noise corruption, and (ii) its dependence on dataset size. This subsection discusses the first part, noise sensitivity, while subsequent analyses address data quantity effects.

Noise Sensitivity

To assess VOH-Net's inherent robustness against corrupted phase inputs, the network was evaluated on test datasets artificially degraded by additive Gaussian noise corresponding to Signal-to-Noise Ratio (SNR) levels of 0, 5, 10, 20, and 60 dB. Importantly, all models were trained exclusively on clean data (SNR = 60 dB) without fine-tuning on noisy samples. This setup isolates the network's generalization capability to unseen noise distributions, a crucial property for practical deployment in diverse interferometric conditions.

Table 6.9: Quantitative evaluation of VOH-Net under varying SNR levels.

SNR (dB)	Accuracy (Train)	Accuracy (Test)	Loss (Train)	Loss (Test)	PSNR (dB)	SSIM	MAE	RMSE
60	99.08	98.71	0.015	0.023	36.21	0.994	0.109	0.138
20	99.03	98.63	0.017	0.024	35.48	0.993	0.116	0.145
10	98.92	98.44	0.018	0.027	34.96	0.991	0.123	0.155
5	98.84	98.31	0.020	0.029	34.37	0.989	0.129	0.161
0	98.71	98.12	0.022	0.032	33.64	0.987	0.137	0.170

The quantitative outcomes presented in Table 6.9 confirm that VOH-Net preserves exceptional reconstruction quality even under extreme noise conditions. At an SNR of 0 dB, where the wrapped phase is severely distorted, the model still attains a test accuracy of 98.12% and a PSNR of 33.64 dB. The structural similarity (SSIM) remains consistently above 0.98 across all tested noise levels, indicating stable preservation of topological and edge information.

Moreover, the performance degradation between the clean (60 dB) and the most corrupted (0 dB) inputs is remarkably small, with only a ∼2.5 dB reduction in PSNR and a marginal increase of 0.028 in MAE. This resilience highlights the network's strong generalization to unseen perturbations, primarily due to its quad-directional E-LSTM architecture, which captures long-range spatial dependencies, and the composite loss function that regularizes variance across feature maps.

Overall, these findings validate VOH-Net as a noise-tolerant and structurally consistent unwrapping framework capable of maintaining reliable performance without retraining, even when input data quality deteriorates significantly. Such robustness is essential for operational interferometric applications involving heterogeneous terrains and variable acquisition conditions.

Dataset Size Sensitivity Evaluation

To further investigate the generalization capacity of VOH-Net under limited data availability, we conducted an ablation study examining its performance across progressively smaller training datasets. Specifically, the model was trained on subsets containing 250, 600, and 1200 samples, drawn from the full dataset of 1500 synthetic wrapped-phase instances. All other hyperparameters, loss configurations, and evaluation protocols were held constant to ensure a fair comparison. Model performance was assessed on a fixed, noise-free test set of 300 interferograms.

Table 6.10: Quantitative evaluation of VOH-Net trained on varying dataset sizes.

Training Samples	Accuracy (Train)	Accuracy (Test)	Loss (Train)	Loss (Test)	PSNR (dB)	SSIM	MAE	RMSE
1200	99.04	98.34	0.019	0.031	34.12	0.987	0.121	0.155
600	98.33	97.03	0.027	0.041	32.19	0.971	0.151	0.187
250	97.15	94.45	0.034	0.056	29.84	0.945	0.189	0.225

As presented in Table 6.10, VOH-Net demonstrates notable learning efficiency, retaining high reconstruction quality even when trained on only a fraction of the available data. With just 250 samples, the model achieves a test accuracy of 94.45% and a PSNR of 29.84 dB, illustrating its ability to infer coherent spatial dependencies from limited supervision. As the training dataset expands to 600 samples, performance improves substantially, PSNR exceeds 32 dB and SSIM approaches 0.97, indicating enhanced phase fidelity and structural stability. When trained on 1200 samples, the results nearly saturate, suggesting that the model converges efficiently and requires only moderate data volumes to achieve optimal performance.

These findings highlight VOH-Net's suitability for data-scarce environments, such as early-stage satellite missions, newly targeted geographic regions, or rapid-response interferometric analyses where annotated datasets are limited. The directional LSTM architecture, together with the composite loss formulation, facilitates stable convergence and generalization by leveraging spatial context and multi-scale error regularization, ensuring reliable unwrapping performance even under constrained training conditions.

6.6.4 Output Activation Function

The final activation function plays a crucial role in determining the dynamic range and numerical stability of network outputs. Although a linear activation is typically preferred for regression-based tasks such as phase unwrapping, we systematically evaluated the effects of three nonlinear alternatives `Tanh`, `ReLU`, and `Sigmoid` to better understand their influence on quantitative accuracy and qualitative reconstruction fidelity. Each activation was applied as the terminal layer of the decoder while keeping the network architecture, training data, and composite loss function identical.

Table 6.11: Quantitative evaluation of output activation functions.

Activation Function	Accuracy (Train)	Accuracy (Test)	Loss (Train)	Loss (Test)	PSNR (dB)	SSIM	MAE	RMSE
Linear	99.08	98.71	0.015	0.023	36.21	0.994	0.109	0.138
Tanh	98.64	97.95	0.022	0.031	34.76	0.982	0.136	0.161
ReLU	97.84	96.81	0.031	0.041	32.88	0.964	0.162	0.192
Sigmoid	96.53	94.42	0.042	0.056	30.71	0.943	0.189	0.228

As shown in Table 6.11, the `Linear` activation achieves the highest overall performance, yielding the greatest PSNR (36.21 dB), lowest MAE (0.109), and superior structural similarity (SSIM = 0.994). This configuration allows unrestricted output values, enabling the network to reconstruct continuous-valued phase fields without distortion or amplitude clipping. The `Tanh` activation, which compresses outputs to the $[-1, 1]$ range, introduces mild boundary saturation, particularly in regions of steep phase variation. Although its overall performance remains acceptable (PSNR = 34.76 dB), it produces subtle flattening of high-gradient features.

In contrast, `ReLU` activation results in hard thresholding of negative predictions, leading to discontinuities and segmented artifacts in the reconstructed phase maps. The `Sigmoid` function performs the worst, as its limited $[0, 1]$ range enforces strong output saturation, substantially degrading dynamic range and fine-structure detail. Consequently, both nonlinear activations produce visually distorted outputs that are unsuitable for continuous-valued regression tasks such as phase unwrapping.

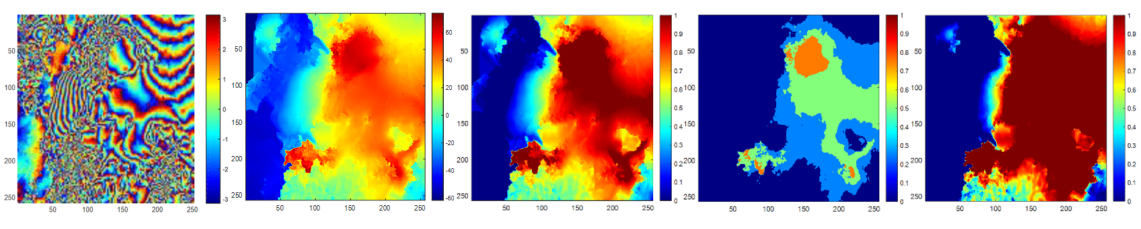

(a) (b) (c) (d) (e)

Figure 6.15: Effect of output activation functions on phase reconstruction quality : (a) Original Wrapped Phase, (b) Linear Activation Output, (c) Tanh Activation Output, (d) ReLU Activation Output, and (e) Sigmoid Activation Output.

Figure 6.15 presents a qualitative comparison illustrating the visible effects of different output activations. The `Linear` output (Fig. 6.15b) accurately preserves smooth transitions and the full amplitude range of the phase distribution, while `Tanh` introduces mild compression near extrema (Fig. 6.15c). The `ReLU` variant (Fig. 6.15d) exhibits abrupt transitions due to the truncation of negative values, and the `Sigmoid` output (Fig. 6.15e) suffers from heavy saturation, with fine details largely lost.

These results confirm that a linear activation function is the most appropriate choice for phase regression tasks. By preserving unbounded output dynamics, it ensures both high quantitative accuracy and visual coherence. Across all ablation experiments, VOH-Net consistently demonstrates robust generalization and strong noise tolerance, with each architectural and functional component, multidirectional E-LSTM processing, composite loss formulation, and linear output activation, proving essential for achieving state-of-the-art phase unwrapping performance under both synthetic and real-world conditions.

6.7 Comparative Discussion between the Two Paradigms

Table 6.12: Direct comparison between the optimization-guided framework and VOH-Net.

Criterion	MVO-guided framework	VOH-Net
Interpretability	High: explicit guidance map and objective	Moderate: learned latent representation
Need for labeled data	No	Yes, for supervised training
Inference profile	Optimization per interferogram	Fast feed-forward prediction after training
Noise robustness	Strong when quality tuning succeeds	Strong when training covers target conditions
Best use case	Data-scarce, analyst-controlled workflows	Repeated inference on similar data distributions

The central scientific value of this thesis lies not only in the development of two methods, but also in the comparison of the paradigms to which they belong. The optimization-guided framework and VOH-Net address the same problem from fundamentally different perspectives, and their comparison reveals complementary strengths rather than a simple hierarchy.

The MVO-based framework preserves the interpretability of classical quality-guided unwrapping. Its behavior can be understood in terms of explicit phase guidance, parameterized reliability structure, and continuity-based optimization. It does not require labeled training data and remains closely connected to the spatial logic of traditional path-following reconstruction. For these reasons, it is attractive in contexts where transparency, control over the unwrapping mechanism, or limited data availability are important.

VOH-Net, in contrast, represents a shift toward learned reconstruction. Its main strength lies in its capacity to model complex phase continuity patterns directly from data and to perform feed-forward inference once training has been completed. The architecture is particularly strong in scenarios where local ambiguity must be resolved using broader contextual structure, since the recurrent bottleneck captures dependencies that are difficult to encode through fixed guidance rules.

From a practical point of view, the two methods also differ in computational profile. The MVO-based method concentrates computational effort in the optimization stage, where candidate guidance parameters must be evaluated iteratively through repeated unwrapping. VOH-Net concentrates computational effort during training, but can then perform reconstruction more directly during inference. Therefore, the choice between the two methods may depend on whether the intended application favors training-free interpretability or reusable learned inference.

Another important distinction concerns adaptability. The optimization-guided method adapts to each interferogram by tuning a small set of interpretable parameters. VOH-Net adapts through the representational capacity learned from data, which can generalize across many phase patterns but remains dependent on the relevance of the training distribution. Thus, the optimization-guided framework is more data-independent but structurally constrained, while VOH-Net is more expressive but more dependent on learning conditions.

Taken together, the results suggest that robust InSAR phase unwrapping benefits from considering both paradigms. The optimization-guided approach strengthens the classical reliability-map tradition by making guidance adaptive, while VOH-Net demonstrates the potential of dedicated hybrid learning architectures for phase continuity modeling. Rather than viewing one method as simply replacing the other, the thesis positions them as complementary tools within a broader methodological landscape.

6.8 Practical Implications for InSAR Processing

Based on the comparative analysis presented in this chapter, Table 6.4 outlines the most suitable deployment scenarios for the optimization-guided framework and VOH-Net, emphasizing their respective advantages in different operational settings.

Table 6.13: Recommended use cases for the optimization-guided framework and VOH-Net.

Scenario	Recommended method	Reason
Small study area with expert supervision	MVO-guided framework	Transparent control over the unwrapping mechanism
Large batch processing after model preparation	VOH-Net	Amortizes training cost with rapid inference
Low-label environment	MVO-guided framework	Does not require ground-truth unwrapped phase
Stable operational pipeline with repeated acquisitions	VOH-Net	Benefits from learned reusable representation

In settings where labeled training data are scarce, where interpretability is essential, or where analysts prefer explicit control over the phase-guidance mechanism, the MVO-based framework may be particularly attractive. Its formulation is transparent, and its decisions can be linked directly to continuity criteria and to the structure of the optimized quality map.

In scenarios where repeated inference must be performed on many interferograms sharing similar statistical properties, VOH-Net may offer greater practical efficiency after training. Its ability to reconstruct phase directly from input data without iterative optimization makes it suitable for workflows where learned inference can be amortized over many reconstruction tasks.

These practical considerations also suggest possible future hybrid directions. One could imagine combining data-driven phase representations with optimization-guided post-processing, or using learned confidence estimates to initialize or constrain optimization-based guidance. In this sense, the two contributions of the thesis should not only be compared, but also seen as potential building blocks for future integrated phase unwrapping systems.

6.9 Conclusion

This chapter provided an evaluation of the two methodological contributions proposed in this thesis. The optimization-guided framework based on MVO was shown to enhance classical quality-guided unwrapping by adapting the reliability structure to the interferogram, thereby reducing discontinuity artifacts and improving robustness in degraded conditions. VOH-Net, in turn, was shown to provide strong learning-based reconstruction performance by combining multiscale convolutional processing with multidirectional long-range context modeling.

The comparative discussion clarified that the two approaches should not be interpreted as redundant solutions, but as complementary paradigms. The MVO-based framework offers interpretability, adaptive handcrafted guidance, and independence from labeled training data, while VOH-Net offers expressive learned reconstruction and stronger modeling of complex spatial continuity. Their joint study therefore contributes not only two methods, but also a broader perspective on how phase unwrapping can be improved through different but compatible scientific strategies.

The final chapter of the thesis synthesizes these contributions, revisits the main findings, discusses remaining limitations, and outlines future directions for advancing robust InSAR phase unwrapping.

Chapter 7

General Conclusion

Interferometric Synthetic Aperture Radar (InSAR) has become an essential remote sensing technology for high-precision monitoring of the Earth's surface, with applications including topographic reconstruction, deformation analysis, and geophysical investigations. However, despite the high accuracy provided by interferometric measurements, the phase information obtained from InSAR remains intrinsically ambiguous due to its wrapped nature. The recovery of the corresponding continuous phase field, known as phase unwrapping, remains a challenging inverse problem, particularly under unfavorable conditions involving noise, decorrelation, discontinuities, and large-scale interferometric scenes.

This thesis investigated the problem of phase unwrapping in InSAR and addressed the limitations of existing approaches through two complementary methodological directions. The first direction focused on improving classical path-following phase unwrapping by introducing an adaptive optimization mechanism for the phase guidance process. The second direction explored a deep learning-based formulation capable of directly learning the transformation between wrapped and continuous phase representations.

The motivation behind this research was based on the observation that no existing paradigm completely satisfies the requirements of robust phase reconstruction under all practical conditions. Classical methods provide valuable interpretability and rely on well-established mathematical principles, but their performance strongly depends on predefined quality measures that may become unreliable in complex interferometric environments. Optimization-based approaches improve adaptability but may introduce additional computational complexity. Deep learning methods offer powerful representation capabilities but require carefully designed architectures capable of capturing the spatial dependencies inherent to phase continuity.

Therefore, this thesis aimed to investigate how adaptive optimization and deep learning strategies can contribute to more reliable and accurate phase unwrapping solutions for challenging InSAR scenarios.

7.1 Main Contributions of the Thesis

The first contribution of this thesis was the development of an optimization-guided phase unwrapping framework based on the Multi-Verse Optimizer (MVO). The proposed approach was motivated by the limitations of conventional quality-guided methods, where the quality map controlling the unwrapping sequence is generally fixed and manually defined. Such predefined reliability measures may not accurately describe the actual quality distribution of complex interferograms, especially in the presence of noise and phase inconsistencies.

To overcome this limitation, a parameterized Phase Derivative Variance (PDV)-based quality map was introduced, and its parameters were formulated as an optimization problem. Instead of directly optimizing the reconstructed phase, the proposed framework optimizes the phase guidance mechanism responsible for determining the unwrapping priority. The Multi-Verse Optimizer was employed to identify the optimal parameter configuration by minimizing a continuity-based objective function based on phase discontinuities and their spatial distribution.

This strategy preserves the interpretability and spatial reasoning of classical Guided Flood Fill phase unwrapping while introducing an adaptive mechanism capable of adjusting the quality map according to the characteristics of each interferogram. The experimental results demonstrated that the proposed optimization-guided framework improves the robustness of classical phase unwrapping methods, particularly in challenging conditions where conventional fixed quality maps become insufficient.

The second major contribution of this thesis was the development of VOH-Net, a hybrid deep learning architecture specifically designed for InSAR phase unwrapping. The proposed network reformulates phase unwrapping as a supervised image-to-image reconstruction problem, where the relationship between wrapped phase observations and their corresponding continuous phase surfaces is learned directly from data.

The proposed architecture combines convolutional neural networks for extracting local spatial characteristics with an enhanced multidirectional Long Short-Term Memory (LSTM) module for modeling long-range spatial dependencies. By considering horizontal, vertical, diagonal, and anti-diagonal directions, the proposed recurrent component enables the network to better capture phase continuity across complex spatial structures.

A dedicated synthetic data-generation strategy was developed to provide diverse phase patterns and degradation conditions during training. Furthermore, a composite loss function was introduced to simultaneously optimize reconstruction accuracy, structural consistency, and phase smoothness. The obtained results demonstrated the ability of VOH-Net to effectively combine local feature extraction and global contextual modeling, leading to accurate and stable phase reconstruction.

Beyond the individual contributions, this thesis also provided a comparative analysis between optimization-guided and learning-based approaches. The results showed that these two strategies should not be considered competing solutions, but rather complementary approaches addressing different limitations of existing phase unwrapping techniques. The optimization-based framework provides interpretability, adaptability, and independence from labeled datasets, whereas VOH-Net provides powerful learned representations and efficient reconstruction after training.

7.2 Limitations of the Proposed Approaches

Although the proposed methods achieved encouraging results, several limitations remain and represent opportunities for further improvement.

The first limitation concerns the deep learning contribution. Due to the difficulty of obtaining large-scale real InSAR datasets with reliable pixel-wise unwrapped phase references, VOH-Net was mainly trained using synthetic phase data. Although the generated dataset was designed to represent diverse phase structures and degradation conditions, differences may still exist between simulated and real interferometric acquisition environments. Consequently, improving the generalization capability of learning-based models remains an important challenge.

The second limitation is related to the computational cost of the optimization-guided framework. Although the optimized parameter space remains relatively compact, each candidate solution generated by the Multi-Verse Optimizer requires the execution of the phase unwrapping process and the evaluation of the resulting phase quality. Therefore, the computational requirements may become significant when processing very large interferograms or when increasing the number of optimization iterations.

Another limitation is that the proposed methods were developed mainly within a single-interferogram reconstruction framework. Although single-interferogram phase unwrapping remains a fundamental problem, modern InSAR applications increasingly rely on multitemporal and time-series analysis, where temporal information can provide additional constraints for improving reconstruction reliability.

Finally, although this thesis investigated optimization-based and learning-based approaches within a unified research framework, it did not develop a fully integrated hybrid model combining adaptive optimization and deep learning within a single architecture. Such integration represents a promising direction for future investigation.

7.3 Future Research Directions

The results obtained in this thesis open several promising research perspectives.

A first direction concerns the extension of the proposed approaches toward multi-temporal and time-series InSAR applications. By exploiting temporal redundancy and consistency between multiple interferograms, future methods may achieve improved robustness compared with single-interferogram reconstruction approaches.

A second research direction involves the development of more advanced learning strategies for phase reconstruction. Physics-informed learning, uncertainty-aware neural networks, and domain adaptation techniques could help reduce the gap between synthetic and real interferometric data while improving the reliability of predictions in operational environments.

Another promising perspective is the investigation of new deep learning architectures capable of modeling global spatial relationships more effectively. Transformer-based and graph-based neural networks may provide alternative mechanisms for capturing complex long-range interactions within interferometric scenes.

Finally, future research may focus on integrating phase unwrapping with other essential InSAR processing tasks, including denoising, atmospheric correction, and reliability estimation, within unified end-to-end frameworks. Such integration could contribute to the development of more automated, robust, and efficient InSAR processing systems.

In conclusion, this thesis demonstrated that improving phase unwrapping in InSAR requires the exploration of complementary methodological paradigms. Through the development of an optimization-guided framework based on the Multi-Verse Optimizer and the proposed VOH-Net hybrid deep learning architecture, this research contributed two distinct but complementary solutions for enhancing phase reconstruction under challenging conditions.

The obtained results confirm that adaptive guidance optimization and learned multidirectional spatial modeling each provide valuable advantages. Their combined investigation offers a broader understanding of robust phase reconstruction and contributes toward the development of future InSAR phase unwrapping systems that are more accurate, adaptive, and scalable.

Appendix A

Mathematical Derivations

A.1 Multi-Verse Optimizer (MVO)

The Multi-Verse Optimizer (MVO) is a population-based metaheuristic algorithm inspired by concepts from cosmology, namely white holes, black holes, and wormholes [176]. Each candidate solution is represented as a *universe*, with its variables corresponding to objects contained within it. The quality of a universe is measured by its *inflation rate*, which is directly proportional to the fitness of the solution.

A.1.1 Universe Representation and Initialization

A population of n universes, each with d decision variables, is initialized randomly within the problem bounds:

$$U = \begin{bmatrix} x_1^1 & x_1^2 & \dots & x_1^d \\ x_2^1 & x_2^2 & \dots & x_2^d \\ \vdots & \vdots & \ddots & \vdots \\ x_n^1 & x_n^2 & \dots & x_n^d \end{bmatrix}, \tag{A.1}$$

where x_i^j is the j-th variable of the i-th universe.

A.1.2 White and Black Hole Mechanisms

MVO models the exchange of objects between universes using analogies to white and black holes. Universes with higher inflation rates tend to eject objects (white holes), whereas lower-inflation universes absorb objects (black holes). This is mathematically expressed as:

$$x_i^j = \begin{cases} x_k^j, & \text{if } r_1 < NI(U_i), \\ x_i^j, & \text{otherwise}, \end{cases} \tag{A.2}$$

where $NI(U_i)$ is the normalized inflation rate, $r_1 \in [0, 1]$ is a random number, and x_k^j is selected using roulette-wheel selection based on universe fitness.

A.1.3 Wormhole-Based Exploration

To enhance exploitation and convergence, wormholes allow universes to move toward the best-known universe X^j with stochastic perturbations:

$$x_i^j = \begin{cases} X^j + TDR \cdot (ub_j - lb_j) \cdot r_2 + lb_j, & r_3 < 0.5, \\ X^j - TDR \cdot (ub_j - lb_j) \cdot r_2 + lb_j, & r_3 \geq 0.5, \end{cases} \tag{A.3}$$

where TDR is the *Travelling Distance Rate*, ub_j and lb_j are variable bounds, and r_2, r_3 are uniform random numbers.

A.1.4 Adaptive Parameters

The wormhole existence probability (WEP) and TDR are adaptively updated to balance exploration and exploitation:

$$WEP = WEP_{\min} + l \cdot \frac{WEP_{\max} - WEP_{\min}}{L}, \quad TDR = 1 - \left(\frac{l}{L}\right)^{1/P}, \tag{A.4}$$

where l is the current iteration, L is the maximum number of iterations, and P controls exploitation precision.

A.1.5 Stopping Criterion and Complexity

The optimization proceeds iteratively until a predefined stopping criterion, such as the minimum error or maximum iterations, is reached. The computational complexity of MVO is dominated by the roulette-wheel selection and sorting of universes:

$$O(MVO) = O\left(L\left(n \log n + n \cdot d\right)\right), \tag{A.5}$$

where L is the number of iterations, n is the number of universes, and d is the number of decision variables.

A.2 Loss Function

The training of the proposed VOH-Net model relies on a composite loss function specifically designed to balance pixel-level accuracy, structural coherence, and phase smoothness in the reconstructed outputs. The total loss combines three complementary components: the Mean Squared Error (MSE) loss, a Gradient Regularization term, and a Variance of Error loss. Together, these terms ensure that the model minimizes both global and local discrepancies between predicted and ground-truth phase maps.

The first component, the Mean Squared Error (MSE), quantifies the pixel-wise difference between the reconstructed phase map and its corresponding ground truth:

$$L_{\text{mse}} = \frac{1}{N} \sum_{i,j} \left(y_{\text{pred},i,j} - y_{\text{true},i,j}\right)^2, \tag{A.6}$$

where N denotes the total number of pixels, y_{pred} represents the network prediction, and y_{true} corresponds to the reference phase. This term encourages the model to produce phase values that closely approximate the ground truth at each pixel location.

To further enhance structural consistency, a Gradient Regularization Loss is introduced. This term penalizes large discrepancies between the spatial gradients of the predicted and true phase maps, promoting smooth transitions while preserving essential edge structures:

$$L_{\text{grad}} = \frac{1}{N} \sum_{i,j} \left(|\nabla_x y_{\text{pred},i,j} - \nabla_x y_{\text{true},i,j}| + |\nabla_y y_{\text{pred},i,j} - \nabla_y y_{\text{true},i,j}|\right). \tag{A.7}$$

Finally, to maintain statistical stability in the prediction error distribution, a Variance of Error Loss is employed. This term ensures that the network not only minimizes the average error but also controls its spread across the image:

$$L_{\text{var}} = \frac{1}{N} \sum_{i,j} \left(E_{i,j} - \bar{E}\right)^2, \tag{A.8}$$

where $E = y_{\text{pred}} - y_{\text{true}}$ and $\bar{E}$ represents the mean of E over all pixels. By penalizing deviations from the mean error, this term enforces consistency in prediction accuracy across spatial regions.

The overall training objective integrates these three components into a single weighted function:

$$\text{Loss} = L_{\text{mse}} + \lambda \cdot L_{\text{grad}} + L_{\text{var}}, \tag{A.9}$$

where the hyperparameter $\lambda = 0.1$ controls the influence of the gradient regularization term. This value was determined empirically through a grid search over $\lambda \in \{0.01, 0.05, 0.1, 0.2\}$, with $\lambda = 0.1$ providing the most balanced trade-off between preserving smooth phase continuity and maintaining high pixel-wise reconstruction accuracy. Higher values of λ tended to oversmooth the phase surface, whereas smaller values resulted in residual discontinuities.

Table A.1 presents a comparison between the original and modified loss formulations, highlighting their respective components and contributions to overall model performance.

Table A.1: Comparison between original and modified loss functions.

Aspect	**Original Loss Function**	**Modified Loss Function**
Gradient Regularization Loss	Yes	Yes
Variance of Error Loss	Yes	Yes
Mean Squared Error	No	Yes
Final Objective	Smoothness + Error Consistency	Smoothness + Error Consistency + Pixel-wise Accuracy

The modified formulation explicitly introduces the Mean Squared Error term, which enhances pixel-level precision without compromising the smoothness and consistency promoted by the original loss components. This combination ensures that VOH-Net reconstructs globally consistent phase surfaces while preserving fine structural details required for accurate interferometric analysis.

Appendix B

Algorithms

B.1 Opimized Phase Unwrapping Algorithm

Phase unwrapping is a critical step in InSAR interferometry, where the accuracy of unwrapped phases directly impacts subsequent applications such as deformation mapping and topographic analysis.

Table B.1: Optimization-Guided Phase Unwrapping Algorithm Steps Using MVO

Step	Description
1	**Interferogram Generation:** Input interferogram $I(x,y) = A(x,y) \cdot e^{j\phi(x,y)}$, then separate amplitude $A(x,y)$ and wrapped phase $\phi(x,y)$.
2	**Mask Creation:** Generate binary mask $M(x,y)$ by thresholding amplitude: $M(x,y) = 1$ if $A(x,y) \geq \tau \cdot \max(A)$, otherwise 0. Typically, $\tau = 0.3$.
3	**Phase Quality Map:** Compute PDV-based quality map $Q(x,y) = C(\lvert\partial\phi/\partial x\rvert^H + \lvert\partial\phi/\partial y\rvert^B) + D\nabla^2\phi + G\sigma^2_{\text{local}}(\phi)$ with parameters C, H, B, D, G.
4	**Seed Point Selection:** Choose starting point $(x_0, y_0) = \arg\max_{(x,y)\in M} A(x,y)$ for phase unwrapping.
5	**Guided Flood Fill Unwrapping:** Propagate unwrapped phase $\Phi(x', y') = \Phi(x,y) + \Delta\phi(x, y \to x', y')$, processing neighbors with valid mask and highest quality.
6	**Objective Function Evaluation:** Evaluate unwrapped phase quality using N_D (number of discontinuities) and L_D (length of discontinuities): $f(P_O) = \alpha N_D + \beta L_D$.
7	**Parameter Optimization:** Use Multi-Verse Optimizer (MVO) to find optimal parameter vector $P_O = [C, H, B, D, G]$ minimizing $f(P_O)$, then regenerate PDV map for robust unwrapping.

This work proposes a novel optimization-guided framework that improves the reliability of phase unwrapping in noisy and discontinuous interferograms. By integrating a tunable Phase Derivative Variance (PDV) map into a Guided Flood Fill (GFF) algorithm, and optimizing its parameters with a Multi-Verse Optimizer (MVO), the system ensures smoother and more accurate unwrapped phase results while minimizing discontinuities.

B.2 Voh-Net Algorithm

The proposed VOH-Net model is designed for interferometric phase reconstruction and follows a symmetric encoder–decoder architecture enhanced with an E-LSTM module. The encoder extracts multi-scale spatial features from the input wrapped phase map, which are then processed along horizontal, vertical, diagonal, and anti-diagonal directions by the E-LSTM to capture long-range spatial dependencies and resolve complex phase discontinuities. The decoder reconstructs the unwrapped phase map by progressively upsampling and refining features while incorporating contextual information from the encoder. The network is trained with a composite loss function that balances pixel-level accuracy, structural consistency, and phase smoothness, enabling robust performance under noise, aliasing, and decorrelation effects.

Table B.2: VOH-Net Algorithm Steps (Symbolic Form)

Step	**Description**
1	$\psi \in \mathbb{R}^{256\times256\times1}$: input wrapped phase map
2	Encoder: $P_k = \mathrm{AvgPool}(\mathrm{ReLU}(\mathrm{BN}(\mathrm{Conv2D}(P_{k-1}, W_k) + b_k)))$, $k = 1..4$
3	E-LSTM: $X_{\mathrm{dir}} = \mathrm{Reshape}_{\mathrm{dir}}(P_4)$; $H_{\mathrm{dir}} = \mathrm{E}-\mathrm{LSTM}(X_{\mathrm{dir}}, W_{\mathrm{lstm}}, b_{\mathrm{lstm}})$
4	Feature Concatenation: $H = \mathrm{Concat}(H_{\mathrm{hor}}, H_{\mathrm{ver}}, H_{\mathrm{diag}}, H_{\mathrm{anti-diag}})$
5	Decoder: $U_k = \mathrm{Conv2DTranspose}(H_{k-1}, W_k^{\mathrm{T}}) + b_k^{\mathrm{T}}$; $U_k' = \mathrm{Concat}(U_k, C_{9-k})$; $H_k = \mathrm{Conv2D}(U_k', W_k) + b_k$
6	Output: $\phi = \mathrm{Conv2D}(H_8, W_{\mathrm{out}}) + b_{\mathrm{out}}$
7	Loss: $\mathrm{Loss} = L_{\mathrm{mse}} + \lambda L_{\mathrm{grad}} + L_{\mathrm{var}}$, $\lambda = 0.1$

Appendix C

Scientific Production

C.1 Publications

1. **Saoussen Djeddi**, Tarek Bentahar, Saidi, Riad., & Yacine Belhocine. (2025). VOH-Net: Vision-Optimized Hybrid Network for Deep Learning-Based Phase Unwrapping. Advances in Space Research. 77(3), https://doi.org/10.1016/j.asr.-2025.11.077

2. **Saoussen Djeddi**, Tarek Bentahar, Saidi, Riad., & Yacine Belhocine. (2026). Optimization-Guided Quality Mapping for Improved InSAR Phase Unwrapping. Signal Processing: Image Communication, 117620. https://doi.org/10.1016/j.image.2026.117620

C.2 International Conferences

1. **Djeddi, S**., Bentahar, T., Bentahar, A., Saidi, R., & Djellab, H. (2024). A Comparative Analysis of Branch-Cut and Quality-Guided Algorithms For inSAR Interferogram. 2024 8th International Conference on Image and Signal Processing and Their Applications (ISPA), 1–8. https://doi.org/10.1109/ispa59904.2024.10536705

2. **Djeddi, S**., Bentahar, T., Bentahar, A., Saidi, R., & Djellab, H. (2024). Securing and Enhancing Remote Sensing Image Transmission: A Comprehensive Approach Utilizing Hamming and Reed-Solomon Codes. 2024 2nd International

Conference on Electrical Engineering and Automatic Control (ICEEAC), 1–6. https://doi.org/10.1109/iceeac61226.2024.10576209

3. **Djeddi, S**., Belhocine, Y., Mebarkia, M,. & Meraoumia, A. (2025). Biometric Evolution: Leveraging Semi-Supervised Learning for Secure Identification. 2025 7th International Conference on Pattern Analysis and Intelligent Systems (PAIS), 1–6. https://doi.org/10.1109/pais66004.2025.11126457

4. **Djeddi, S**., Belhocine, Y., Mebarkia, M,. Meraoumia, A., & Bendjenna, H. (2025). Enhanced finger-knuckle-print recognition using deep texture feature analysis. 2021 International Conference on Recent Advances in Mathematics and Informatics (ICRAMI), 1-6.

5. Benamara, K., Saidi, R., Bentahar, T., Djellab, H., Belhocine, Y., & **Djeddi, S**. (2025). Encryption of InSAR Interferograms Based on AES-256 with Integration of Logistic Chaos. Lecture Notes in Electrical Engineering, 333–348. https://doi.org/10.1007/978-981-95-1109-9_36

6. Bentahar, T., **Djeddi, S**., & Belhocine, Y. (2025, October). InSAR-Based Ground Deformation Monitoring: Uncertainty Analysis and Public Safety Applications. In 2025 International Conference on Metrology, Industrial Control and Innovation (ICMICI). 1-6, Setif, Algeria.

7. Belhocine, Y., Djeddi, S., Meraoumia, A., Bendjenna, H., & Chitroub, S. (2026, April). Toward Explainable Systems: Homomorphic Filtering and Fisher-Aware Dictionary Learning. 2026 1st International Conference on Data Analytics and Intelligent Systems (DAIS), 1–13. Springer.

C.3 National Conferences

1. **Djeddi, S**., Bentahar, T., Saidi, R., Benamara, K., Belhocine, Y., & Djellab, H. (2024). Implementation and analysis of AES-256 for secure interferometric synthetic aperture radar (InSAR) data protection. In The First National Conference on Advances in Telecommunications, Electronics and Computer Engineering (ATECE), 1-6, Khenchela, Algeria

2. **Djeddi, S**., Bentahar, T., Saidi, R., Djellab, H., Belhocine, Y., & Benamara, K. (2024). Enhancing phase derivative variance in quality guided phase unwrapping for SAR interferometry. In 1st National Conference on Artificial Intelligence and Information Technology (NCAIIT). Ghilizane, Algeria.

3. **Djeddi, S**., Bentahar, T., & Saidi, R. (2025, September). Analysis and Discussion on Phase Unwrap-ping Techniques for SAR Interferometry. In 2025 National Conference on Innovation in Electronics and Telecommunication Technologies (NCIETT), (1-6 pages). Tebessa, Algeria.

4. **Djeddi, S**., Bentahar, T., Saidi, R., Belhocine, Y,. & Bentahar, A. (2025, January). Mixed Noise Reduction in InSAR Interferograms Using Robust Trilateral Filtering. In 2025 National Conference on Electrical Engineering, Renewable Energy, and Artificial Intelligence (NCEERA), (1-6 pages). Barika, Algeria.

C.4 Workshops

1. **Djeddi, S**., Belhocine, Y., & Mahdjoub., FZ. (2026, April). AI-based security in telecommunication networks. In 2026 1st Research Day on Intelligent Telecom Networks Hackathon (ITNH). Tebessa, Algeria.

Bibliography

[1] Bamler, R., & Hartl, P. (1998). Synthetic aperture radar interferometry. Inverse Problems, 14(4), R1–R54. https://doi.org/10.1088/0266-5611/14/4/001

[2] Rosen, P. A., Hensley, S., Joughin, I. R., Li, F. K., Madsen, S. N., Rodriguez, E., & Goldstein, R. M. (2000). Synthetic aperture radar interferometry. Proceedings of the IEEE, 88(3), 333–382. https://doi.org/10.1109/5.838084

[3] Crosetto, M., Monserrat, O., Cuevas-González, M., Devanthéry, N., & Crippa, B. (2016). Persistent scatterer interferometry: A review. ISPRS Journal of Photogrammetry and Remote Sensing, 115, 78–89. https://doi.org/10.1016/j.isprsjprs.2015.10.011

[4] Ghiglia, D. C., & Pritt, M. D. (1998). Two-dimensional phase unwrapping: Theory, algorithms, and software. Wiley. ISBN 978-0471249351.

[5] Ferretti, A., Prati, C., & Rocca, F. (2001). Permanent scatterers in SAR interferometry. IEEE Transactions on Geoscience and Remote Sensing, 39(1), 8–20. https://doi.org/10.1109/36.898661

[6] Massonnet, D., Rossi, M., Carmona, C., Adragna, F., Peltzer, G., Feigl, K., & Rabaute, T. (1993). The displacement field of the Landers earthquake mapped by radar interferometry. Nature, 364, 138–142. https://doi.org/10.1038/364138a0

[7] Lu, Z., & Dzurisin, D. (2014). InSAR imaging of Aleutian volcanoes: Monitoring a volcanic arc from space. Springer.

[8] Wright, T. J., Parsons, B. E., & Lu, Z. (2004). Toward mapping surface deformation in three dimensions using InSAR. Geophysical Research Letters, 31(1), L01607. https://doi.org/10.1029/2003GL018827

[9] Pepe, A., & Calò, F. (2017). A review of interferometric synthetic aperture RADAR (InSAR) multi-track approaches for the retrieval of Earth's surface displacements. Applied Sciences, 7(12), Article 1264. https://doi.org/10.3390/app7121264

[10] Hooper, A. (2008). A multi-temporal InSAR method incorporating both persistent scatterer and small baseline approaches. Geophysical Research Letters, 35(16), L16302. https://doi.org/10.1029/2008GL034654

[11] Crosetto, M., Monserrat, O., Iglesias, R., & Crippa, B. (2010). Persistent scatterer interferometry: Potential, limits and initial C- and X-band comparison. Photogrammetric Engineering & Remote Sensing, 76(9), 1061–1069.

[12] Osmanoğlu, B., Sunar, F., Wdowinski, S., & Cabral-Cano, E. (2016). Time series analysis of InSAR data: Methods and trends. ISPRS Journal of Photogrammetry and Remote Sensing, 115, 90–102. https://doi.org/10.1016/j.isprsjprs.2015.10.003

[13] Herraez, M. A., Burton, D. R., Lalor, M. J., & Gdeisat, M. A. (2002). Fast two-dimensional phase-unwrapping algorithm based on sorting by reliability following a noncontinuous path. Applied Optics, 41(35), 7437–7444. https://doi.org/10.1364/AO.41.007437

[14] Goldstein, R. M., Zebker, H. A., & Werner, C. L. (1988). Satellite radar interferometry: Two-dimensional phase unwrapping. Radio Science, 23(4), 713–720. https://doi.org/10.1029/RS023i004p00713

[15] Tikhonov, A. N., & Arsenin, V. Y. (1977). Solutions of ill-posed problems. Winston.

[16] Tarantola, A. (2005). Inverse problem theory and methods for model parameter estimation. SIAM.

[17] Aster, R. C., Borchers, B., & Thurber, C. H. (2018). Parameter estimation and inverse problems (3rd ed.). Elsevier.

[18] Massonnet, D., & Feigl, K. L. (1998). Radar interferometry and its application to changes in the Earth's surface. Reviews of Geophysics, 36(4), 441–500. https://doi.org/10.1029/97RG03139

[19] Yu, H., Bamler, R., Lanari, R., & Liu, Y. (2019). Interferometric SAR phase unwrapping: A review of methods and applications. IEEE Geoscience and Remote Sensing Magazine, 7(3), 40–58.

[20] Valentino, G., Briffa, J., Farrugia, R. A., & Fejjari, A. (2023). Interferometric phase denoising and unwrapping: A literature review. Xjenza Online, 11(Special issue), 49–58.

[21] Mirjalili, S., Mirjalili, S. M., & Hatamlou, A. (2016). Multi-verse optimizer: A nature-inspired algorithm. Neural Computing and Applications, 27(2), 495–513. https://doi.org/10.1007/s00521-015-1870-7

[22] Perera, M. V., & De Silva, A. (2021). A joint convolutional and spatial quad-directional LSTM network for phase unwrapping. In ICASSP 2021 - 2021 IEEE International Conference on Acoustics, Speech and Signal Processing (ICASSP) (pp. 4055–4059). IEEE.

[23] Moreira, A., Prats-Iraola, P., Younis, M., Krieger, G., Hajnsek, I., & Papathanassiou, K. P. (2013). A tutorial on synthetic aperture radar. IEEE Geoscience and Remote Sensing Magazine, 1(1), 6–43.

[24] Cheney, M. (2001). A mathematical tutorial on synthetic aperture radar. SIAM Review, 43(2), 301–312.

[25] Hanssen, R. F. (2001). Radar interferometry: Data interpretation and error analysis. Kluwer Academic Publishers.

[26] Curlander, J. C., & McDonough, R. N. (2021). Synthetic aperture radar: Systems and signal processing (Revised ed.). Wiley.

[27] Cumming, I. G., & Wong, F. H. (2022). Digital processing of synthetic aperture radar data (2nd ed.). Artech House.

[28] Franceschetti, G., & Lanari, R. (2018). Synthetic aperture radar processing. CRC Press.

[29] Tomiyasu, K. (1978). Tutorial review of synthetic-aperture radar (SAR) with applications to imaging of the ocean surface. Proceedings of the IEEE, 66(5), 563–583.

[30] Fornaro, G., Pauciullo, A., & Reale, D. (2011). A null-space method for the phase unwrapping of multitemporal SAR interferometric stacks. IEEE Transactions on Geoscience and Remote Sensing, 49(6), 2323–2334

[31] Zebker, H. A., Rosen, P. A., & Hensley, S. (1997). Atmospheric effects in interferometric synthetic aperture radar surface deformation and topographic maps. Journal of Geophysical Research: Solid Earth, 102(B4), 7547–7563.

[32] Berardino, P., Fornaro, G., Lanari, R., & Sansosti, E. (2002). A new algorithm for surface deformation monitoring based on small baseline differential SAR interferograms. IEEE Transactions on Geoscience and Remote Sensing, 40(11), 2375–2383.

[33] Bürgmann, R., Rosen, P. A., & Fielding, E. J. (2000). Synthetic aperture radar interferometry to measure Earth's surface topography and its deformation. Annual Review of Earth and Planetary Sciences, 28, 169–209.

[34] Zebker, H. A., & Villasenor, J. (1992). Decorrelation in interferometric radar echoes. IEEE Transactions on Geoscience and Remote Sensing, 30(5), 950–959.

[35] Lee, J.-S., Papathanassiou, K. P., Ainsworth, T. L., Grunes, M. R., & Reigber, A. (2003). A new technique for noise filtering of SAR interferometric phase images. IEEE Transactions on Geoscience and Remote Sensing, 41(10), 2279–2285.

[36] Goldstein, R. M., & Werner, C. L. (1998). Radar interferogram filtering for geophysical applications. Geophysical Research Letters, 25(21), 4035–4038.

[37] Yu, H., Lan, Y., Yuan, Z., Xu, J., & Lee, H. (2019). Phase unwrapping in InSAR: A review. IEEE Geoscience and Remote Sensing Magazine, 7(1), 40–58.

[38] Itoh, K. (1982). Analysis of the phase unwrapping problem. Applied Optics, 21(14), 2470–2471.

[39] Liu, Y., Wu, H., Zhang, Y., Lu, Z., Kang, Y., & Wei, J. (2025). 3D automatic detection and correction for phase unwrapping errors in time series SAR interferometry. ISPRS Journal of Photogrammetry and Remote Sensing, 220, 232–245.

[40] Costantini, M. (1998). A novel phase unwrapping method based on network programming. IEEE Transactions on Geoscience and Remote Sensing, 36(3), 813–821.

[41] Jolivet, R., Grandin, R., Lasserre, C., Doin, M.-P., & Peltzer, G. (2011). Systematic InSAR tropospheric phase delay corrections from global meteorological reanalysis data. Geophysical Research Letters, 38(17), L17311.

[42] Gong, W., Li, Z., & Lin, H. (2021). Phase unwrapping techniques in SAR interferometry: Current status and future directions. Remote Sensing, 13(15), 2950. https://doi.org/10.3390/rs13152950

[43] Abdul-Rahman, H. S., Gdeisat, M. A., Burton, D. R., Lalor, M. J., Lilley, F., & Moore, C. J. (2007). Fast and robust three-dimensional best path phase unwrapping algorithm. Applied Optics, 46(26), 6623–6635. https://doi.org/10.1364/AO.46.006623

[44] Cusack, R., Huntley, J. M., & Goldrein, H. T. (1995). Improved noise-immune phase-unwrapping algorithm. Applied Optics, 34(5), 781–789.

[45] Flynn, T. J. (1997). Two-dimensional phase unwrapping with minimum weighted discontinuity. Journal of the Optical Society of America A, 14(10), 2692–2701.

[46] Holland, J. H. (1975). Adaptation in natural and artificial systems. University of Michigan Press.

[47] Qin, Y., Wan, S., Wan, Y., Weng, J., Liu, W., & Gong, Q. (2020). Direct and accurate phase unwrapping with deep neural network. Applied Optics, 59(24), 7258–7267. https://doi.org/10.1364/AO.399715

[48] Pritt, M. D. (1996). Phase unwrapping by means of multigrid techniques for interferometric SAR. IEEE Transactions on Geoscience and Remote Sensing, 34(3), 728–738.

[49] Costantini, M., Farina, A., Zirilli, F., & Barba, S. (1999). A wrap-reduction approach to SAR interferometry phase unwrapping. International Journal of Remote Sensing, 20(18), 3855–3875.

[50] Fornaro, G., Franceschetti, G., Lanari, R., Pascazio, V., & Schirinzi, G. (1996). Interferometric SAR phase unwrapping using Green's formulation. IEEE Transactions on Geoscience and Remote Sensing, 34(3), 720–727.

[51] Chen, C. W., & Zebker, H. A. (2001). Network approaches to two-dimensional phase unwrapping: InSAR applications. IEEE Transactions on Geoscience and Remote Sensing, 39(1), 12–21. https://doi.org/10.1109/36.898661

[52] Chen, C. W., & Zebker, H. A. (2002). Phase unwrapping for large SAR interferograms: Statistical segmentation and generalized network models. IEEE Transactions on Geoscience and Remote Sensing, 40(8), 1709–1719.

[53] Pepe, A., & Lanari, R. (2006). On the extension of the minimum cost flow algorithm for phase unwrapping of multitemporal differential SAR interferograms. IEEE Transactions on Geoscience and Remote Sensing, 44(9), 2374–2383.

[54] Yu, H., & Lan, Y. (2016). Robust two-dimensional phase unwrapping for multibaseline SAR interferograms: A two-stage programming approach. IEEE Transactions on Geoscience and Remote Sensing, 54(2), 1050–1063. https://doi.org/10.1109/TGRS.2015.2477871

[55] Yu, H., Li, Z., & Bao, Z. (2011). A cluster-analysis-based efficient multibaseline phase-unwrapping algorithm. IEEE Transactions on Geoscience and Remote Sensing, 49(1), 478–487. https://doi.org/10.1109/TGRS.2010.2055631

[56] Pascazio, V., & Schirinzi, G. (2000). Multifrequency InSAR height reconstruction through maximum likelihood estimation of local planes parameters. IEEE Transactions on Image Processing, 11(12), 1478–1489. https://doi.org/10.1109/83.887498

[57] Fornaro, G., Pauciullo, A., & Sansosti, E. (2005). Phase difference-based multichannel phase unwrapping. IEEE Transactions on Image Processing, 14(7), 960–972. https://doi.org/10.1109/TIP.2005.847340

[58] Fornaro, G., Monti Guarnieri, A., Pauciullo, A., & De Zan, F. (2006). Maximum likelihood multi-baseline SAR interferometry. IEE Proceedings - Radar, Sonar and Navigation, 153(3), 279–288. https://doi.org/10.1049/ip-rsn:20050018

[59] Jiang, Z., Wang, J., Song, Q., & Zhou, Z. (2017). A refined cluster-analysis-based multibaseline phase-unwrapping algorithm. IEEE Geoscience and Remote Sensing Letters, 14(9), 1565–1569. https://doi.org/10.1109/LGRS.2017.2723178

[60] Yuan, Z., Wang, Z., Yu, H., Xing, X., Zhou, L., Chen, L., & Xu, J. (2025). A WaveCluster-Based Robust and Fast Multibaseline InSAR Phase Unwrapping Algorithm. IEEE Transactions on Geoscience and Remote Sensing, 63, 5223417. https://doi.org/10.1109/TGRS.2025.3630866

[61] Molan, Y. E., & Lohman, R. B. (2023). A pattern-based strategy for InSAR phase unwrapping. Journal of Geophysical Research: Solid Earth, 128, e2022JB025761. https://doi.org/10.1029/2022JB025761

[62] Goldberg, D. E. (1989). Genetic algorithms in search, optimization, and machine learning. Addison-Wesley.

[63] Eberhart, R. C., & Shi, Y. (2001). Particle swarm optimization: Developments, applications and resources. In Proceedings of the 2001 Congress on Evolutionary Computation (pp. 81–86). IEEE.

[64] Mirjalili, S., Mirjalili, S. M., & Lewis, A. (2014). Grey wolf optimizer. Advances in Engineering Software, 69, 46–61. https://doi.org/10.1016/j.advengsoft.2013.12.007

[65] Mirjalili, S., Lewis, A., & Sayed, S. A. M. (2014). Grey wolf optimizer. Advances in Engineering Software, 69, 46–61.

[66] Kumar, S. V., Sun, X., Wang, Z., Goldsbury, R., & Cheng, I. (2023). A U-Net approach for InSAR phase unwrapping and denoising. Remote Sensing, 15(21), 5081. https://doi.org/10.3390/rs15215081

[67] Yang, W., He, Y., Zhu, Q., Zhang, L., & Jin, L. (2024). Unwrap-Net: A deep neural network-based InSAR phase unwrapping method assisted by airborne LiDAR data. ISPRS Journal of Photogrammetry and Remote Sensing, 218, 510–529.

[68] Liu, B., Wu, L., Song, X., Hao, H., Zou, L., & Lu, Y. (2023). PUnet: A robust framework for phase unwrapping in interferometric SAR. Frontiers in Environmental Science, 11, 1138399. https://doi.org/10.3389/fenvs.2023.1138399

[69] Zhou, L., & Yu, H. (2024). InSAR-DLPU: A benchmark dataset for deep learning-based synthetic aperture radar interferometry phase unwrapping [Software and Data Sets]. IEEE Geoscience and Remote Sensing Magazine, 12, 118–124. https://doi.org/10.1109/MGRS.2024.3359691

[70] Spoorthi, G. E., Gorthi, S. S., & Gorthi, R. K. S. S. (2020). PhaseNet 2.0: Phase unwrapping of noisy data based on deep learning approach. IEEE Transactions on Image Processing, 29, 4862–4872. https://doi.org/10.1109/TIP.2020.2977213

[71] Feng, X., Wei, L., Ren, X., Zhao, C., Ao, M., Wang, Y., Luo, J., & Bignami, C. (2026). Phase gradient rate constrained minimum cost flow: A robust unwrapping method for landslides with large deformation gradients. ISPRS Journal of Photogrammetry and Remote Sensing, 232, 1–16. https://doi.org/10.1016/j.isprsjprs.2025.12.017

[72] Pu, L., Zhang, X., Zhou, Z., Li, L., Zhou, L., Shi, J., & Wei, S. (2021). A robust InSAR phase unwrapping method via phase gradient estimation network. Remote Sensing, 13(22), 4564. https://doi.org/10.3390/rs13224564

[73] Yang, W., He, Y., Zhu, Q., Zhang, L., & Jin, L. (2024). Unwrap-Net: A deep neural network-based InSAR phase unwrapping method assisted by airborne LiDAR data. ISPRS Journal of Photogrammetry and Remote Sensing, 218, 510–529. https://doi.org/10.1016/j.isprsjprs.2024.11.009

[74] Ronneberger, O., Fischer, P., & Brox, T. (2015). U-Net: Convolutional networks for biomedical image segmentation. In Medical Image Computing and Computer-Assisted Intervention (pp. 234–241). Springer.

[75] Hochreiter, S., & Schmidhuber, J. (1997). Long short-term memory. Neural Computation, 9(8), 1735–1780.

[76] He, K., Zhang, X., Ren, S., & Sun, J. (2016). Deep residual learning for image recognition. In Proceedings of the IEEE Conference on Computer Vision and Pattern Recognition (pp. 770–778).

[77] Saoussen Djeddi, Tarek Bentahar, Saidi, R., & Yacine Belhocine. (2025). VOH-Net: Vision-Optimized Hybrid Network for Deep Learning-Based Phase Unwrapping. Advances in Space Research. https://doi.org/10.1016/j.asr.2025.11.077

[78] Xu, W., Cumming, I. G., & Bamler, R. (1996). A region-growing algorithm for InSAR phase unwrapping. IEEE Transactions on Geoscience and Remote Sensing, 34(2), 471–476.

[79] Chen, Y., Liu, Y., Zhang, L., & Li, W. (2023). A hybrid optimization framework for robust phase unwrapping in low-coherence regions. IEEE Transactions on Geoscience and Remote Sensing, 61, 1–13. https://doi.org/10.1109/TGRS.2023.3267401

[80] Wang, H., & Wang, C. (2022). Graph-based optimization for reliable phase unwrapping in complex terrain. Remote Sensing, 14(4), 849. https://doi.org/10.3390/rs14040849

[81] Zhang, Z., & Jiang, W. (2021). Phase unwrapping using a primal-dual network optimization model with total variation constraints. ISPRS Journal of Photogrammetry and Remote Sensing, 179, 109–121. https://doi.org/10.1016/j.isprsjprs.2021.07.013

[82] Cho, K., van Merriënboer, B., Gulcehre, C., Bahdanau, D., Bougares, F., Schwenk, H., & Bengio, Y. (2014). Learning phrase representations using RNN encoder-decoder for statistical machine translation. In Proceedings of EMNLP (pp. 1724–1734).

[83] LeCun, Y., Bengio, Y., & Hinton, G. (2015). Deep learning. Nature, 521, 436–444. https://doi.org/10.1038/nature14539

[84] Goodfellow, I., Bengio, Y., & Courville, A. (2016). Deep learning. MIT Press. http://www.deeplearningbook.org

[85] Kingma, D. P., & Ba, J. (2015). Adam: A method for stochastic optimization. In International Conference on Learning Representations.

[86] Raissi, M., Perdikaris, P., & Karniadakis, G. E. (2019). Physics-informed neural networks: A deep learning framework for solving forward and inverse problems involving nonlinear partial differential equations. Journal of Computational Physics, 378, 686–707.

[87] Kendall, A., & Gal, Y. (2017). What uncertainties do we need in Bayesian deep learning for computer vision In Advances in Neural Information Processing Systems (pp. 5574–5584).

[88] Vaswani, A., Shazeer, N., Parmar, N., Uszkoreit, J., Jones, L., Gomez, A. N., Kaiser, Ł., & Polosukhin, I. (2017). Attention is all you need. In Advances in Neural Information Processing Systems (pp. 5998–6008).

[89] Dosovitskiy, A., Beyer, L., Kolesnikov, A., Weissenborn, D., Zhai, X., Unterthiner, T., Dehghani, M., Minderer, M., Heigold, G., Gelly, S., Uszkoreit, J., & Houlsby, N. (2021). An image is worth 16x16 words: Transformers for image recognition at scale. In International Conference on Learning Representations.

[90] Zhao, X., Ma, J., Wang, L., Zhang, Z., Ding, Y., & Xiao, X. (2025). A review of hyperspectral image classification based on graph neural networks. Artificial Intelligence Review, 58, 172. https://doi.org/10.1007/s10462-025-11169-y

[91] Raspini, F., Caleca, F., Del Soldato, M., Festa, D., Confuorto, P., & Bianchini, S. (2022). Review of satellite radar interferometry for subsidence analysis. Earth-Science Reviews, 235, 104239. https://doi.org/10.1016/j.earscirev.2022.104239

[92] Ferretti, A., Monti-Guarnieri, A., Prati, C., Rocca, F., & Massonnet, D. (2007). InSAR Principles: Guidelines for SAR Interferometry Processing and Interpretation (ESA TM-19). ESA Publications.

[93] Hooper, A., Bekaert, D., Spaans, K., & Arıkan, M. (2012). Recent advances in SAR interferometry time series analysis for measuring crustal deformation. Tectonophysics, 514–517, 1–13.

[94] Zebker, H. A., & Goldstein, R. M. (1986). Topographic mapping from interferometric SAR. Journal of Geophysical Research, 91(B5), 4993–4999.

[95] Xu, W., Chang, E., Kwoh, L., Lim, H., & Cheng, W. (1994). Phase-unwrapping of SAR interferogram with multi-frequency or multibaseline. In Proceedings of the IEEE International Geoscience and Remote Sensing Symposium (pp. 730–732). Pasadena, CA.

[96] Yu, H., Xing, M., & Bao, Z. (2013). A fast phase unwrapping method for large-scale interferograms. IEEE Transactions on Geoscience and Remote Sensing, 51(10), 5154–5165.

[97] Zhang, K., Ge, L., Hu, Z., Ng, A., Li, X., & Rizos, C. (2011). Phase unwrapping for very large interferometric data sets. IEEE Transactions on Geoscience and Remote Sensing, 49(10), 4048–4061.

[98] Chen, C., & Zebker, H. A. (2000). Network approaches to two-dimensional phase unwrapping. JOSA A, 17(3), 401–414.

[99] Kennedy, J., & Eberhart, R. (1995). Particle swarm optimization. In Proceedings of the IEEE International Conference on Neural Networks (pp. 1942–1948).

[100] Yuan, Z., Deng, Y., Li, F., Wang, R., Liu, G., & Han, X. (2013). Multichannel InSAR DEM reconstruction through improved closed-form robust Chinese remainder theorem. IEEE Geoscience and Remote Sensing Letters, 10(6), 1314–1318.

[101] Ghiglia, D. C., & Wahl, D. E. (1994). Interferometric synthetic aperture radar terrain elevation mapping from multiple observations. In Proceedings of the IEEE Digital Signal Processing Workshop (pp. 33–36). Albuquerque, NM.

[102] Lombardo, P., & Lombardini, F. (1997). Multi-baseline SAR interferometry for terrain slope adaptivity. In Proceedings of the National Radar Conference (pp. 196–201).

[103] Fornaro, G., Pauciullo, A., & Sansosti, E. (2002). Bayesian approach to phase-difference-based phase unwrapping. In Proceedings of the IEEE 36th Asilomar Conference on Signals, Systems and Computers (pp. 1397–1401). Napoli, Italy.

[104] Poggi, G., Ragozini, A. P. R., & Servadei, D. (2000). A Bayesian approach for SAR interferometric phase restoration. In Proceedings of the IEEE International Geoscience and Remote Sensing Symposium (pp. 3202–3205).

[105] Liu, H., Xing, M., & Bao, Z. (2015). A cluster-analysis-based noise-robust phase-unwrapping algorithm for multibaseline interferograms. IEEE Transactions on Geoscience and Remote Sensing, 53(1), 494–504.

[106] Yu, H., Lee, H., Yuan, T., & Cao, N. (2018). A novel method for deformation estimation based on multi-baseline InSAR phase unwrapping. IEEE Transactions on Geoscience and Remote Sensing, 56(9), 5231–5243.

[107] Wang, K., Li, Y., Qian, K., Di, J., & Zhao, J. (2019). One-step robust deep learning phase unwrapping. Optics Express, 27(10), 15100–15115.

[108] Kampes, B. M. (2006). Radar interferometry: Persistent scatterer technique. Springer.

[109] Peltzer, G., Rosen, P., Rogez, F., & Hudnut, K. (1998). Poro-elastic rebound along the Landers 1992 earthquake surface rupture. Journal of Geophysical Research: Solid Earth, 103(B12), 30131–30145.

[110] Joughin, I., Kwok, R., & Fahnestock, M. (1998). Interferometric estimation of three-dimensional ice-flow using ascending and descending passes. IEEE Transactions on Geoscience and Remote Sensing, 36(1), 25–37.

[111] Biggs, J., Wright, T., Lu, Z., & Parsons, B. (2007). Multi-interferogram method for measuring interseismic deformation: Denali fault, Alaska. Geophysical Journal International, 170(3), 1165–1179.

[112] Simons, M., Fialko, Y., & Rivera, L. (2002). Coseismic deformation from satellite radar interferometry: Model and examples. Geophysical Journal International, 151(3), 725–740.

[113] Massonnet, D., Feigl, K. L., Rossi, M., & Adragna, F. (1994). Radar interferometric mapping of deformation in the year after the Landers earthquake. Nature, 369, 227–230.

[114] Ketelaar, G. (2009). Satellite radar interferometry: Subsidence monitoring techniques. Springer.

[115] Gens, R., & van Genderen, J. L. (1996). SAR interferometry—issues, techniques, applications. International Journal of Remote Sensing, 17(10), 1803–1835.

[116] Li, Z., Fielding, E. J., & Cross, P. (2009). Integration of InSAR time-series analysis and water-vapour correction for mapping post-seismic motion after the 2003 Bam earthquake. Quarterly Journal of Engineering Geology and Hydrogeology, 42(1), 61–70.

[117] Bekaert, D. P. S., Hooper, A., & Wright, T. J. (2015). A spatially variable power law tropospheric correction technique for InSAR data. Journal of Geophysical Research: Solid Earth, 120(2), 1345–1356.

[118] Li, X., & Xu, Q. (2015). Ionospheric effects on L-band SAR interferometry and mitigation strategies. Remote Sensing of Environment, 170, 1–13.

[119] Small, D. (2011). Flattening gamma: Radiometric terrain correction for SAR imagery. IEEE Transactions on Geoscience and Remote Sensing, 49(8), 3081–3093.

[120] Lee, J.-S. (1981). Refined filtering of image noise using local statistics. Computer Graphics and Image Processing, 15(4), 380–389.

[121] Lopes, A., Nezry, E., Touzi, R., & Laur, H. (1993). Structure detection and statistical adaptive speckle filtering in SAR images. International Journal of Remote Sensing, 14(9), 1735–1758.

[122] Touzi, R., Lopes, A., Bruniquel, J., & Vachon, P. W. (1999). Coherence estimation for SAR imagery. IEEE Transactions on Geoscience and Remote Sensing, 37(1), 135–149.

[123] Lee, J.-S., Hoppel, K. W., Mango, S. A., & Miller, A. R. (1994). Intensity and phase statistics of multilook polarimetric and interferometric SAR imagery. IEEE Transactions on Geoscience and Remote Sensing, 32(5), 1017–1028.

[124] Bone, D. J. (2001). Fourier fringe analysis: The two-dimensional phase unwrapping problem. Applied Optics, 40(16), 2680–2686.

[125] Bioucas-Dias, J. M., & Valadão, G. (2007). Phase unwrapping via graph cuts. IEEE Transactions on Image Processing, 16(3), 698–709.

[126] Bioucas-Dias, J. M., & Valadão, G. (2008). Multichannel phase unwrapping with graph cuts. IEEE Transactions on Image Processing, 17(6), 923–935.

[127] Jenkinson, M. (2003). Fast, automated, N-dimensional phase-unwrapping algorithm. Magnetic Resonance in Medicine, 49(1), 193–197.

[128] Spagnolini, U. (1995). 2-D phase unwrapping and instantaneous frequency estimation. IEEE Transactions on Geoscience and Remote Sensing, 33(3), 579–589.

[129] Djeddi, S., Bentahar, T., Saidi, R., & Belhocine, Y. (2026). Optimization-guided quality mapping for improved InSAR phase unwrapping. Signal Processing: Image Communication, 148, 117620. https://doi.org/10.1016/j.image.2026.117620

[130] Ghiglia, D. C., Romero, L. A., & Pritt, M. D. (1993). Linear and nonlinear methods for two-dimensional phase unwrapping. Applied Optics, 32(5), 805–814.

[131] Martins, J. M. B., Bioucas-Dias, J. M., & Leitão, J. M. N. (2008). A new SAR interferometric phase unwrapping algorithm based on the shortest path tree. IEEE Transactions on Geoscience and Remote Sensing, 46(10), 3205–3215.

[132] Yu, H., Lan, Y., & Yuan, Z. (2012). Quality-guided phase unwrapping for large interferograms using block processing. IEEE Geoscience and Remote Sensing Letters, 9(5), 857–861.

[133] Liang, C., Fielding, E. J., Huang, M.-H., & Bürgmann, R. (2019). Coseismic fault-slip models inferred from geodetic data and implications for InSAR phase unwrapping in large deformation areas. Geophysical Journal International, 217(2), 1123–1139.

[134] Gao, Y., Zhang, S., Li, T., Chen, Q., Zhang, X., & Li, S. (2019). Refined two-stage programming approach of phase unwrapping for multi-baseline SAR interferograms using the unscented Kalman filter. Remote Sensing, 11(2), 199.

[135] Zhou, L., Lan, Y., Xia, Y., & Gong, S. (2020). Extended phase unwrapping max-flow/min-cut algorithm for multibaseline SAR interferograms using a two-stage programming approach. Sensors, 20(2), 375.

[136] Gao, Y., Tang, X., Li, T., Chen, Q., Zhang, X., Li, S., & Lu, J. (2020). Bayesian filtering multi-baseline phase unwrapping method based on a two-stage programming approach. Applied Sciences, 10(9), 3139.

[137] Ferraiuolo, G., Pascazio, V., & Schirinzi, G. (2004). Maximum a posteriori estimation of height profiles in InSAR imaging. IEEE Geoscience and Remote Sensing Letters, 1(2), 66–70.

[138] Ferraioli, G., Shabou, A., Tupin, F., & Pascazio, V. (2009). Multichannel phase unwrapping with graph cuts. IEEE Geoscience and Remote Sensing Letters, 6(3), 562–566.

[139] Lan, Y., Yu, H., & Xing, M. (2019). Refined two-stage programming-based multi-baseline phase unwrapping approach using local plane model. Remote Sensing, 11(5), 491.

[140] Lin, Z., Duan, Y., Deng, Y., Tian, W., & Zhao, Z. (2022). An improved multi-baseline phase unwrapping method for GB-InSAR. Remote Sensing, 14(11), 2543.

[141] Liu, H., Yue, J., Liu, W., Huang, Q., Li, G., & Liu, M. (2023). Multi-baseline phase unwrapping with robust branch and bound pure integer programming algorithm. Optics and Lasers in Engineering, 161, 107352.

[142] Wang, Z., Li, X., Xing, C., Wang, Z., Liu, P., & Li, Z. (2026). An improved closed-form multi-baseline phase unwrapping algorithm. Remote Sensing, 18(2), 214.

[143] Wu, Y., Zhang, H., Wang, J., Wang, R., Zhao, F., Wu, Z., & Cai, Y. (2022). Stereo-radargrammetry assisted InSAR phase unwrapping method for DEM generation. IEEE Transactions on Geoscience and Remote Sensing, 60, 5233718.

[144] Dardikman-Yoffe, G., Roitshtain, D., & Mirsky, S. (2020). PhUn-Net: Neural network for phase unwrapping. Biomedical Optics Express, 11(3), 1107–1117.

[145] Zhang, L., Huang, G., Li, Y., Yang, S., Lu, L., & Huo, W. (2023). A robust InSAR phase unwrapping method via improving the pix2pix network. Remote Sensing, 15(19), 4885.

[146] Mu, J., Wang, Y., Zhan, S., Yao, G., Liu, K., Zhu, Y., & Wang, L. (2024). A coherence-guided InSAR phase unwrapping method with cycle-consistent adversarial networks. IEEE Journal of Selected Topics in Applied Earth Observations and Remote Sensing, 17, 2690–2704.

[147] Boubacar-Sani, I., Jiang, X., Toure, S., Kpalma, K., Diop, O., & Maiga, A.-S. (2025). Spatio-temporal refinement for InSAR phase unwrapping using untrained neural networks. In 2025 33rd European Signal Processing Conference (EUSIPCO) (pp. 1777–1781). IEEE.

[148] Zhang, L., Zhang, L., & Du, B. (2016). Deep learning for remote sensing data: A technical tutorial on the state of the art. IEEE Geoscience and Remote Sensing Magazine, 4(2), 22–40.

[149] Zhu, X. X., Tuia, D., Mou, L., Xia, G.-S., Zhang, L., Xu, F., & Fraundorfer, F. (2017). Deep learning in remote sensing: A comprehensive review and list of resources. IEEE Geoscience and Remote Sensing Magazine, 5(4), 8–36.

[150] Ma, L., Liu, Y., Zhang, X., Ye, Y., Yin, G., & Johnson, B. A. (2019). Deep learning in remote sensing applications: A meta-analysis and review. ISPRS Journal of Photogrammetry and Remote Sensing, 152, 166–177.

[151] Ball, J. E., Anderson, D. T., & Chan, C. S. (2017). Comprehensive survey of deep learning in remote sensing: Theories, tools, and challenges for the community. Journal of Applied Remote Sensing, 11(4), 042609.

[152] Bishop, C. M. (2006). Pattern recognition and machine learning. Springer.

[153] Devlin, J., Chang, M.-W., Lee, K., & Toutanova, K. (2019). BERT: Pre-training of deep bidirectional transformers for language understanding. In Proceedings of the 2019 Conference of the North American Chapter of the Association for Computational Linguistics: Human Language Technologies (Vol. 1, pp. 4171–4186).

[154] Ghamisi, P., Plaza, J., Chen, Y., Li, J., & Plaza, A. J. (2017). Advanced spectral classifiers for hyperspectral images: A review. IEEE Geoscience and Remote Sensing Magazine, 5(1), 8–32.

[155] Reichstein, M., Camps-Valls, G., Stevens, B., Jung, M., Denzler, J., Carvalhais, N., & Prabhat. (2019). Deep learning and process understanding for data-driven Earth system science. Nature, 566, 195–204.

[156] Mou, L., Ghamisi, P., & Zhu, X. X. (2017). Deep recurrent neural networks for hyperspectral image classification. IEEE Transactions on Geoscience and Remote Sensing, 55(7), 3639–3655.

[157] Yang, X.-S. (2010). Nature-inspired metaheuristic algorithms (2nd ed.). Luniver Press.

[158] Dorigo, M., Maniezzo, V., & Colorni, A. (1996). Ant system: Optimization by a colony of cooperating agents. IEEE Transactions on Systems, Man, and Cybernetics, Part B: Cybernetics, 26(1), 29–41.

[159] Yang, X.-S., & Deb, S. (2009). Cuckoo search via Lévy flights. In 2009 World Congress on Nature & Biologically Inspired Computing (NaBIC) (pp. 210–214). IEEE.

[160] Talbi, E.-G. (2009). Metaheuristics: From design to implementation. Wiley.

[161] Wolpert, D. H., & Macready, W. G. (1997). No free lunch theorems for optimization. IEEE Transactions on Evolutionary Computation, 1(1), 67–82.

[162] Karaboga, D. (2005). An idea based on honey bee swarm for numerical optimization (Technical Report TR06). Erciyes University.

[163] Kennedy, J. (2011). Particle swarm optimization. In C. Sammut & G. I. Webb (Eds.), Encyclopedia of machine learning (pp. 760–766). Springer.

[164] Candès, E. J., Wakin, M. B., & Boyd, S. P. (2008). Enhancing sparsity by reweighted ℓ_1 minimization. Journal of Fourier Analysis and Applications, 14(5–6), 877–905.

[165] Kaipio, J. P., & Somersalo, E. (2005). Statistical and computational inverse problems. Springer.

[166] Zhang, K., Ge, L., Hu, Z., Ng, A., Li, X., & Rizos, C. (2011). Phase unwrapping for very large interferometric data sets. *IEEE Transactions on Geoscience and Remote Sensing*, 49(10), 4048–4061. https://doi.org/10.1109/TGRS.2011.2149640

[167] Pascazio, V., & Schirinzi, G. (2000). Multifrequency InSAR height reconstruction through maximum likelihood estimation of local planes parameters. *IEEE Transactions on Image Processing*, 11(12), 1478–1489. https://doi.org/10.1109/83.887498

[168] Fornaro, G., Monti Guarnieri, A., Pauciullo, A., & De-Zan, F. (2006). Maximum likelihood multi-baseline SAR interferometry. *IEE Proceedings - Radar, Sonar and Navigation*, 153(3), 279–288. https://doi.org/10.1049/ip-rsn:20050018

[169] Fornaro, G., Pauciullo, A., & Sansosti, E. (2005). Phase difference-based multichannel phase unwrapping. *IEEE Transactions on Image Processing*, 14(7), 960–972. https://doi.org/10.1109/TIP.2005.847340

[170] Fornaro, G., Pauciullo, A., & Sansosti, E. (2002). Bayesian approach to phase-difference-based phase unwrapping. In *Proceedings of the IEEE 36th Asilomar Conference on Signals, Systems and Computers* (pp. 1397–1401). Napoli, Italy.

[171] Perera, M. V., & Silva, A. D. (2021). A Joint Convolutional and Spatial Quad-Directional LSTM Network for Phase Unwrapping. In *ICASSP 2022 - 2022 IEEE International Conference on Acoustics, Speech and Signal Processing (ICASSP)* (pp. 4055–4059). https://doi.org/10.1109/icassp39728.2021.9414748

[172] Sica, F., Calvanese, F., Scarpa, G., & Rizzoli, P. (2020). A CNN-Based Coherence-Driven Approach for InSAR Phase Unwrapping. *IEEE Geoscience and Remote Sensing Letters*, 19, 1–5. https://doi.org/10.1109/lgrs.2020.3029565

[173] Morishita, Y. (2022). Effective unwrapping of complicated phases by exploiting multiple interferograms: a case study of the 2016 Kumamoto earthquake. *Earth Planets and Space*, 74(1). https://doi.org/10.1186/s40623-022-01595-5

[174] Cumming, I. G., & Wong, F. H. (2005). *Digital processing of synthetic aperture radar data*. Artech House, 1(3), 108–110.

[175] Thiel, C. (1997). *SAR Interferometry Applied to the Study of Land Subsidence in the Region of Mexico City*. Ph.D. Dissertation, University of Stuttgart.

[176] Mirjalili, S., Mirjalili, S. M., & Hatamlou, A. (2015). Multi-Verse Optimizer: a nature-inspired algorithm for global optimization. *Neural Computing and Applications*, in press. http://dx.doi.org/10.1007/s00521-015-1870-7